DEPARTAMENTO DE ASTROFÍSICA

Universidad de La Laguna

Shedding Light on Globular Cluster Formation: Age and Chemical Composition in the Multiple Stellar Population Scenario

Memoria que presenta
D. Matteo Simioni
para optar al grado de
Doctor por la Universidad de La Laguna.

INSTITUTO Đ ASTROFISICA Đ CANARIAS
junio de 2019

Examination date: July 2019
Thesis supervisors: Prof. Antonio Aparicio Juan (ULL, IAC); Prof. Giampaolo Piotto (UniPD, INAF-OAPD); Dr. Luigi Bedin (INAF-OAPD)

Abstract

In the past decades, major observational breakthroughs have revealed that Globular Clusters (GC) in the Milky Way host distinct stellar populations. Classically representing the best examples in nature of Simple Stellar Populations, these new findings have put GCs in the limelight. In particular, unveiling the origin of the so-called Multiple Stellar Population (MP) phenomenon, is nowadays an active field of investigation in Astrophysics.

GCs, in fact, play a key role in the study of the onset of the star formation in the Universe and the early evolution of stellar systems being fundamental to trace ages and chemical composition in the galaxies they belong to. This is especially true for the Milky Way: Galactic GCs are the oldest objects for which accurate and precise absolute ages can be determined; also, detailed chemical composition allows to infer the properties of the environment at the formation epoch.

Large observational programmes are being carried on with the aim to better characterize the MP phenomenon and to provide constraints for theoretical models. In this context, the present investigation made use of the data collected within the Hubble Space Telescope UV Legacy Survey of Galactic Globular Clusters. This exquisite data-set, along with the adoption of state-of-the-art data reduction and analysis techniques allowed an accurate study of the MP phenomenon. In summary, the present investigation has contributed to the characterization of this extremely interesting phenomenon through the detection of radial gradients among the number of stars belonging to different stellar populations in the Galactic GC NGC 2808 (Simioni et al. 2016). Moreover, the reduction of the entire sample of parallel Advanced Camera for Surveys observations has been carried out: the resulting catalogues are meant to be used as a reference for many future studies of different nature (Simioni et al. 2018).

The results coming from other ongoing researches are also presented. Specifically, the advent of the so-called chromosome maps has led to the classification

of Galactic GCs into type I and type II. The relations between this new classification and various properties of these systems have been investigated by means of a principal component analysis finding interesting aspects that merit further studies. Finally, the MP in the metal-poor, old Galactic GC NGC 6341 have been characterized. This cluster results to be compatible with being a type I one and the presence of a radial gradient in the distribution of the stellar populations has been investigated.

Resumen

A lo largo de las últimas decadas, importantes evidencias observacionales han revelado que los Cúmulos Globulares (CG) en la Vía Láctea albergan distintas poblaciones estelares. Representando clásicamente los mejores ejemplos en la naturaleza de Poblaciones Estelares Simples, estos nuevos hallazgos han puesto a los CG en el centro de atención. En particular, desvelar el origen del fenómeno llamado de las Poblaciónes Estelares Múltiples (PEM), es hoy en día un campo de investigación en Astrofísica muy activo.

De hecho, los CG desempeñan un papel clave en el estudio del comienzo de la formación estelar en el Universo y la evolución temprana de los sistemas estelares ya que son fundamentales para rastrear edades y la composición química en las galaxias a las que pertenecen. Esto es especialmente cierto para la Vía Láctea: los CG Galácticos son los objetos más antiguos para los cuales se pueden determinar edades absolutas con precisión; además, conocer la composición química detallada permite deducir las propiedades del medio ambiente en la época de formación.

Se están llevando a cabo grandes programas de observación con el objetivo de caracterizar mejor el fenómeno de las PEM y proporcionar restricciones para los modelos teóricos. En este contexto, la presente investigación hizo uso de los datos recopilados dentro del programa *Hubble Space Telescope UV Legacy Survey of Galactic Globular Clusters*. Estos datos exquisitos, junto con la adopción de técnicas de análisis y reducción de datos de vanguardia, permitieron un estudio preciso del fenómeno de las PEM. En resumen, la presente investigación ha contribuido a la caracterización de este fenómeno extremadamente interesante a través de la detección de gradientes radiales entre el número de estrellas que pertenecen a diferentes poblaciones estelares en el CG Galáctico NGC 2808 (Simioni et al. 2016). Además, se ha llevado a cabo la reducción de toda la muestra de observaciones en *parallel mode* de la *Advanced Camera for Surveys*: los catálogos resultantes están destinados a ser utilizados como referencia para

muchos estudios en varios ambitos (Simioni et al. 2018).

También se presentan los resultados de otras investigaciones en curso. Específicamente, el advenimiento de los diagramas llamados *chromosome maps* ha llevado a la clasificación de los CG Galácticos en tipo I y tipo II. Las relaciones entre esta nueva clasificación y las diversas propiedades de estos sistemas han sido investigadas por medio de un análisis de componentes principales y se encontraron aspectos interesantes que merecen estudios adicionales. Por último, se han caracterizado las PEM en NGC 6341, un CG Galactico viejo y pobre en metal. Este cúmulo resulta compatible con ser de tipo I y se ha investigado la presencia de un gradiente radial en la distribución espacial de las poblaciones estelares.

Sommario

Nelle ultime decadi, importanti evidenze osservative hanno rivelato che gli Ammassi Globulari (AG) nella Via Lattea ospitano popolazioni stellari distinte. Queste nuove scoperte hanno concentrato l'attenzione su questi sistemi perchè classicamente considerati il miglior esempio in natura di Popolazioni Stellari Semplici. In particolare, svelare l'origine delle cosiddette Popolazioni Stellari Multiple (PSM) è tutt'oggi un campo di investigazione astrofisica molto attivo.

Gli AG, infatti, giocano un ruolo chiave nello studio dell'inizio della formazione stellare nell'Universo e dei primi stadi dell'evoluzione dei sistemi stellari in quanto permettono di tracciare età e composizione chimica nelle galassie che li ospitano.

Questo è particolarmente vero per la Via Lattea: gli AG Galattici sono gli oggetti astronomici più vecchi per i quali può essere determinata con precisione ed accuratezza l'età assoluta; inoltre, conoscendo dettagliatamente la composizione chimica, è possibile dedurre le proprietà dell'intorno al momento della loro formazione.

Tutt'ora, importanti programmi osservativi sono attivi con lo scopo di caratterizzare il fenomeno delle PSM e produrre vincoli per i modelli teorici di formazione degli AG. In questo contesto, la presente investigazione fa uso dei dati raccolti nel programma *Hubble Space Telescope UV Legacy Survey of Galactic Globular Clusters*.

L'eccellente qualità delle osservazioni combinata a tecniche di riduzione ed analisi all'avanguardia, permette uno studio accurato del fenomeno delle PMS. Riassumendo, la presente investigazione ha contribuito alla caratterizzazione di questo fenomeno estremamente interessante attraverso il rilevamento di gradienti radiali del numero di stelle associate a popolazioni stellari distinte nell'AG Galattico NGC 2808 (Simioni et al. 2016). Inoltre è stata portata a termine la riduzione dell'intero set di osservazioni in *parallel mode* della *Advanced Camera for Surveys*: i cataloghi risultanti sono stati resi pubblici per essere utilizzati

come riferimento per altri studi, anche di natura differente (Simioni et al. 2018).

Sono anche presentati i risultati derivanti da ricerche attualemnte in corso. Specificamente, l'avvento delle cosiddette *chromosome maps* ha portato a classificare gli AG in tipo I e tipo II. Le relazioni tra questa nuova classificazione e varie proprietà di questi sistemi sono state investigate attraverso un'analisi di componenti principali trovando interessanti aspetti che meritano uno studio più dettagliato.

Infine, si sono caratterizzate le PSM nell'ammasso Galattico NGC 6341, un AG vecchio e poco metallico. Questo ammasso è risultato essere di tipo I ed è stato studiata la presenza di gradienti radiali nella distribuzione spaziale delle popolazioni strellari che ospita.

Contents

1 Introduction **1**
1.1 Stellar population of GCs 2
1.2 Properties of the MP phenomenon 3
1.3 Proposed models of formation of MP in GCs 5

2 Thesis Work **13**
2.1 The *HST* UV Legacy Survey of Galactic GCs 13
2.2 Thesis objectives 18

3 On the Cluster Type of Galactic GCs **21**
3.1 Introduction 21
3.2 Variables of the problem and PCA 24
3.3 Relations studied 30
3.3.1 Age-metallicity relation 30
3.3.2 [Fe/H] vs Galactocentric distance 33
3.3.3 Orbital parameters vs. cluster type 35
3.3.4 Cluster mass vs. cluster type 36
3.3.5 Spatial distribution of cluster types 37
3.4 Summary (Conclusion) 38
3.5 Appendix 39

4 ACS/WFC **Parallel-Field Catalogues** **45**
4.1 Introduction 45
4.2 Observations and Data Reduction 47
4.3 The Colour-Magnitude Diagrams and trichromatic stacked images 60
4.4 Selection of well-measured stars 63
4.5 Released Electronic Material 66
4.6 Summary and Conclusions 68

4.7 Extra material 69

5 Population gradients in NGC 2808 **87**
5.1 Introduction 88
5.2 Data and data analysis 89
5.2.1 Artificial Stars 92
5.3 The fraction of stars in the three MSs 92
5.4 Results 98
5.4.1 Crude estimate (Method I) 99
5.4.2 A more sophisticated estimate (Method II) 102
5.4.3 Theoretical interpretation 104
5.5 Summary and Conclusions 107

6 The MS of M92 **109**
6.1 Introduction 109
6.2 Observations and Data Reduction 110
6.2.1 Artificial-star tests 113
6.3 The Chromosome Map of M92 113
6.4 Population ratios and their radial distribution 117
6.5 Discussion 125
6.5.1 The Main Sequences of M92 127
6.6 Summary and Conclusions 131

7 Conclusion **133**

Bibliography **139**

List of Figures

1.1 Time evolution of the local values of the population ratio . . . 8
1.2 Fraction of total inital mass associated to diferent polluters . . 9
1.3 Fast rotating massive stars model 11

2.1 Reproduction of Figure 1 of Piotto et al. (2015) 16
2.2 Reproduction of Figure 11 of Milone et al. (2015b) 17

3.1 Example of chromosome maps 23
3.2 Eigenvectors projections 27
3.3 Age-metallicity relation 31
3.4 r_{GC} vs [Fe/H 34
3.5 Orbit inclination and eccentricity 36
3.6 GC mass 37
3.7 Spatial distribution of type I and type II GCs 38
3.8 Eigenvectors projections - bis 41

4.1 Finding charts: NGC 1261, NGC 1851, NGC 2298 and NGC 3201 53
4.2 Aperture corrections 55
4.3 Astrometric precision 60
4.4 Gaia-STScI offset 61
4.5 Resulting CMDs: NGC 1261 62
4.6 Trichromatic mosaic of NGC/,1261 64
4.7 Selection of well-measured stars 65
4.8 Finding charts: NGC 4590, NGC 4833, NGC 5024, NGC 5053, NGC 5286 and NGC 5466 70
4.9 Finding charts: NGC 5897, NGC 5904, NGC 5927, NGC 5986, NGC 6093 and NGC 6101 71

4.10 Finding charts: NGC 6121, NGC 6144, NGC 6171, NGC 6218, NGC 6254 and NGC 6304 72
4.11 Finding charts: NGC 6341, NGC 6352, NGC 6362, NGC 6366, NGC 6388 and NGC 6397 73
4.12 Finding charts: NGC 6441, NGC 6496, NGC 6535, NGC 6541, NGC 6584 and NGC 6624 74
4.13 Finding charts: NGC 6637, NGC 6652, NGC 6656, NGC 6681, NGC 6715 and NGC 6717 75
4.14 Finding charts: NGC 6723, NGC 6779, NGC 6791, NGC 6809, NGC 6838 and NGC 6934 76
4.15 Finding charts: NGC 6981, NGC 7089 and NGC 7099 77
4.16 Resulting CMDs: NGC 1851, NGC 2298, NGC 3201, NGC 4590 and NGC 5024 78
4.17 Resulting CMDs: NGC 5053, NGC 5286, NGC 5466, NGC 5897, NGC 5904 and NGC 5927 79
4.18 Resultin CMDs: NGC 5986, NGC 6093, NGC 6101, NGC 6121, NGC 6144 and NGC 6171 80
4.19 Resulting CMDs: NGC 6218, NGC 6254, NGC 6304, NGC 6341, NGC 6352 and NGC 6362 81
4.20 Resulting CMDs: NGC 6366, NGC 6388, NGC 6397, NGC 6441, NGC 6496 and NGC 6535 82
4.21 Resulting CMDs: NGC 6541, NGC 6584, NGC 6624, NGC 6637, NGC 6652 and NGC 6656 83
4.22 Resulting CMDs: NGC 6681, NGC 6715, NGC 6717, NGC 6723, NGC 6779 and NGC 6791 84
4.23 Resulting CMDs: NGC 6809, NGC 6838, NGC 6934, NGC 6981, NGC 7089 and NGC 7099 85

5.1 Finding chart for NGC 2808 90
5.2 CMDs of NGC/,2808 93
5.3 CMD regions used for stellar counts 94
5.4 Radial population ratios for NGC 2808 103
5.5 Time evolution of the radial population ratios for NGC 2808 . . 106

6.1 Selection of well measured stars 112
6.2 Selection of RGB sample 114
6.3 Completeness levels 115
6.4 Ridge lines used for the CM construction 116
6.5 CM of M92 118
6.6 1G/2G selection 119

6.7 Stellar populations statistical subdibvision 122
6.8 Width comparison between distinct stellar population distributions 123
6.9 Radial distribution of the population ratios 124
6.10 Color separation between stellar populations 128
6.11 Radial distribution II 129
6.12 MS of M92 130

List of Tables

3.1 GC properties considered for the PCA 24
3.2 The considered sample of Galactic GC 25
3.3 Principal components 26
3.4 Correlations between principal components and parameters . . 28
3.5 Spearman rank coefficients list 32
3.6 Oosterhoff type of type II GC 35
3.7 GC properties considered for the PCA - bis 40
3.8 Principal components - bis 40
3.9 Correlations between principal components and parameters - bis 42
3.10 HB index of type II GC 43

4.1 Observation log 48
4.2 Observation log (continued, I) 49
4.3 Observation log (continued, II) 50
4.4 Observation log (continued, III) 51
4.5 Aperture corrections 56
4.6 Aperture corrections (continued) 57
4.7 Astrometric solution precision 58
4.8 Astrometric solution precision (continued) 59
4.9 Catalogue for M4: an example 67
4.10 Information provided by each catalogue. 68

5.1 Observation log for NGC 2808 92
5.2 Population ratios for NGC 2808 97
5.3 Stellar masses for the three main populations of NGC 2808 . . 98
5.4 Population ratios 101
5.5 Slope and intercept values for population gradients in NGC 2808 (Method I) 102

5.6 Slope and intercept values for population gradients in NGC 2808 (Method II) 104

6.1 Population ratios 126

1

Introduction

Globular Clusters (GCs) are common constituents of galaxies and can be defined as dense aggregates of stars with a rough spherical symmetry (see for example the discussion in Meylan & Heggie 1997, Sec. 2). Our Galaxy, the Milky Way (MW), is not an exception and it hosts about 150 known GCs (Harris 1996, 2010 edition). While it is believed that most of MW GCs have been already discovered (Harris 2001), efforts are being devoted to study the specific frequency of them in other galaxies (e.g. Harris et al. 2017 and references therein). These systems, in fact, have typical masses of the order of $10^3 - 10^5\,M_\odot$ and half-light radii of the order of $1 - 10$ parsecs. Consequently, GCs have relatively small dimensions compared to the distance they have from the Sun[1] and thus their members can be safely considered to be all at the same distance. Their typical stellar density makes them also easily detectable. Even when there is no possibility to resolve the observed galaxy into single stars, its GC system can be studied as these stellar agglomerations results in bright 'stellar' objects in contrast to the diffuse light of the hosting galaxy. Before GCs could be observed in other galaxies, Shapley (1918) observed that in our Galaxy these objects define an extended system, centrally concentrated which trace the structure of the MW. More importantly, it was also observed that the Sun is not at the center of this system and, therefore, of our Galaxy. GCs have been ever since regarded as invaluable tools in order to characterize the structure of the MW (Zinn 1988 and reference therein) and in general of their hosting galaxies. Their importance is also due to the fact that they are known to be very old: with ages of the order of 13 Gyr, MW GCs are the oldest objects for which precise and accurate absolute ages can be determined

[1] The nearest is NGC 6121 (M 4) which is about 2 kpc away from the Sun.

(see e.g. Marín-Franch et al. 2009; Charbonnel 2016 and references therein). Moreover, GCs displays a broad range of metallicities with, in many cases, evidences of a bimodal distribution (Harris 2001 and reference therein). Even more interesting is that it indeed exists a metallicity gradient among MW GCs, with more metallic ones populating the most central regions of the Galaxy and metal poor objects populating the outer regions. In particular, Zinn (1985) demonstrated the existence of two distinct components among MW GCs, with different metallicities, spatial distributions and kinematics. The presence of at least two distinct groups of GCs, with a noticeable discontinuity in their spatial distribution, implies that each group could have different origin. And it is extremely fascinating that in general, albeit with some differences, bimodality seems to characterize the metallicity distribution function of GCs in galaxies (Harris et al. 2017).

1.1 Stellar population of GCs

In order to continue this introduction, and ultimately to properly contextualize the present work, it is mandatory to clarify what we refer to as stellar population. This concept is indeed the key to understand why GCs can really be considered a sort of laboratory (Renzini 1987; Renzini & Fusi Pecci 1988; Moehler 2001; Gratton et al. 2004; Gratton et al. 2012; Bono 2010). Since the first Hertzsprung-Russell (H-R) diagrams have been obtained, it has been observed that stars in the solar neighborhood occupy different loci with respect to those of GCs (see e.g. the discussion in Baade 1944). These findings supported the discovery of the coexistence in the MW of two populations of stars (Oort 1926). In particular, it was observed that the brightest part of the color-magnitude diagram (CMD) of MW GCs was composed only of red giant branch (RGB) stars and lack main sequence (MS) stars as opposed to solar neighborhood, where the MS is populated up to the brightest magnitudes. Another feature which at the time was found only in the CMD of GCs was the presence of the horizontal branch (HB) which occupy a region between the MS and the RGB. With the advancements in the field of stellar evolution it has became possible to interpret the observed H-R diagrams (and their observational counterparts, the CMDs) with theoretical models. It was soon realized that GC stars are old (Kraft 1979) and populate a very broad range of stellar evolution stages from main sequence (MS), to the red giant branch (RGB) passing through the turn-off (TO) and the sub-giant branch (SGB); up to the horizontal branch (HB) and the asimptotic giant branch too (AGB) (e.g. Arp et al. 1952; Oke & Schwarzschild 1952; Sandage & Schwarzschild 1952; Sandage 1953; Iben 1967). Given also the compact nature of GCs, and the observational evidence of the

virtual absence of dust inside these objects, it was commonly assumed that all the stars in a GC have the same age, the same (at least initial) chemical composition, and with stellar masses distributed according to an initial mass function (Kraft 1979, Smith 1987). These conditions, make GCs the best examples in nature of what is called a Simple Stellar Population (SSP) (Renzini 1981; also the number of binaries is generally lower than what is observed in the field Milone et al. 2012c). This has motivated extenisve and detailed investigations in the last half of the past century.

Early spectroscopic surveys of bright stars in Galactic GCs in the 70s have revealed that the inhomogeneities in metallicity among them have to be extendended to other chemical elements (Kraft 1979). Even more unexpected, was the presence of chemical inhomogeneities among stars in the same evolutionary phase of the same GC (Kraft 1979; Kraft 1994). In particular CN, CH and NH band strenght differences in stars of the same GC were among the first to be discovered (Smith 1987 and references therein). Further studies aimed at finding the origin of these inhomogeneities ultimately resulted in the discovery of anti-correlations between star-to-star light elemnt abundances (Kraft 1994; Gratton et al. 2004; Gratton et al. 2012). These anti-correlations are highly GC-specific and they are not observed, for example, among halo field stars; moreover, their presence has been detected, with different amplitude of the phenomenon, in various Galactic GCs (Carretta et al. 2010b). More recently, photometric evidences of the presence of complex stellar population have started to add up to the growing sample of spectroscopical observations (see for example Piotto 2009 for a review on early works). It is worth mentioning that, while spectroscopy is relatively limited in the number of stars that could be sampled both because of the need to observe bright stars and to the difficulties related to stellar crowding (which is a normal condition to face in studying the central region of Galactic GCs), photometry provides a good alternative to overcome these limitations. It is therefore easy to understand that, given the high number of stars involved in photometric studies of GCs (and thus the high statistical significance related to this), the observation of multiple main sequences (MSs) in the CMD of NGC 5139 ωCen (Bedin et al. 2004) or in the more *classical* GC NGC 2808 (Piotto et al. 2007), or even the splitting of the SGB in other Galactic GCs (Piotto et al. 2012) provided the final evidence to abandon the classical view of GCs hosting simple stellar populations.

1.2 Properties of the Multiple Stellar Populations phenomenon

As mentioned in the previous section, the growing sample of observational evidence (both from spectroscopical and photometrical) motivated the launching

of different projects aimed to survey the multiple stellar population (MP) phenomenon in Galactic GCs and to ultimately characterize its properties. At the current status of the investigation, the phenomenon is observed to have the following characteristics (Piotto et al. 2015; Renzini et al. 2015):

1. Ubiquity. In almost all the GCs studied so far it has been revealed the presence of multiple distinct stellar populations (Milone et al. 2017) and/or that of the Na-O anti-correlation (Carretta et al. 2009a). It thus appears that the occurrence of multiple stellar populations in GCs is an intrinsic property of the particular star formation processes in GCs;

2. Enrichment. In GCs, we observe a stellar population with chemical composition consistent with the proto-galactic composition (i.e. typical of the interstellar matter at the time it formed). In contrast, the other stellar populations present in the same cluster, are observed to have chemical composition with different amount of contamination due to hydrogen burning via the CNO-cycle and proton-capture processes at high temperatures. It follows that relatively massive stars of a first-generation (1G) contributed to accumulate the material out of which second-generations (2G) formed. Thus, a self-enrichment scenario is usually preferred (but see also Bekki et al. 2007).

3. Variety. The MP is occurring in GCs in many different modes and amplitudes. Milone et al. (2017) made a tentative subdivision among the general *appearance* that multiple stellar populations are observed to have in each GC, identifying two types of clusters. A similar effort, but taking into account different observables, has been reported in Smith (1987).

4. Discreteness. The current evidences indicate that MPs are observed to form distinct sequences or groups in CMDs and two-colour plots and are not consistent with continuous spreads or blends. This is less obvious from spectroscopic measurements (for example from observed Na-O anti-correlations) but there are some evidences that discreteness is present even in these measurements if sufficiently accurate and with a sufficient number of stars(Marino et al. 2008; Carretta 2014).

These observed properties are especially important when a model of GC formation is proposed. We recall here that, despite it is quite common among Galactic GCs, the chemical abundance pattern of 2G stars are scarcely found among Milky Way halo field stars (Martell & Grebel 2010; Carretta et al. 2010b). This suggest that these kind of stars are specific to GCs and can be generated only in this environment. Only later they started to populate

the Galactic halo as a consequence of tidal stripping from the cluster itself (Vesperini et al. 2010). It is important also to note that in many GCs, the fraction of 2G stars is comparable or even higher than that of 1G stars (Milone et al. 2017). These two conditions combined impose a strong constraint on the amount of processed gas needed to form the 2G. In all present self-enrichment scenarios, only a fraction of the total mass of the 1G can be produced to pollute the gas reservoir for 2G. This implies that the original mass of the cluster could have been larger than what is presently observed. Renzini et al. (2015) estimate that up to $80-90\%$ of the initial mass of the 1G should be removed to reconcile with what is presently observed. Finally, another piece of information comes from the fact that, even if the mean [Fe/H] varies from GC to GC, stars of the same cluster generally display high levels of homogeneity in metallicity. In fact it has been measured that, in many cases, the difference in iron abundance among stars of the same cluster is lower than 0.1 dex (Carretta et al. 2009c). Albeit there are some exceptions (see e.g. Piotto et al. 2015), this indicates that in general, supernova explosions do not contribute to the contamination of the material of 2G. On the contrary, it is more likely that these events play a role in halting the star formation in GCs (D'Ercole et al. 2008).

1.3 Proposed models of formation of MP in GCs

At the light of the above mentioned observed properties of the MP phenomenon, a number of theoretical scenarios for the formation of distinct stellar populations in GCs has been proposed. Since the early discovery of chemical non-homogeneities among GC stars, many hypothesis have been inferred (see for example Smith 1987). But, given the peculiar abundance pattern observed for GC stars, the nowadays preferred scenario is the one of a group of stars of a first (primordial) generation that acts as polluter for the material that subsequently forms 2G stars (Renzini 2013; Bastian et al. 2015; Renzini et al. 2015). In this respect four kinds of polluters are at the base of the most known proposed formation scenario of GC formation and in the following we provide a brief description of them. We remand to Bastian et al. (2015) and Renzini et al. (2015) for recent discussions about their viability. Interestingly enough, at the current state of investigations, none of the proposed models of GC formation seem to successfully reproduce the whole set of observational constraints.

A largely investigated class of polluters are AGB stars and, in particular, those where the hot-bottom burning (HBB) process is active (e.g. D'Ercole et al. 2008 and reference therein). HBB AGB stars have been shown, in finely tuned models, to be capable of ejecting processed material at relatively low velocity ($\sim$ 10 km/s) that can in principle be retained by the gravitational

potential of a typical GC. As anticipated, the abundance pattern of the HBB AGB yield is highly model dependent (D'Ercole et al. 2010), but in general it is not trivial to match the widely observed Na-O anti-correlation with this kind of polluters. Nonetheless, HBB AGBs are suitable candidates for the explanation of the helium enrichment of 2G stars (Slemer et al. 2017; but see Bastian et al. 2015 and the discussions in Renzini et al. 2015) and their winds could contribute to the formation of a cooling-flow in the relatively short interval of time between the end of 1G supernovae type II explosions and the appearence of the first 1G supernovae type Ia (D'Ercole et al. 2008, D'Ercole et al. 2010, Renzini et al. 2015, Bekki et al. 2017). One of the fundamental limitations that these kind of pulleters seem to have is that the total yield coming from AGB HBB stars must be only a fraction of the original total mass of 1G. As discussed in the precedent section, 1G stars, have a chemical pattern which is fairly common in the MW halo and, possibly, it is not difficult to imagine that in origin GCs were more massive than what we observe today. But losing 1G stars alone cannot entirely solve the problem. In order to match the observed anticorrelation, some dilution with pristine, unprocessed, gas seems to be mandatory (D'Antona et al. 2016). A possible way to mitigate this effect was explored in D'Ercole et al. (2010), where the authors assign a non-canonical IMF to 2G stars, preventing the formation of massive stars. Renzini (2013), instead, suggested an improved star formation efficiency as a possible way out. Another solution, comes from the assumption that GC formed at high redshifts in systems analog to the nowadays dwarf galaxies which subsequently merge with the MW (for recent simulations see for example Bekki et al. 2017). In summary, at the current status of investigations, the scenarios involving AGB stars as polluters, and in particular those experiencing HBB, appear to be worth deeper investigations. Nonetheless, at the current state of knowledge and due to the present-day difficulties in reproducing the observational data, it cannot be stated that they should be regarded at as the only possible scenario. To conclude, an important consequence of this scenario that is relevant to emphasize, is that, 2G stars are expected to form in the central part of the cluster (D'Ercole et al. 2008). Strong constraints for this scenario are thus expected to come from the study of radial gradients of stellar populations in GCs. In particular, 2G stars are expected to be more centrally concentrated than 1G stars. However, one in search of such signature must face the fact that GCs are very old, of the order of 13 Gyr-old thus there is plenty of time for dynamical effects to mix stellar populations together. Vesperini et al. (2013) investigated in detail this aspect and demonstrated that, an initially more concentrated 2G, in the presence of 1G stars, progressively diffuse till complete mixing is reached. The velocity in doing so is regulated by the structural parameters of the cluster, such as mass

and concentration (which regulate the relaxation time of a GC). This study also demonstrated that mixing occurs first in the central region, while stellar population gradients could be in principle detected for longer periods including measures referred to the outskirts of GCs.

For the sake of completeness Figure 1.1 reproduces Figure 7 of Vesperini et al. (2013) where it is possible to see the evolution of the radial gradient of the ratios between local number of 1G and 2G stars (population ratio). In particular, it is possible to note that, close to the GC center the steepness of the gradient rapidly decrease with time, with respect to what happens in the outer regions. What results is that in the central regions the gradient flattens with time and the local population ratio progressively match the values found in the outskirts of the GC. On the other hand, the gradient in the outer regions is relatively flat since the beginning with only a shift of the local value of population ratio to higher values, but with a different speed with respect to what happens in the central regions. It follows that, even if the gradient of the population ratio becomes relatively flat in the inner cluster regions, including the outskirts of the GC in the sample allows the detection of gradients even in dynamically old clusters.

Massive interacting binary systems have also been regarded as viable alternative polluters for the intracluster medium (e.g. de Mink et al. 2009). In these systems, the material processed by hydrogen burning is transferred between the two companions and a fraction of it forms a circumbinary disk. This gas reservoir is then progressively expelled via low velocity winds, a condition wich is mandatory for the processed material to be retained by the gravitational potential of the cluster. Even in this case, to quantitatively match the observed abundance pattern a small degree of mixing with primordial gas seems to be needed. Nonetheless, in the de Mink et al. (2009) formulation, the total mass ejected from these systems appears to be higher than in the HBB AGB case and lessen the problem of generating such high number of second generation stars (see Figure 1.2).

This apparent advantage has been questioned with the simple argument that a relevant fraction of the ejected mass, comes from stars of more that $10M_{\odot}$. It follows that these stars are likely to produce their ejecta at the same time Supernovae Type II explosions are occurring in the cluster, preventing the formation of the cooling flow (Renzini et al. 2015). A variant of this scenario has been presented in Bastian et al. (2013) where it is proposed that the ejecta of massive interacting binary stars may be accreted directly by fully-convective lower-mass stars still in the Hayashi line. In this scenario, the internal dynamics of the GC plays a crucial role, since stars that passes through the cluster center are likely to accrete more processed material than stars that spend more time

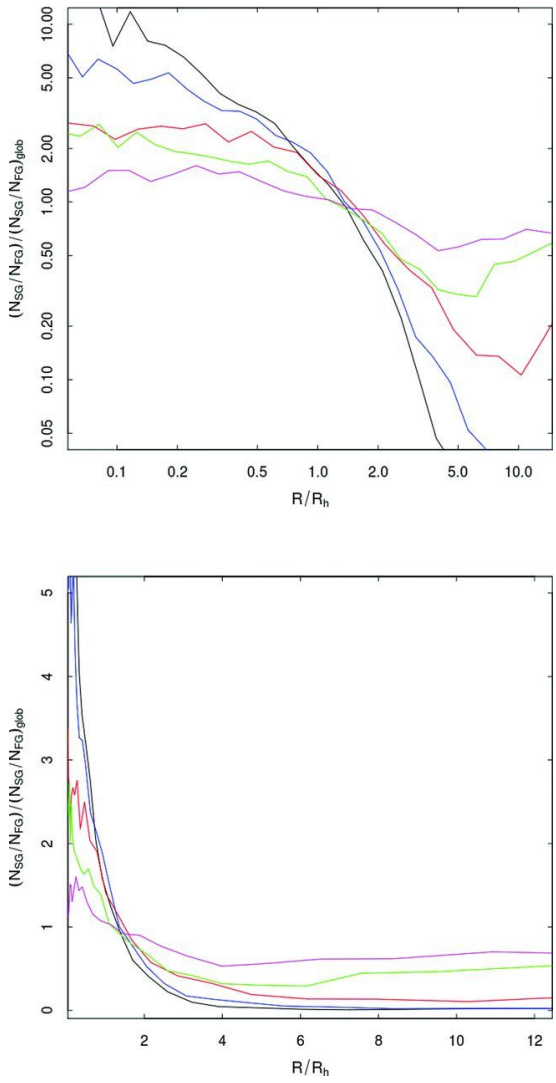

Figure 1.1: Reproduction of Figure 7 of Vesperini et al. (2013). Time evolution of the local values of the ratio between the nuber of 1G and 2G stars (population ratio) normalized to the global value of the same quantity, as a function of radial distance from cluster center (in units of the half-mass radius R_h). In the upper panel, the adoption of log-log scale allow to inspect in more detail the behaviour of the local population ratio at small radial distances. Lines of different colours refer to different ages of the system in units of the initial half-mass relaxation time ($t_{rh}(0)$); black line refers to $0.2t/t_{rh}(0)$, the blue one to $1t/t_{rh}(0)$, the red one to $5t/t_{rh}(0)$, the green one to $15t/t_{rh}(0)$ and finally the magenta line refers to $45t/t_{rh}(0)$.

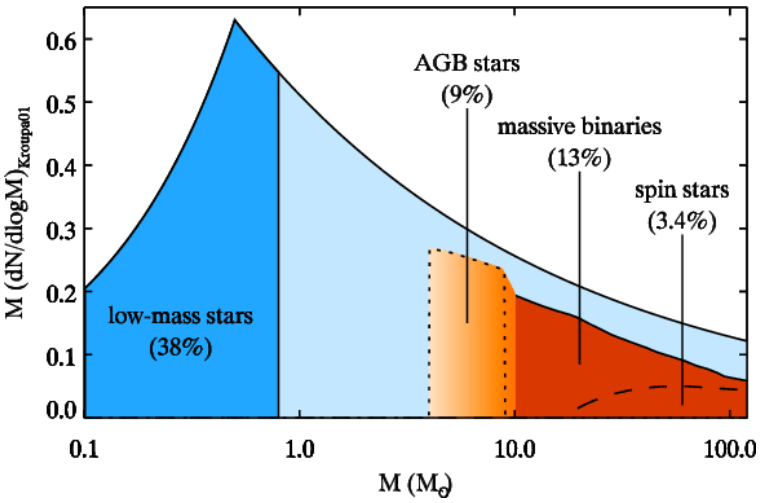

Figure 1.2: Reproduction of Figure 2 of de Mink et al. (2009). Adopting a Kroupa (2001) IMF, the authors have calculated for distinct polluters the fraction of GC total mass associated to them. It can be seen that, of the total initial mass of the GC, $\sim 9\%$ results to be associated to AGB stars, while massive stars represent $\sim 13\%$. The authors also estimated that fast rotating massive stars constitute $\sim 3.4\%$ of the total initial mass function.

in the outer regions, where density is lower. Therefore, in this way, a collapsing cloud to form 2G stars is not needed and, also, the problem of the fraction of 2G with respect to 1G stars is further mitigated. Nonetheless, this scenario is subject to the same limitations of the one by de Mink et al. (2009). In fact, 2G stars are observed to be virtually not contaminated by Supernovae products. In addition, given that in the scenario by Bastian et al. (2013) the accretion mechanism works differently for each single star depending on many factors, it becomes more difficult to justify the presence of discrete sequences in the observed CMD. An intrinsic broadening of the sequences is more likely.

Another class of polluters, are fast rotating massive stars (Krause et al. 2013). In this scenario, massive stars (40 to 120 $M_\odot$) are subject to rotation that fosters the ejection of material processed by hydrogen-burning at high temperatures and generates what is called a decretion disk. It is proposed that 2G stars are generated in this dense local environment. A schematic view of the proposed model is reported in Figure 1.3 (from Krause et al. 2013).

Also for this case Renzini et al. (2015) reported some criticism. In particular, as for the Bastian et al. (2013) model, since 2G stars formation is assumed to be active in the same epoch of Supernovae Type II explosions, it is unlikely that any contamination from the product of the explosion could be avoided. And this is in contrast with what is observed. Another similitude with the previous case, and again a crucial point, is that the proposed method of generation of 2G stars implies a continuous distribution of values of chemical abundances. This would produce intrinsically broad sequences in the CMDs as opposed to the discrete, narrow sequences that are observed. Another interesting aspect that (Renzini et al. 2015) pointed out is that the proposed method of 2G stars generation is not GC specific and that does not fit with the observed small fraction of 2G stars observed in the halo of the Milky Way.

Finally, in recent years, it has been also suggested that supermassive stars (of the order of 10^4 $M_\odot$) may have formed in the central region of young GCs and the nuclear reactions that took place in their interiors could have produced the right chemical abundance pattern for 2G stars (Denissenkov & Hartwick 2014, Denissenkov et al. 2015). These kind of stars have not been observed in nature so far, but the authors suggest that the detection of intermediate-mass black holes in GCs should provide strong indication of their presence in the past. Apart from the problem of the existence of these objects, the model suffers from similar limitations as the precedent. In particular, given the high mass, the evolution of these massive stars must be very rapid and the gas accumulation phase results to be contemporary to the Supernovae Type II explosions. Moreover, a relatively limited mass range is required in order to reproduce the correct chemical abundance pattern of 2G stars. Thus, only a

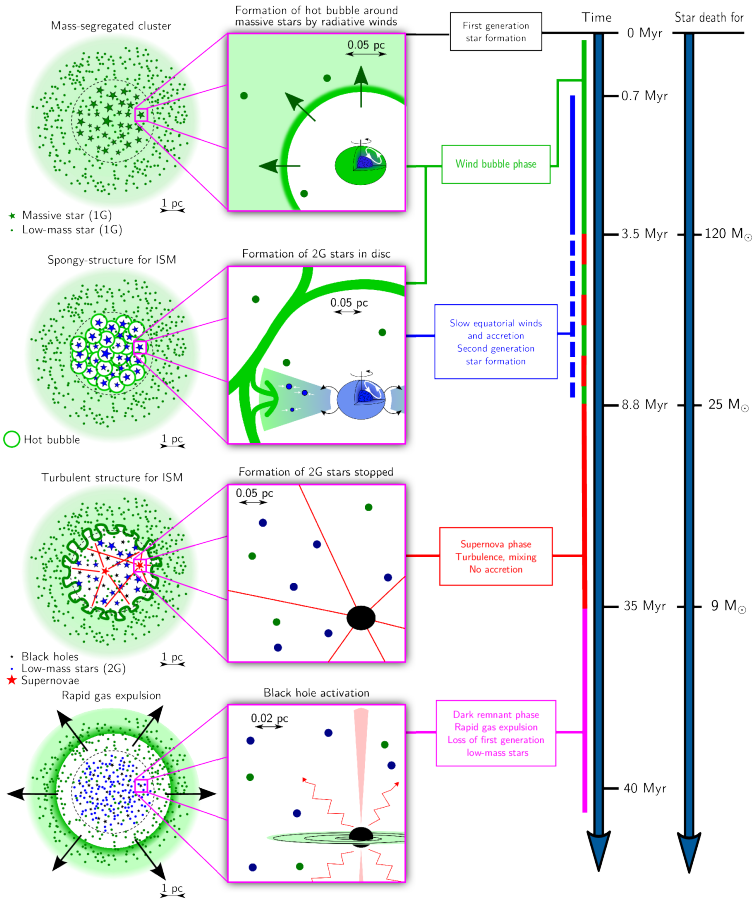

Figure 1.3: Reproduction of Figure 1 of Krause et al. (2013). A proposed schematic model for massive rotating stars as polluters. Massive rotating stars, segregated in the center of the cluster, generate an ejection of proccessed material that forms what is called a decretion disk. 2G stars are thus expected to be born in this dense local environment within ~ 10 Myrs after 1G stars have formed. This episode of star formation is subsequently interrupted when 1G massive stars begins to enter the supernova phase and the decretion disk is blown away from the cluster by the strong stellar winds. In this phase, it is also expected the loss of a significant fraction of low-mass 1G stars that populates the outer regions of the primordial cluster.

small fraction of processed material could be produced, too low to match the observed number of 2G stars in present day GCs.

2

Thesis Work

The dicovery of the MP phenomenon led to a rethinking not only on how GCs forms but also on their role in the formation of their hosting galaxies. For this reason, a multitude of studies has been carried out in the last decade focusing on both the characterization of the phenomenon and the interpretation of the observational results. It is therefore mandatory to further contextualize the thesis work before summarizing the specific objectives.

2.1 The *HST* UV Legacy Survey of Galactic GCs

As reported in the previous chapter, photometric detection of multiple distinct sequences in the CMD of Galactic GCs plays a key role in highlighting the inadequacy of the classical view to represent observations and to shed new light on the chemical abundance differences detected by spectroscopic studies. One of the main reason is that photometry allows to sample large numbers of stars in an homogeneous manner and to study them consistently thus increasing the statistical relevance of the chemical abundance differences among groups of stars. Another aspect that needs to be underlined, is that photometry, intended as a sort of very low resolution spectroscopy, allows also to reach fainter magnitudes, thus enabling the study of low mass stars in the MS phase. The early detection of multiple MSs in the CMD of Galactic GCs led to the establishment that mixing in the stellar interiors, due to stellar evolution (i.e. transition from MS phase to RGB one) cannot be the only mechanism involved in creating the observed chemical patterns. More likely, the chemical differences observed are intrinsic of the gas out of which the stars are formed (see for example Bedin et al. 2004 and Piotto et al. 2007 for early detection of multiple MS). But as

highlighted in detailed spectroscopic studies, chemical differences among GC stars involve specific elements and for this reason not all filter combinations are equally valid in order to highlight them photometrically. In particular, it has been demonstrated in various studies that the observed chemical differences manifest themselves more in the UV part of the electromagnetic spectrum (e.g. Bellini et al. 2010; Milone et al. 2010; Sbordone et al. 2011; Milone et al. 2012b; Piotto et al. 2013). Unfortunately, until few years ago, there were no large, homogeneous photometric surveys of GCs that sampled that wavelenght interval. To fill this gap is one of the main goal of the *Hubble Space Telecope* (*HST*) UV Legacy Survey of Galactic GCs: Shedding Light on Their Populations and Formation (GO13297, PI: Piotto; Piotto et al. 2015). The present thesis work makes extensive use of the data collected in this photometric survey and this section is dedicated to describe it in more detail.

As the name of the survey suggests, data have been obtained with the instruments onboard *HST*. Many photometric studies have proven the advantage of space-based photometric observation, and the exquisite spatial resolution combined with the stability of the point spread function (PSF) are mandatory for the survey. Moreover, the wavelenght interval that needs to be sampled is not accesible to ground-based telescopes. Different *HST* instruments have been used in precedent large photometric surveys (e.g. Piotto et al. 2002; Sarajedini et al. 2007) and in the case of GO13297, the Wide Field Camera 3 (WFC3) has been chosen to observe the central part of 57 GCs. These clusters represent a subsample of 56 out of the total 67 nearby Galactic GCs that were observed with the Advanced Camera for Surveys (ACS) in the older ACS Survey of Galactic GCs (Sarajedini et al. 2007), for wich F606W and F814W observations were collected. In addition to these, observations of the open cluster NGC 6791 have been collected. Taking advantage of the Parallel Observation mode, ACS exposures have also been obtained for the outer regions of the majority of the observed GCs, to enhance the spatial mapping. For these exposures, the filters F475W and F814W of the Wide Field Channel (WFC) of the camera have been used because no bluer filters than F435W are available. It is interesting to note here that this filter combination provide a relatively large color-baseline and for this reason it is particularly indicated to detect differences in temperature among stars which, at a given magnitude, could be produced by differences in helium abundances (see for example the case of the triple MS of NGC 2808 by Piotto et al. 2007). Another important aspect is that the CMDs obtained in the visible/NIR part of the spectrum are deeper than those obtained with UV filters (the lower stellar density in the outer regions also plays an important role) and this implies that the ACS parallel observation are more suitable to study the low-mass MS stars. In summary, the *HST* UV Legacy Survey of

Galactic GCs not only complements previous *HST* photometric surveys with a combination of UV filters suitable to characterize the MP phenomenon in a homogeneous and consistent way, but also extends their spatial sampling providing high precision astrometric and photometric catalogues also for the outskirts of the majority of them.

Few words more on the particular filter choice adopted to image the central regions of the GCs will be spent in the following. It is important to underline that most of the stars lie in the cluster centers and, if crowding is properly taken into account, it becomes possible to identify even very tiny features in the CMD. As anticipated, since the early spectroscopic studies of the '70s it is known that the chemical abundance differences among GC stars are mainly due to nitrogen, oxygen and carbon variations, the elements involved in the CNO-cycle. Recent photometric studies have also demonstrated that combinations of WFC3 F275W, F336W and F438W filters are very efficient in separating the sequences of stars with different C, N , O abundances in all the CMD regions. The reason is that specific spectral lines fall in the passband of each of these filters (e.g. Milone et al. 2012b; Milone et al. 2018).

Figure 2.1 clearly shows that each filter adopted in the UV Legacy Survey covers spectral lines created by specific chemical elements. In particular, the F275W passband contains the absorption lines of OH molecule, F336W passband is dominated by the absorption lines of NH molecules, while absorption lines of CN and CH molecules are present in the passband of the F438W filter. Figure 2.1 also shows how the typical chemical patterns of FG stars (in red) and SG stars (in blue) shape the spectra in such a way that the difference in their chemical abundances are evident in the wavelength range covered by the selected filter. In this respect, it is interesting to note that the index $c_{F275W,F336W,F438W} = (\mathrm{F275W} - \mathrm{F336W}) - (\mathrm{F336W} - \mathrm{F438W})$ defined in Milone et al. (2013) has been found to be particularly useful in enhancing the separation in colour among distinct stellar populations in the CMD of GCs. This pseudo-colour, along with the F275W − F814W colour has been recently used by Milone et al. (2017) to construct the two-pseudo-colour diagrams named chromosome maps which allow not only the characterization of the multiple stellar populations in the target GCs, but also a new classification of them into two categories: Type I GCs and Type II ones. Further details on this topic will be given in the following chapters.

For the sake of completeness, we corroborate Figure 2.1 with a reproduction of Figure 11 of Milone et al. (2015b). In Figure 2.2 it is possible to see how abundance differences of specific elements affect the spectra of a star (left panels) and how this translates into colour differences relative to various combinations of *HST* filters (right panels). In the first lines, the effect of C, N

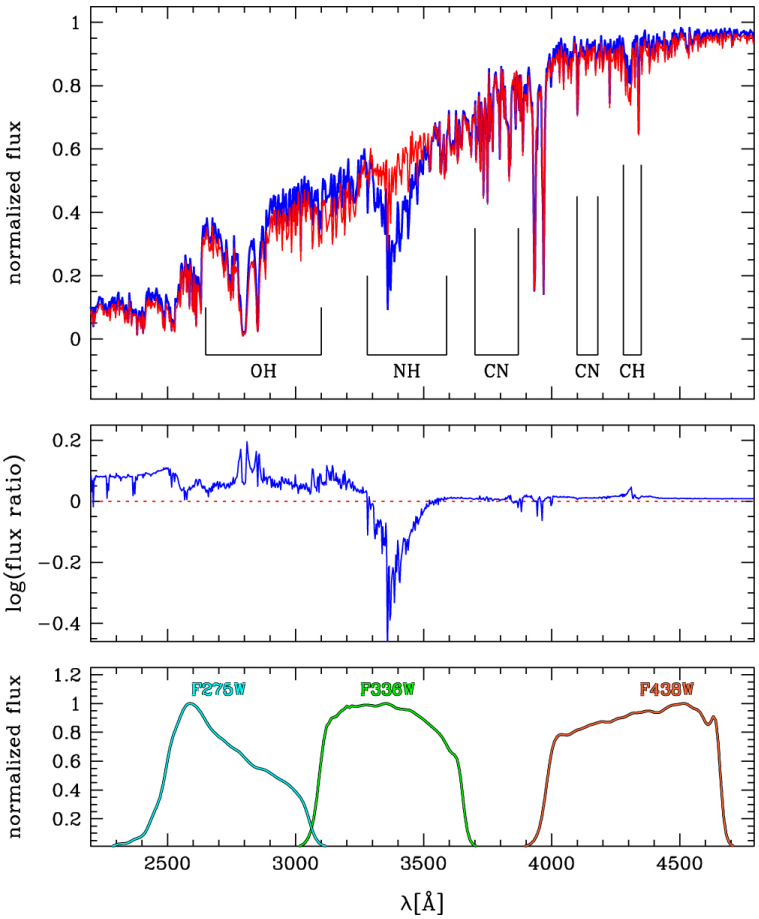

Figure 2.1: Reproduction of Figure 1 of Piotto et al. (2015). The synthetic spectrum of a FG star (in red) is compared with one of a typical FG star wich result to be Oxigen- and carbon-depleted while enhanced in nitrogen. In the lower panel the filter transmissivities are shown for the filters used in the UV Legacy Survey. It can be noted that F275W filter bandpass include the OH line while the F438W filter bandpass include the band of CN and of CH. The SG star in this case appear brighter than the FG star. On the contrary, the FG star appears brighter than the SG one in the F336W filter, where the NH band falls in the relative bandpass.

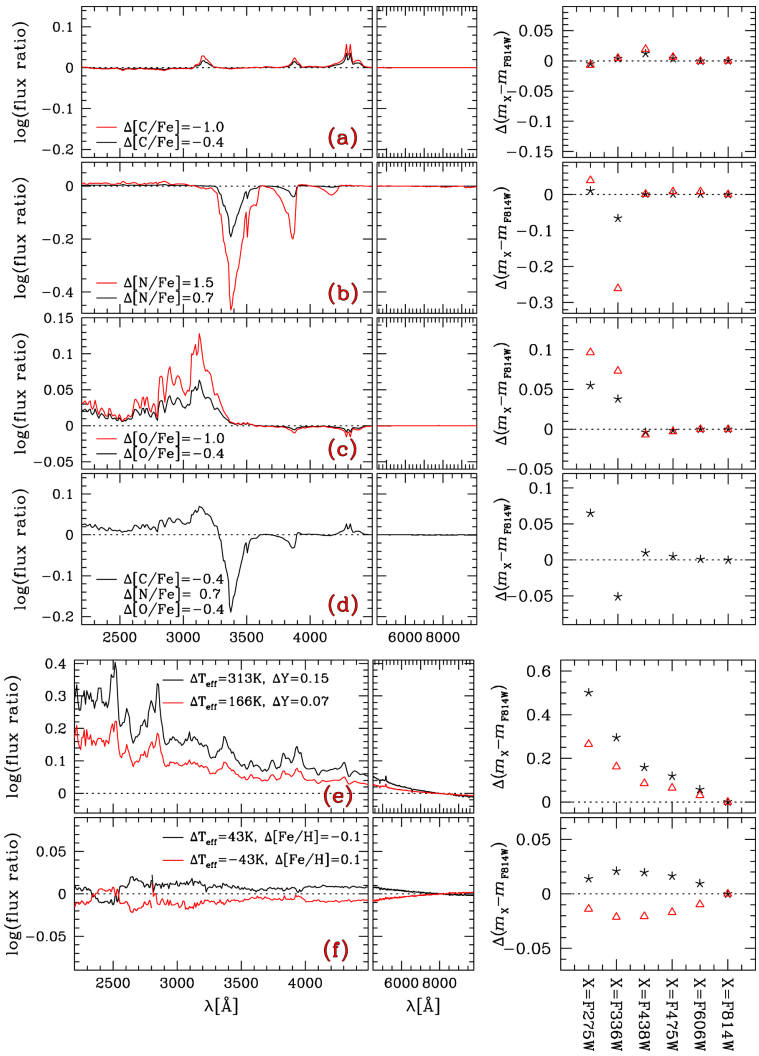

Figure 2.2: Reproduction of Figure 11 of Milone et al. (2015b). Effect of different chemical abundances with different *HST* filter combination. Left panels, ratio between the synthetic spectra of a reference star and those with different chemical abundances as specified in the legend of each panel. Right panels, expected colour separation between the sequences of the different stellar population with different filter combination. The first rows refers to changes in the carbon abundance only (panel a), nitrogen only (panel b), oxygen only (panel c) and C,N and O combined (panel d). The expected effect of different helium contents is reported in panel f while panel f refers to different iron abundances.

and O abundance variations are shown both for single elements and combined. Again, the values used for the abundance are those typical for FG and SG stars. It is possible to observe that, in this case, only the bluer part of the spectrum is affected. Consequently, the expected color spread involving visible filters like F475W − F814W (as in the case of the ACS parallel observations) or F606W − F814W (as in the past ACS Survey of Galactic GCs) is practically negligible. On the contrary, as already mentioned, the three WFC3 filters selected for the UV Legacy Survey are particularly sensitive to variations of such chemical elements and this translates into colour differences of the order of 0.05 magnitudes with C variations giving the lowest signal. Things changes if helium and iron are taken into account and in this case, especially for Fe, also visible filters acquire some sensitivity and can thus be used to reveal the presence of distinct stellar populations in the CMD. Even if He abundances are not easy to be measured directly with spectroscopy, observational evidences suggest that, albeit some isolated cases (e.g. NGC2808), there is not large He spread among GC stars (Lagioia et al. 2018 and references therein; Milone et al. 2018). Also for the case of iron spread, observations show similar results with the majority of the clusters being relatively homogeneous in the Fe abundance of their stars (Carretta et al. 2009c) with some noticeable exceptions (like e.g. ωCen).

Having this said it is motivated the need to complement the past photometric surveys with the new UV Legacy one, adopting this new set of filters. It is also clear the use of *HST*, as it is the best instrument to reach the photometric and astrometric precision mandatory to properly characterize the MP phenomenon. This last requirement is achieved thanks to the use of techniques and software specifically adapted and developed for this survey (Piotto et al. 2015; Nardiello et al. 2018b and references therein).

2.2 Thesis objectives

In the following, the scientific objectives achieved in the context of the *HST* UV Legacy Survey of Galactic GCs by the present thesis work are resumed.

Recent results on multiband photometry demonstrated that combinations of UV and visible filters are particularly suited to identify multiple sequences in the CMD of all surveyed Galactic GCs. In particular, the creation of the so-called Chromosome Maps led to a new classification of the Galactic GCs in two category, type I and type II, based on the qualitative comparison of features in these two-colour diagrams (Milone et al. 2017). In the light of this new classification, possible relations among cluster type and various GC parameters have been studied. To quantify the level of correlation, a principal component analysis has been performed. Interesting cases have been subsequently studied

in details. The results are presented in Chapter 3.

One of the main objectives of the present thesis is to reduce and analyze all the ACS parallel observation obtained in the context of the *HST* UV Legacy Survey. The entire data sample has been reduced and photometric and astrometric catalogues have been produced. The material has been presented in Simioni et al. (2018) and is described in detail in Chapter 4.

A second major objective of the thesis is to make use of the ACS parallel data in order to exploit their scientific potential. This has been demonstrated in Simioni et al. (2016). In that work ACS parallel observations of the outskirts of the Galactic GC NGC 2808 have been integrated with WFC3 UV data of the central regions in order to study the radial gradient of distinct stellar populations hosted by this cluster. The work is presented in Chapter 5.

Finally, the MP phenomenon has been characterized in detail in the low-metallicity, old galactic GC NGC 6341 (M92). Also in this case, a tentative connection between WFC3 data of the central region and ACS parallel observation data of the outskirts of this cluster has been investigated. The results are presented in Chapter 6.

3

On the Cluster Type of Galactic Globular Clusters

Abstract

As outlined in Milone et al. (2017) and Marino et al. (2018), the analysis of chromosome maps of Galactic Globular Clusters permits to classify them into type I and type II clusters. In this work, we have performed Principal Component Analysis in order to explore possible correlations among some parameters of Galactic Globular Clusters in the light of this new classification.

3.1 Introduction

Seen as a single system, the Galactic Globular Clusters (GCs) have been classically used to establish the non-preferential position of the Sun with respect to our Galaxy. Being also the oldest astronomical objects for wich reliable ages could be estimated, they have been also used to put strong constraints to cosmological theories. In the Milky Way (MW) they have been found to populate a spheroid that extends out to various tens of kiloparsecs from the center of our Galaxy. A multitude of studies have been oriented to them in order to find hints on MW formation processes.

For the first time, Zinn (1985) provided evidence that pointed to the existence of distinct sub-populations of GCs inside the MW. In his work, a halo population was detected in the Galaxy along with a disk population. GCs associated to the halo population seem to be characterized by lower metallicity and a small net rotation around the Galactic center. On the other hand, the

disk population is more metal rich and has been found to have a velocity close to that of the local standard of rest. At that time, this was used to promote the vision that, at least part of MW GCs have extragalactic origins and were later incorporated into MW via merging processes.

Since then, an increasing number of refinements in the number and components of distinct GC populations in the MW have been proposed. Ibata et al. (1995) discovered the Sagittarius dwarf galaxy. Its chemical and kinematical patterns have been detected in a large area of the sky supporting the idea that this satellite of the MW is being subject of tidal stripping. The authors, also suggested that some MW GCs are likely part of this galaxy. The existence of others nearby, stripped dwarf galaxies has been proposed, along with a list of GCs likely associated with them (see for example Marín-Franch et al. 2009 — hereafter MF09).

More recently, in the first decade of this century, the advent of deep, high resolution photometry of Galactic GCs, led to the detection of distinct and detached sequences at different stellar evolutionary stages in the Color-Magnitude Diagrams (CMD) of these objects. This result, coupled with the growing number of spectroscopical evidence, was interpreted in terms of multiple stellar populations (MSP). It is worth mentioning that distinct sequences of stars, that appear detached in the CMD, put strong contraints to modelling the processes of star formation in GCs. This evidence, in fact, rules out a continous star formation process and suggests that bursts of star formation have occurred in these systems.

At first, the MSP phenomenon was detected in single GCs, leading to a growing number of them being considered peculiar. But it was only with the completion of a large photometric survey, namely the *Hubble Space Telescope* (HST) UV Legacy Survey of Galactic Globular Clusters (PI Piotto, Piotto et al. 2015 — hereafter Paper I), that it has been demonstrated that this phenomenon is a common characteristic of virtually all Galactic GCs (Paper I; Milone et al. 2017 — hereafter Paper IX).

Even more interesting is that, with the introduction of the chromosome maps (Paper IX), MW GC population has been once again subdivided. Indeed, in Paper IX it has been shown that the chromosome maps of the majority of the observed GCs show the presence of two major distinct groups of stars (1G population and 2G population). Samples of stars taken from these two groups display chemical abundance differences in light elements; for example the well known Na-O anticorrelation. These clusters have been addressed to be type I clusters.

The other GCs show more complex chromosome maps: other groups of stars can be detected, in addition to the two groups present in type I clusters,

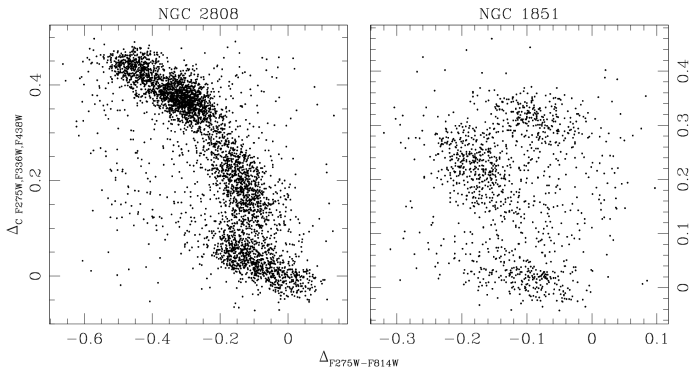

Figure 3.1: A collection of two chromosome maps. In particular, NGC 2808, on the left, is the prototpe of type I clusters. It shows a chromosome map that is composed by a low, horizontal part and an upper feature elongated in the vertical direction. By contrast, the chromosome map of NGC 1851, is characterized by the presence of additional features which enhance the complexity.

all with their own Na-O anticorrelation, but with different Ba and Fe abundances. GCs that have chromosome maps of this kind are defined as type II clusters. To date, 10 type II clusters have been detected: NGC 362, NGC 1261, NGC 1851, NGC 5139, NGC 5286, NGC 6388, NGC 6656, NGC 6715, NGC 6934 and NGC 7089 (Paper IX).

We provide an example in Figure 3.1, where two chromosome maps of NGC 2808 (a type I GC) and NGC 1851 (a type II GC) are shown. The distribution of points in NGC 2808 is characterized by an horizontal part and a vertical feature. The horizontal distribution defines the 1G population, while 2G population groups all the points distributed in the vertical part of the map. This morphology is commong among all type I GCs. In the chromosome map of NGC 1851 additional features can be detected along with the ones observed in type I GCs.

In this work we have performed a principal component analysis (PCA) in order to investigate the correlation of cluster type with other GC parameters. The structure of this paper is as follows: in Section 3.2 we present the details of the PCA and briefly discuss the results. In Section 3.3 possible relations among various cluster parameters are presented in more detail. In particular,

Table 3.1: GC properties considered for the PCA. They will be identified in the following with the identification number provided in the first column. In the third column we report the sources from where values have been taken. References are: i, Paper IX; ii, Catelan (2009); iii, Zorotovic et al. (2010); iv, Sollima et al. (2010); v, van den Bergh (2011); vi, Kunder et al. (2013); vii, Carretta et al. (2009c); viii, MF09; ix, Dinescu et al. (1999); x, Gnedin & Ostriker (1997); xi, Harris (1996, 2010 edition).

	Description	References
1	Cluster type	i
2	Oosterhoff type	ii; iii; iv; v; vi
3	Metallicity	vii
4	Relative age	viii
5	Total energy of the orbit	ix
6	Total angular momentum	ix
7	Orbit eccentricity	ix
8	Orbit inclination with respect to the Gal. plane	ix
9	Cluster mass	x
10	Core radius (parsec)	xi
11	Tidal radius (parsec)	xi

we reviewed the age-metallicity and age-Galactocentric distance relations (Section 3.3.1); the metallicity vs. Galactocentric distance relation (Section 3.3.2); the relation between orbital parameters and cluster type (Section 3.3.3); the mass distribution (Section 3.3.4); and finally the spatial distribution of GCs (Section 3.3.5).

3.2 Variables of the problem and Principal Component Analysis

We have investigated a large sample of variables through principal component analysis. In particular, we focus on 11 quantities, reported in Table 3.1: cluster type, Oosterhoff type, metallicity, relative age, orbit total energy, orbit total angular momentum, orbit eccentricity, orbit inclination with respect to the Glactic plane, cluster masses, core radii and tidal radii. These quantities have been collected from several catalogues that provide information for different GC samples. Our final sample consist on 25 GCs, 6 of them of type II and the rest of type I. The 6 type II clusters are NGC 362, NGC 1851, NGC 5139, NGC 6656, NGC 6934, NGC 7089. The full list of parameters of our sample is given in Table 3.2.

Table 3.2: The considered sample of Galactic GC. For each cluster the values of the parameters used in the PCA are given. Labels in the first row identify the parameters, according to the designations given in Table 3.1. They are respectively: cluster type (1), Oosterhoff type (2), metallicity (3), relative age (4), total energy of the orbit (5), total angular momentum (6), orbit eccentricity (7), orbit inclination with respect to the Galactic plane (8), cluster mass (9), core radius (10), tidal radius (11).

Parameter:	1	2	3	4	5	6	7	8	9	10	11
					($10^2\,km^2\,s^{-2}$)	($kpc\,km\,s^{-1}$)		(deg)	($M_\odot$)	(pc)	(pc)
NGC 104	I	II	-0.76	1.02	-872	1274.0	0.17	29	1.45e+06	0.4712	55.36
NGC 288	I	II	-1.32	0.83	-787	654.1	0.74	44	1.11e+05	3.4950	34.15
NGC 362	II	I	-1.3	0.81	-856	358.0	0.85	21	3.78e+05	0.4503	25.91
NGC 1851	II	I	-1.18	0.78	-340	2259.0	0.69	22	5.61e+05	0.3168	22.95
NGC 2298	I	II	-1.96	0.99	-655	1394.0	0.78	36	7.20e+04	0.9739	23.36
NGC 4590	I	II	-2.27	0.9	-396	3160.0	0.48	30	3.06e+05	1.7380	44.67
NGC 5024	I	II	-2.06	0.99	-203	4614.0	0.40	62	7.33e+05	1.8220	95.64
NGC 5139	II	Int	-1.64	0.9	-1089	417.3	0.67	16	2.64e+06	3.5850	73.19
NGC 5272	I	I	-1.5	0.89	-649	1531.0	0.42	55	7.82e+05	1.0980	85.22
NGC 5466	I	II	-2.31	1.06	-83	2900.0	0.79	42	1.33e+05	6.6560	72.98
NGC 5904	I	I	-1.33	0.83	-289	1344.0	0.87	33	8.34e+05	0.9599	51.55
NGC 6093	I	II	-1.75	0.98	-1311	374.1	0.73	39	3.67e+05	0.4363	20.88
NGC 6121	I	I	-1.18	0.98	-1121	142.4	0.80	23	2.25e+05	0.7423	33.16
NGC 6171	I	I	-1.03	1.09	-1198	519.5	0.21	44	2.04e+05	1.0430	35.33
NGC 6205	I	II	-1.58	0.91	-476	2156.0	0.62	54	6.27e+05	1.2800	43.39
NGC 6341	I	II	-2.35	1.03	-880	337.8	0.76	23	3.64e+05	0.6277	30.05
NGC 6362	I	I	-1.07	1.06	-1090	655.6	0.39	22	1.17e+05	2.4980	30.73
NGC 6584	I	I	-1.5	0.88	-773	573.5	0.87	20	2.19e+05	1.0210	30.13
NGC 6656	II	II	-1.7	0.99	-871	1008.0	0.53	18	5.36e+05	1.2380	29.70
NGC 6779	I	II	-2	1.07	-791	392.9	0.86	15	1.89e+05	1.2030	28.86
NGC 6809	I	II	-1.93	0.96	-1038	763.1	0.51	56	2.41e+05	2.8270	24.07
NGC 6934	II	I	-1.56	0.87	-249	2905.0	0.72	55	2.15e+05	0.9983	33.83
NGC 7078	I	II	-2.33	1.01	-752	1631.0	0.32	36	9.84e+05	0.4235	82.58
NGC 7089	II	II	-1.66	0.92	-290	2384.0	0.68	53	8.81e+05	1.0700	41.65
NGC 7099	I	II	-2.33	1.01	-937	820.4	0.39	52	2.74e+05	0.1414	44.71

Table 3.3: For each principal component, we report the corresponding values in the second column, the resulting fraction of the total variance explained in the third column and, in the last column, the cumulative fraction of total variance explained.

	Eigenvalue	Fraction of total variance	Cumulative fraction of total variance
PC-1	2.9259	26.6%	26.6%
PC-2	2.1628	19.7%	46.3%
PC-3	1.7456	15.9%	62.2%
PC-4	1.4961	13.6%	75.8%
PC-5	0.8569	7.8%	83.6%
PC-6	0.6077	5.5%	89.1%
PC-7	0.5751	5.2%	94.3%
PC-8	0.2926	2.7%	97.0%
PC-9	0.2228	2.0%	99.0%
PC-10	0.0695	0.6%	99.6%
PC-11	0.0452	0.4%	100.0%

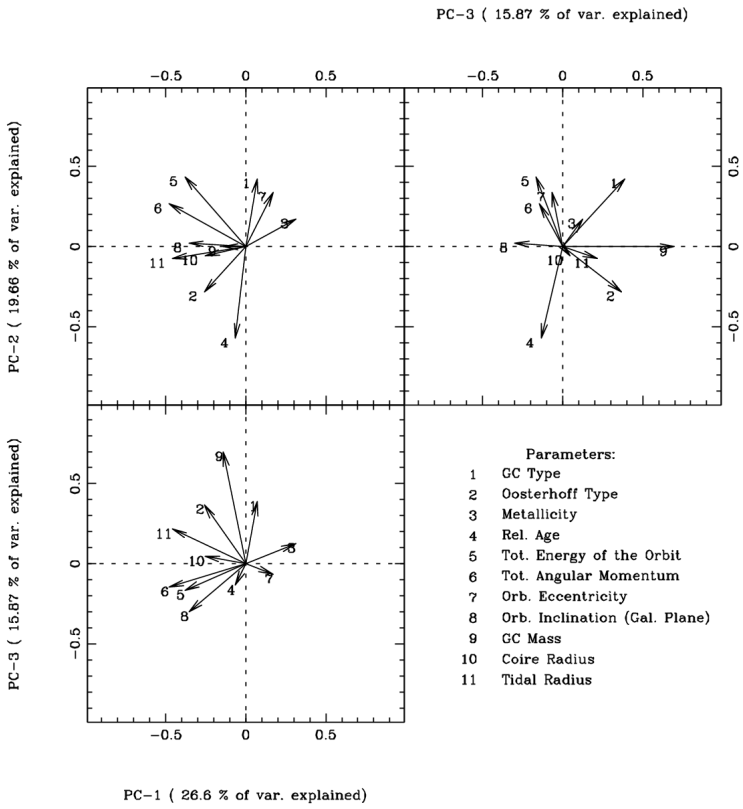

Figure 3.2: Eigenvectors projections of the 11 GC parameters on the planes defined by the first three principal components. Each axis legend reports also the total fraction of variance explained by each component. See text for details.

Table 3.4: Correlations between principal components (columns) and GC parameters (rows).

	PC-1	PC-2	PC-3	PC-4	PC-5	PC-6	PC-7	PC-8	PC-9	PC-10	PC-11
1	0.1245	0.6220	0.5135	-0.0457	0.2107	-0.3453	-0.3318	-0.2374	-0.0201	-0.0043	-0.0363
2	-0.4449	-0.4141	0.4864	-0.4532	0.2429	-0.2047	0.1070	0.2590	-0.0224	-0.0118	-0.0924
3	0.5345	0.2525	0.1676	0.5724	-0.4484	-0.1355	-0.0159	0.2112	-0.1594	-0.0299	-0.0649
4	-0.1096	-0.8404	-0.1773	-0.0407	-0.0223	-0.0021	-0.4107	-0.0635	-0.2742	0.0070	0.0140
5	-0.6520	0.6415	-0.2181	-0.0859	-0.0212	0.1615	-0.1608	0.1333	-0.0851	0.1741	-0.0253
6	-0.8186	0.3909	-0.1916	0.1375	0.0778	0.0078	-0.2370	0.1676	0.0197	-0.1679	0.0513
7	0.2936	0.5002	-0.0871	-0.7139	-0.0723	0.1662	0.1985	-0.0572	-0.2543	-0.0783	0.0001
8	-0.6095	0.0324	-0.3965	0.3218	0.1153	-0.4195	0.3728	-0.1132	-0.1580	0.0171	0.0169
9	-0.2402	-0.0021	0.9227	0.1809	-0.0084	0.1141	0.1197	0.0331	-0.1134	0.0348	0.1249
10	-0.4367	-0.0834	0.0597	-0.4676	-0.6990	-0.2732	-0.0461	-0.0479	0.1055	0.0128	0.0347
11	-0.7833	-0.1091	0.2859	0.2615	-0.1956	0.3327	0.0880	-0.2348	-0.0071	-0.0453	-0.1028

The resulting principal component values, along with the fraction of total variance explained by each component are listed in Table 3.3. The first four components explain respectively 27%, 20%, 16% and 14% of the total variance of the sample, for a total of 76%.

Table 3.4 lists the correlation coefficients between principal components and the 11 quantities considered in the analysis.

Figure 3.2 shows the eigenvector projections of the 11 quantities considered in the planes defined by the first and the second components (upper-left panel), the first and the third components (lower panel) and the third and the second components (upper-right panel).

The first component correlates mainly with orbital parameters like total energy, total angular momentum and inclination (5, 6 and 8 respectively); it also correlates with tidal radius (11), which points to a connection between this parameter and orbital ones. To a lesser extent it also correlates with Oosterhoff type (2) and metallicity (3), indicating the well known relation between metallicity and Oosterhoff type.

The second component shows correlations with cluster type (1), relative age (4), orbit total energy (5) and eccentricity (7). The strong alignment of the eigenvectors associated to cluster type and relative age in the upper-left panel of Figure 3.2, suggests that a detailed study of the origin of this behaviour should be pursued. We will discuss this topic in the following section.

The third component mainly correlates with GC mass (9). At a lesser extent it correlates also with cluster type, pointing to a correlation between both parameters.

The fourth component mainly correlates with the orbit eccentricity and with the metallicity. This relation was discussed in Dinescu et al. (1999). This component mildly correlate also with Oosterhoff type and core radius (2 and 10 respectively) both in the same sense as eccentricity.

Since the first component mainly correlates only with orbital parameters and tidal radius, the conclusion that can be reached is that it describes general properties of the whole GC sample. But our interest is to investigate how the new classification in type I and type II clusters affects the sample, so we have concentrated on the second and third components, which have the highest correlation with cluster type. The relations between it and other parameters are shown in the upper-right panel of Figure 3.2. It can be observed a possible relation between cluster type (1) and relative age (4), in fact, the two associated vectors points in opposite directions and are almost parallels.

3.3 Relations studied

The PCA analysis performed in the previous section has highlighted some possible correlations between various GC properties. In particular, we are interested in studying those that involves cluster type. For this reason, we reviewed in more detail some of them, this time without the use of PCA but quantifying the statistical significance of each one. Our choice is motivated also by the fact that for some quantities the sample used for the PCA is not complete. Therefore, in this way, we are able to detect the presence of selection biases in the precedent analysis.

For clarity, we report in Table 3.5 the Spearman rank coefficients (r_S) of the various correlations investigated. In the first column we report the coefficients for type I clusters, the coefficients for type II ones in the second one and, in the last column, we provide r_S for the sample of type II clusters excluding NGC 6388. In fact, this cluster is among the type II clusters that are not present in the sample used for the PCA in Section 3.2 and its metallicity and position in the Galaxy, makes it somewhat peculiar among this group of GCs (see also Paper IX). It is thus interesting for us to investigate also this last configuration in order to better compare the present results with those of the precedent analysis.

3.3.1 Age-metallicity relation

The strong anti-correlation found between cluster type and age deserves further investigation.

One of the main results coming from MF09 is that the old population of globular clusters shows a small age dispersion of about 0.05, with no detectable trends of age with metallicity. On the other hand, young clusters show a trend with metallicity, the younger clusters being more metal rich. This trend can be clearly seen in Figure 10 of MF09, that we have reproduced in Figure 3.3, highlighting type I and type II clusters present in their sample, respectively with black and red dots. Of the total 64 GCs considered in MF09, 46 are Type I while 10 are of Type II. Interestingly enough, all type II clusters except NGC 6388, show a clear age-metallicity relation.

MF09 noted that the age-metallicity trend of young clusters is followed by GCs believed to be associated with accreted dwarf galaxies, namely Sagittarius (Ibata et al. 1995; Dinescu et al. 2000; Bellazzini et al. 2003) and Monoceros (Crane et al. 2003; Frinchaboy et al. 2004). Also the stellar overdensity in Canis Major (Martin et al. 2004) is taken into account. The cluster sample of possible extra-galactic origin was composed by: Terzan 7, Terzan 8,Arp 2,

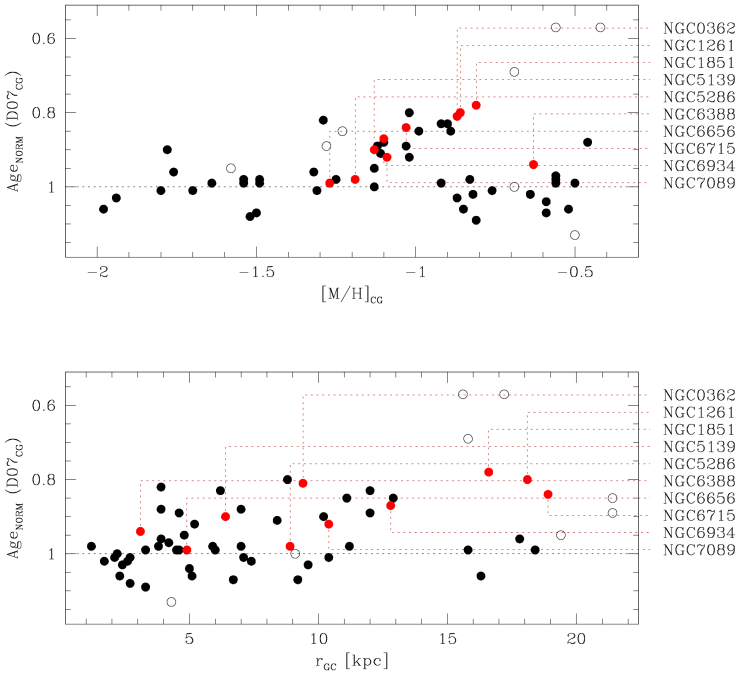

Figure 3.3: Age-metallicity relation for Galactic GCs from data of MF09. Distances from Galactic center come from Harris (1996, 2010 edition). Empty circles represent GCs for which type has not been determined in Paper IX, black dots type I clusters and red points type II ones.

Table 3.5: Spearman rank coefficients for different relations studied. For each case we give the coefficients for the type I clusters, for the whole type II cluster sample and, in the last column, for the sample of type II cluster excluding NGC 6388 from it.

Relation	Type I	Type II	halo Type II
Age vs. metallicity	0.05	-0.62	-0.95
Age vs. r_{GC}	-0.31	-0.76	-0.73
Age vs. $\mid X-8 \mid$	-0.30	-0.68	-0.68
Age vs. $\mid Y \mid$	-0.12	-0.54	-0.45
Age vs. $\mid Z \mid$	-0.16	-0.81	-0.77
[Fe/H] vs. r_{GC} for [Fe/H] ≤ -1	-0.40	0.70	0.70
[Fe/H] vs. $\mid X-8 \mid$ for [Fe/H] ≤ -1	-0.14	0.73	0.73
[Fe/H] vs. $\mid Y \mid$ for [Fe/H] ≤ -1	-0.37	0.37	0.37
[Fe/H] vs. $\mid Z \mid$ for [Fe/H] ≤ -1	-0.29	0.73	0.73

NGC 6715 (M54), Pal 12 and NGC 4147 for Sagittarius; NGC 2298, NGC 2808, NGC 5286, Pal 1 and BH 176 for Monoceros. NGC 2298 and NGC 2808 are also present in the list of GCs presumably associated to the Canis Major stellar overdensity along with NGC 1851 and NGC 1904. Three of them (NGC 6715, NGC 5286 and NGC 1851) are type II clusters, while NGC 2298 and NGC 2808 result to be type I clusters. Thus, not all GCs in the young group of MF09 are type II.

From Figure 3.3 it seems that NGC 6388 is the only type II cluster that does not follow the age-metallicity trend traced by the others. Nevertheless, it is worth noting that NGC 6388 is also the type II cluster which has the smallest distance to the Galactic center and also the one with the highest metallicity. In other words, it is the only type II cluster that can be ascribed strictly to the bulge population.

Apart from it, all the other type II clusters seem to follow a well defined trend. In particular, for the age-metallicity relation, the r_S calculated for all type II clusters is -0.62. The probability of randomly extracting ten points from the sample of Paper IX which display the same value of r_S or higher (i.e. $r_S \leq -0.62$), is less than 4.5%. If NGC 6388 is removed from the sample of type II clusters, $r_S = -0.95$.

On the other hand, the small r_S calculated for type I clusters (0.05) is consistent with GCs of the old population (as defined by MF09) being preferentially Type I clusters. In fact, with a mean relative age of 0.97 (median 0.99 and standard deviation of 0.08) they are slightly biased towards older ages than type II GCs wich results to have a mean relative age of 0.88 and standard deviation of 0.08. We thus ascribe to this the possible cause of the relation

between age and cluster type highlighted by the PCA.

Even more interesting is the lower panel of Figure 3.3, where relative age is plotted against Galactocentric distance (r_{GC}). MF09 noted an increase in age dispersion with distance for the young group of GCs. However, this trend is likely the consequence of the previously observed age-metallicity relation for these GCs. Focussing the attention on type II GCs (red dots), what Figure 3.3 shows is an age-r_{GC} relation for these clusters, rather than an increase in age spread. We have calculated r_S for both type I and II clusters in the plane defined by age and r_{GC} resulting in -0.31 for type I clusters and -0.76 for type II ones or -0.73 if NGC 6388 is removed from the sample (see Table 3.5). The probability of obtaining the same, or higher correlation ($r_S \leq -0.76$) randomly extracting ten points from the sample of type I and type II clusters of MF09 is less than 7%.

To further analyze the possible age-r_{GC} relation found for type II clusters we also considered each single cartesian Galactocentric coordinate (X, Y, Z) defined in the ususal way and measured in kiloparsec. We therefore studied the correlation between age and $\mid X - 8 \mid$, $\mid Y \mid$ and $\mid Z \mid$ respectively for each sample, in analogy to what has been done before. We report the results in Table 3.5. r_S for type II clusters results: -0.68 for X, -0.54 for Y and -0.81 for Z. It thus appears that the possible age-r_{GC} relation for type II clusters is more evident along the Z Galactic coordinate.

3.3.2 [Fe/H] vs Galactocentric distance

In this section we explore the distribution of values in the metallicity-r_{GC} plane.

In Figure 3.4 the Galactocentric distances from Harris 1996, 2010 edition against the [Fe/H] values from Carretta et al. (2009c) are plotted. The distribution of type I clusters seems consistent with the classical view of bulge and halo populations of MW GCs, with more metal rich GCs segregated in the central part of the Galaxy (Harris 2001; MF09).

From Figure 3.4 it can also be noted that NGC 6388 is the only type II cluster that can be considered strictly a bulge one. What is interesting is the relatively low scatter of all the other type II GCs respect to their mean metallicity if compared with the large dispersion of type I ones. In order to characterize this phenomenon, we have considered the sample of type I GCs with [Fe/H]< -1 (36 type I GCs satisfied this condition). We obtain $r_S = -0.40$ for them and $r_S = 0.70$ for type II GCs with [Fe/H]< -1.

The probability of obtainig a sample that displays an equal or higher $\mid r_S \mid$, randomly extracting nine points from the combined samples of type I and type II GCs with [Fe/H]≤ -1, (45 GCs in total) is less than 1%.

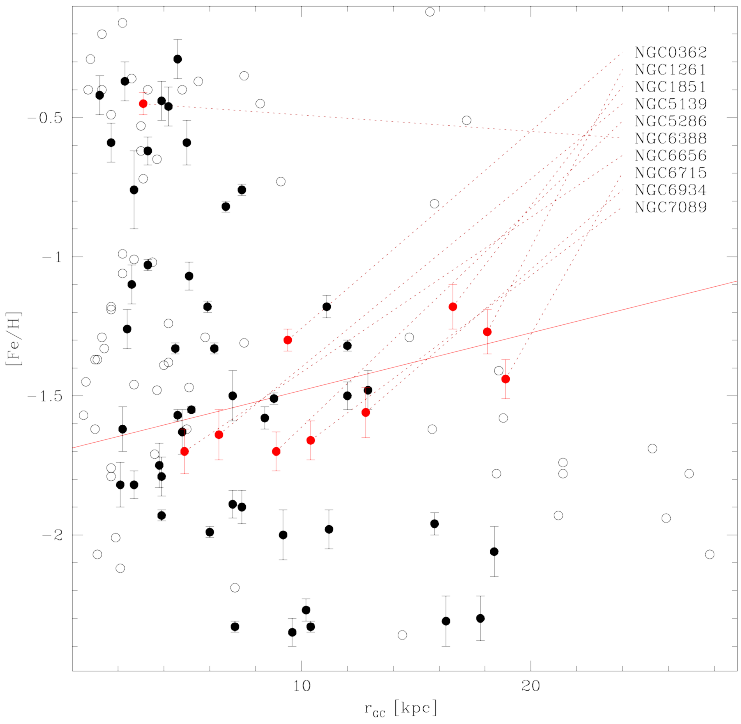

Figure 3.4:]
Galactocentric distances (from Harris 1996, 2010 edition) versus metallicities (from Carretta et al. 2009c). Empty dots represent non-surveyed clusters, black dots refer to type I GCs and red dots to type II. The red solid line is the resulting regression line for type II clusters with [Fe/H] ≤ -1,excluding NGC 6388.

Table 3.6: Oosterhoff type for type II clusters. Galactocentric distances have been also reported. References legend is: 1, Catelan (2009); 2, Zorotovic et al. (2010); 3, Sollima et al. (2010); 4, van den Bergh (2011); 5, Kunder et al. (2013); 6. Sollima et al. (2014).

	R_{GC} (kpc)	OoT	Ref.
NGC 6388	3.1	III	1; 6
NGC 6656	4.9	II	1; 4; 5
NGC 5139	6.4	II	1; 4
NGC 5286	8.9	II	1; 2
NGC 362	9.4	I	1; 4
NGC 7089	10.4	II	1; 4
NGC 6934	12.8	I	1; 4
NGC 1851	16.6	I	1; 4
NGC 1261	18.1	I	1; 4
NGC 6715	18.9	Int	1; 3

Such level of correlation might indicate the existence of a trend for the majority of type II GCs, with metal-richer ones located, nowadays, at larger r_{GC} than those with lower [Fe/H] values. Specifically, the slope of the regression line (solid red line in Figure 3.4) results 0.021 ± 0.005. In order to explore in more detail this possibility, we have investigated the spatial distribution of the Oosterhoff type of these clusters. We recall that this quantity, in fact, correlates with the metallicity of GCs. In Table 3.6 we have listed the Oosterhoff type along with Galactocentric distance for type II clusters. The resulting distribution seems to support the presence of such trend.

As previously done also for the age-r_{GC} relation, we studied the possible relations existing between metallicity and each single Galactic cartesian coordinate. The r_S calculated in each case are reported in Table 3.5. Type II GCs with [Fe/H]≤ -1 show higher values of correlation ($r_S = 0.73$) in the X and Z coordinates than in Y (rs = 0.37).

3.3.3 Orbital parameters vs. cluster type

The second principal component correlates with cluster type, orbit total energy, eccentricity and age (upper-left panel of Figure 3.2).

Figure 3.5 shows the orbit inclination distributions (left panel) and the orbital eccentricity cumulative distribution (right panel). Data are from Dinescu et al. (1999)). Type II clusters (in red) preferentially show high eccentricity orbits. This selection effect is particularly interesting, also in the light of the evidences provided in 3.2. The PCA, in fact, indicates a possible correlation

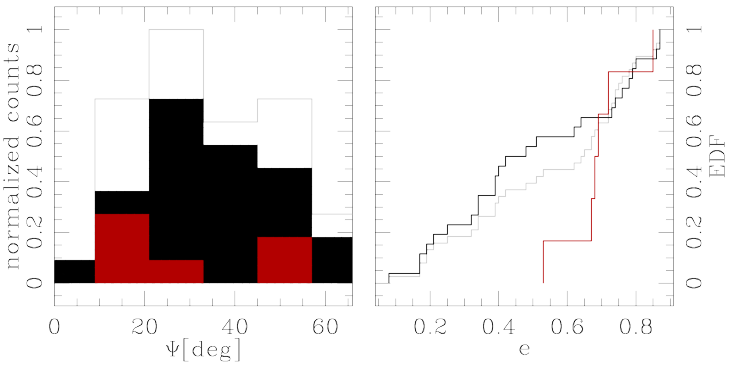

Figure 3.5: Left panel: Orbit inclinations distribution. Orbit inclinations are measured with respect to the Galactic plane. The red histogram refers to type II GC; the black one to type I clusters; the gray line shows the distribution of the total sample. Right panel:Orbit eccentricity cumulative distribution. The same color-code has been adopted. The used values are from Dinescu et al. (1999).

between cluster type and orbit eccentricity also in the sense of type II clusters having on average higher orbit eccentricity than type I ones.

Such differentiation is not detected for orbit inclinations, as the PCA already suggested. In this respect it is also relevant to remind the result obtained in Casetti-Dinescu et al. (2013). In that work the authors observe that NGC 6715 (M54), NGC 5139 (ωCen) and NGC 1851 have unrelated orbits. A tentative dynamical link could only be made for NGC 1851 and NGC 6656 (M22).

3.3.4 Cluster mass vs. cluster type

PCA indicates that 18.3% of variability in the considered sample is explained by the third principal component. This component mainly correlates with cluster mass (see lower-left panel of Figure 3.2).

This is consistent with Figure 3.6 that shows that type II clusters (in red) have, on average, higher mass than type I clusters.

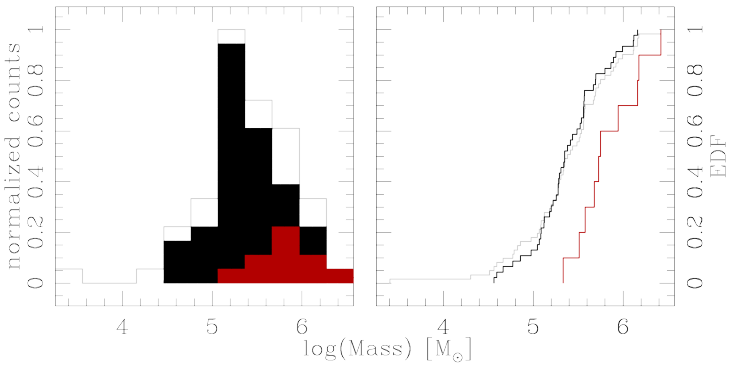

Figure 3.6: Left panel: Mass distribution. The red histogram refers to type II GCs; the black one to type I clusters; the gray line shows the distribution of the total sample. Right panel: Mass cumulative distribution. The same color-code has been adopted. Masses are from Gnedin & Ostriker (1997).

3.3.5 Spatial distribution of cluster types

In Section 3.3.1 and Section 3.3.2 we have noted that a possible relation involving age or metallicity and the spatial distribution of type II GCs may exist. In particular, the r_S values indicate that both relations are somewhat stronger if the Z cartesian Galactic coordinate is considered.

In Figure 3.7, the spatial distributions along the three Galactic coordinates X, Y and Z are shown. The black histograms show type I GCs while the red ones show type II ones. It can be noted that, in X and Y, the two samples seem to be distributed in the whole range of values. In the Z coordinate, instead, type II GCs seem to be preferentially located at negative values, in contrast with the apparent symmetry of the type I distribution. Specifically, no type II GCs are found above Z$\sim$ 2. Calculating the median of each sample and the associated dispersion, we have measured the separation between the two distributions in each projection. It results that, in units of dispersion, the two medians are separated by 0.08 in the X coordinate, 0.43 in Y and 0.80 in Z. We thus calculated the probability of obtaining such values of separation between medians, randomly extracting 10 points from the joint sample of type I and type II GCs. The resulting probabilities are $>$ 80% for X, $\sim$ 10% for Y and $<$ 0.5% for Z, which points to a likely bias in the Z values of the type II sample.

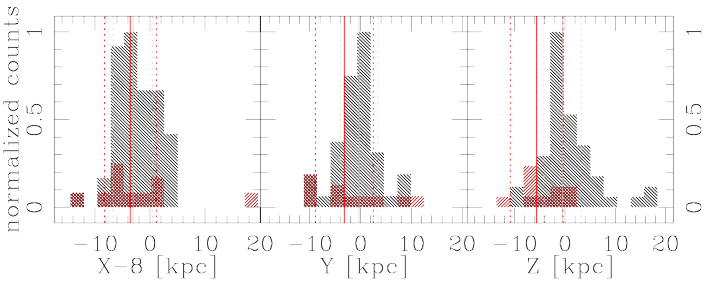

Figure 3.7: Spatial distribution of type I (black) and type II (red) GCs in Galactic cartesian coordinates. For each projection we have also indicated the position of the mean of each sample and the associated 68.27 percentile deviations. Grey vertical lines refers to type I GCs, while the red ones to type II GCs.

3.4 Summary (Conclusion)

With the advent of chromosome maps (Milone et al. 2015b, Paper IX), it has been shown that virtually all Galactic GCs host multiple stellar populations. It is also possible to detect a family of Galactic GCs that shows an above-the-mean complexity in their chromosome maps. These clusters can be distinguished from the others and have been classified as type II clusters, the remaining ones being labelled as type I clusters (Paper IX).

In this paper we study if and how cluster type correlates with GC properties. We have performed principal component analysis based on 11 quantities: cluster type, Oosterhoff type, metallicity, relative age, orbit total energy, orbit total angular momentum, orbit eccentricity, orbit inclination with respect to the Glactic plane, cluster masses, core radii and tidal radii. The main sources of variance in the considered sample results to be contained in orbital parameters and, in sligthly less extent, in the relation between cluster type and relative age. Here below we summarize the main results.

- In the plane age-metallicity, type II clusters define a clear trend, with more metal-rich clusters being younger. NGC 6388 is an exception, but it is also the only type II cluster that is located in the bulge.
- There are hints of a possible relation between age and Galactocentric distance for type II GCs, with younger clusters being located outwards.
- In the [Fe/H]-r_{GC} plane, halo type II clusters seem to show a trend, with

more metal-rich clusters being located outwards. This trend is consistent with the radial distribution of their Oosterhoff type and apparently inconsistent with the trend found for type I GCs.

– The orbits of type II clusters seem to be more eccentric than the average of type I clusters. A large dispersion of the orbital inclinations with respect to the Galactic plane is also observed and is similar for both groups.

– Type II clusters are, on average, more massive than type I ones. There are, in any case, type I clusters with mass comparable to those of type II.

– The spatial distribution of type II GCs have highlighted that these clusters are, nowadays, preferentially located below the plane of the Galaxy. Specifically, no type II GC has been observed above Z$\sim$ 2.

This suggest two kind of studies that should be carried on: (i) it will be of primary interest to search for additional type II clusters, especially at Z$>$ 0 kpc; (ii) it should be also advisable to perform detailed simulation of the kinematic of type II GCs.

For the first point, we are suggesting to trace the path to a photometric survey aimed to enlarge the sample of Galactic GCs for which chromosome maps could be used to discern their type. Extending the survey to the full sample of the MW will improve the statistical significance of the present results.

For the second point we find of particular interest to establish, in the light of this new classification, if some remnants of a common dynamical pattern could be detected among the known type II clusters.

3.5 Appendix

Following the suggestion made by one of the referees of this thesis, in this section we present the results coming from a PCA perfomed on the same sample as in Section 3.2 but including, with all the 11 quantities already considered, the horizontal branch (HB) morphology. The new list of parameters is presented in Table 3.7.

The result of the PCA is reported in Figure 3.8 where the projections of the eigenvectors of the 12 quantites on the planes defined by the first three principal components are shown. While the PCA is showing again a possible correlation between cluster type (1) and relative age (4), it does not reveal any strong link between the first quantity and HB index (9).

Table 3.7: GC properties considered for the second PCA. They will be identified in the following with the identification number provided in the first column. The HB index values used are those tabulated in Mackey & van den Bergh (2005)

	Description
1	Cluster type
2	Oosterhoff type
3	Metallicity
4	Relative age
5	Total energy of the orbit
6	Total angular momentum
7	Orbit eccentricity
8	Orbit inclination with respect to the Gal. plane
9	HB index
10	Cluster mass
11	Core radius (parsec)
12	Tidal radius (parsec)

Table 3.8: For each principal component, we report the corresponding values in the second column, the resulting fraction of the total variance explained in the third column and, in the last column, the cumulative fraction of total variance explained.

	Eigenvalue	Fraction of total variance	Cumulative fraction of total variance
PC-1	3.1811	26.5%	26.5%
PC-2	2.2224	18.5%	45.0%
PC-3	1.8908	15.8%	60.8%
PC-4	1.7426	14.5%	75.3%
PC-5	0.9614	8.0%	83.3%
PC-6	0.6500	5.4%	88.7%
PC-7	0.6020	5.0%	93.7%
PC-8	0.2907	2.4%	96.1%
PC-9	0.2460	2.1%	98.2%
PC-10	0.0998	0.8%	99.0%
PC-11	0.0709	0.6%	99.6%
PC-12	0.0424	0.4%	100.0%

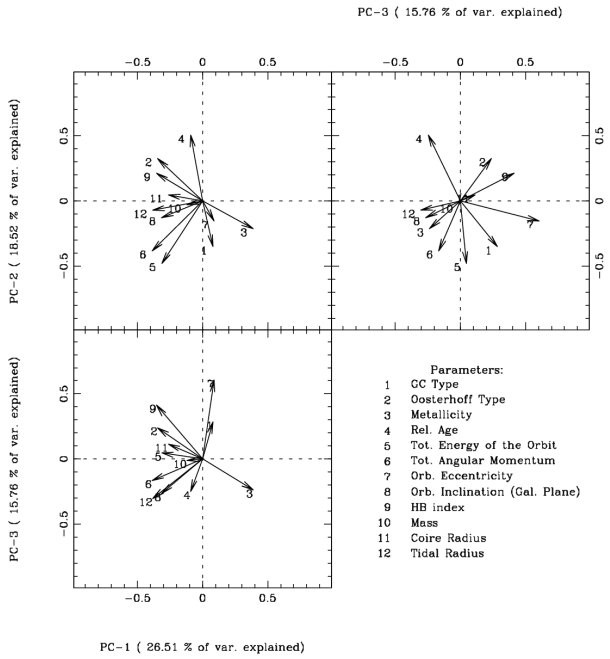

Figure 3.8: Eigenvectors projections of the 12 GC parameters on the planes defined by the first three principal components. Each axis legend reports also the total fraction of variance explained by each component.

Table 3.9: Correlations between principal components (columns) and GC parameters (rows).

	PC-1	PC-2	PC-3	PC-4	PC-5	PC-6	PC-7	PC-8	PC-9	PC-10	PC-11	PC-12
1	0.1426	-0.5236	0.3923	-0.4700	0.1714	0.0882	0.4836	-0.2406	-0.0210	-0.0105	0.0012	-0.0350
2	-0.6162	0.4839	0.3294	-0.3974	0.0903	-0.0438	0.1300	0.2689	0.0532	0.0800	-0.0064	-0.1055
3	0.6909	-0.3182	-0.3269	-0.2656	-0.1798	-0.3171	0.0664	0.1919	-0.2428	-0.0883	-0.0246	-0.0499
4	-0.1638	0.7544	-0.3412	0.1512	-0.1359	0.2881	0.2574	-0.0748	-0.2992	0.0419	0.0085	0.0098
5	-0.5604	-0.7157	0.0623	0.2204	-0.1061	0.2218	-0.0312	0.1322	-0.1040	-0.0084	0.1767	-0.0166
6	-0.6937	-0.5705	-0.2277	0.1462	0.0290	0.1921	0.1547	0.1614	-0.0110	-0.0114	-0.1735	0.0457
7	0.1587	-0.2285	0.8336	0.2474	-0.2050	-0.0116	-0.2441	-0.0575	-0.1986	0.1258	-0.0766	-0.0206
8	-0.5650	-0.1895	-0.3664	0.3274	0.3167	-0.5108	0.0909	-0.1093	-0.0735	0.1272	0.0212	-0.0014
9	-0.6356	0.3154	0.5668	0.0828	0.2685	-0.1800	-0.0439	-0.0189	-0.1355	-0.2049	-0.0011	0.0356
10	-0.2143	-0.0451	-0.0156	-0.9444	0.0328	-0.0309	-0.1649	0.0330	-0.0968	0.0796	0.0276	0.1144
11	-0.4682	0.0713	0.1577	-0.0035	-0.7856	-0.2668	0.2202	-0.0481	0.1002	-0.0160	0.0114	0.0359
12	-0.6842	-0.1065	-0.4171	-0.3650	-0.1683	0.0708	-0.3320	-0.2355	-0.0272	-0.0545	-0.0405	-0.0949

Table 3.10: Oosterhoff type and HB index for type II clusters. Galactocentric distances have been also reported.

	R_{GC} (kpc)	OoT	HB index
NGC 6388	3.1	III	-1.00
NGC 6656	4.9	II	0.91
NGC 5139	6.4	II	-
NGC 5286	8.9	II	0.80
NGC 362	9.4	I	-0.87
NGC 7089	10.4	II	0.92
NGC 6934	12.8	I	0.25
NGC 1851	16.6	I	-0.32
NGC 1261	18.1	I	-0.71
NGC 6715	18.9	Int	0.54

The resulting principal components eigenvalues are listed in table 3.8 along with the correspong percentage of variance explained by each of them. Even in this case, the first four principal components absorb about 75% of the total variance of the sample. From Table 3.9 it can be noted that the fourth principal component is the one that mainly correlates with the mass (10) while the third component is now mostly correlating with orbit eccentricity (7). The second principal component is more similar to what was obtained in the previous PCA. It correlates mostly with relative age (4) and total energy of the orbit (5). The correlation between this component and cluster type results lowered and instead, it shows mild correlation with total angular momentum (6). The first principal component is also similar to what was obtained in the previous PCA. But in this case, it is also correlating with HB index (9). In particular, the PCA is indicating some levels of correlations between HB index and metallicity (3) and Oosterhoff type (2). This can be also observed by looking the alignment between the corresponding arrows in Figure 3.8. This reflects the well-known relation between metallicity and HB morphology. We thus updated Table 3.6 with the correspondign HB index for each type II GC. We provide them in Table 3.10.

It can be noted that Oosterhoff type II GCs have higher values of HB index, as the PCA has already shown. No other evident trends of this quantity with Galactocentric distance have been detected.

It is worth mentioning that, by using UV and visual photometry obtained in the context of the HST UV Legacy Survey of Galactic GCs, Brown et al. (2016) characterized and compared the HB morphology of a sample of 53 Galactic GCs and classify them into 5 distinct categories. The PCA performed including this

last quantity produces analogous results with respect to the one presented.

4

ACS/WFC Parallel-Field Catalogues

The content of this chapter has been adapted from the work: The *Hubble Space Telescope* UV Legacy Survey of Galactic Globular Clusters. XIII. ACS/WFC Parallel-Field Catalogues. The article has been published in the peer-reviewed journal Monthly Notices of the Royal Astronomical Society (Simioni et al. 2018).

Abstract

As part of the *Hubble Space Telescope UV Legacy Survey of Galactic Globular Clusters*, 110 parallel fields were observed with the Wide Field Channel of the Advanced Camera for Surveys, in the outskirts of 48 globular clusters, plus the open cluster NGC 6791. Totalling about 0.3 square degrees of observed sky, this is the largest homogeneous *Hubble Space Telescope* photometric survey of Galalctic globular clusters outskirts to date. In particular, two distinct pointings have been obtained for each target on average, all centred at about 6.5 arcmin from the cluster centre, thus covering a mean area of about 23 arcmin^2 for each globular cluster. For each field, at least one exposure in both F475W and F814W filters was collected. In this work, we publicly release the astrometric and photometric catalogues and the astrometrised atlases for each of these fields.

4.1 Introduction

For almost three decades, the Milky Way Globular Clusters (GCs) have been the target of large CCD photometric surveys aimed at sampling their stellar populations in a homogeneous way (Rosenberg et al. 2000a, Rosenberg et al.

2000b, Piotto et al. 2002, Sarajedini et al. 2007) using both space- and ground-based instruments. The growing sample of data, and the advent of increasingly sophisticated data-analysis techniques, have clearly demonstrated that GCs host distinct stellar populations with different chemical abundances. High-precision photometric measurements have revealed that the colour-magnitude diagrams (CMDs) show distinct sequences in various evolutionary stages (see e.g. Anderson 1997, Lee et al. 1999, Pancino et al. 2000, Bedin et al. 2004, Piotto et al. 2007, Milone et al. 2008, Bellini et al. 2010). These findings are also supported by spectroscopical evidence that the stellar populations of these systems are not as simple as thought (see e.g. Marino et al. 2008, Yong & Grundahl 2008, Kraft 1994, Carretta et al. 2009a, Carretta et al. 2009b, Gratton et al. 2004, Gratton et al. 2012).

The *Hubble Space Telescope UV Legacy Survey of Galactic Globular Clusters* (GO-13297; PI:Piotto) has been specifically designed to further investigate this phenomenon and it now appears likely that all Galactic GCs host multiple stellar populations (Piotto et al. 2015 – hereafter Paper I, Milone et al. 2017 – hereafter Paper IX). In the context of this survey, parallel Advanced Camera for Surveys (ACS) observations have been obtained. While the main observations were taken using a combination of UV and optical filters of the Wide Field Camera 3 (WFC3), the lack of filters bluer than F435W dictated the use of the F475W and F814W filters of the Wide Field Channel of the ACS (ACS/WFC) in the parallel observations. The large colour baseline provided by this filter combination guarantees sensitivity to helium abundance differences, while being largely insensitive to star-to-star variations in light-element abundances (Sbordone et al. 2011, Cassisi et al. 2017).

One of the main objectives for which these observations were planned is to investigate how different stellar populations formed in GCs. Strong observational constraints come from the analysis of the radial distribution of each stellar population (D'Ercole et al. 2008; Bellini et al. 2009, Vesperini et al. 2013). As an example, Simioni et al. (2016) complemented WFC3 data of the central regions of NGC 2808 with ACS parallel observations and found evidence of different radial trends associated with distinct stellar populations hosted by the cluster. Thus, clusters with large helium variations among their stellar populations are the preferred target of investigation with the current data-sample. Other interesting targets, albeit extensively studied, are those defined as Type-II clusters in Paper IX, which displays multiple sub-giant branches in optical CMDs.

We stress the fact that this is the first homogeneous *HST* photometric survey of the outskirts of Galactic GCs. The observations presented here represent a first epoch for future studies aimed at systematical measurements of absolute,

relative and internal proper motions of stars in these regions. Archival *HST* observations matching a sub-sample of the observed fields exist, and proper motions will be published separately. In the imaged stellar fields, the stellar density is not as high as in the central regions. As a consequence, crowding is not a serious issue for these data. That makes them particularly suitable to be used as input catalogue for future spectroscopic surveys.

The present catalogues can be used to perform several interesting analyses. For example, dynamical interactions between stars in GCs is at the origin of the mass segregation phenomenon. A precise estimate of its effects is fundamental for the derivation of a global mass function for a GC (Vesperini & Heggie 1997, Paust et al. 2010, Sollima & Baumgardt 2017). The measurement of the fraction of binaries is also fundamental for this kind of analysis and could provide useful constraints for dynamical models (Milone et al. 2012c). We note, also, that in some cases white dwarf cooling sequences are visible in the obtained CMDs. Finally, it is interesting to note that due to the presence of many extra-galactic objects in the observed field, other studies could benefit from these observations.

In this work, we present the first photometric catalogues from the ACS/WFC parallel observations of the GO-13297 program. All data have been reduced in a homogeneous manner, making these catalogues particularly suitable for inter-comparison. The article is organised as follows: in Section 4.2 the data are presented along with some information about the observing strategy, together with a detailed description of the data reduction. The extracted CMDs are presented in Section 4.3. Details on the selection of well measured stars are given in Section 4.4. In Section 4.5 the catalogues and the released electronic material are described in detail. Finally, in Section 4.6, after a summary, we briefly discuss some of the main scientific questions we will address with these catalogues in subsequent papers.

4.2 Observations and Data Reduction

Table 4.1: Observation log. For each GC in the survey, and the open cluster NGC 6791, we show right ascension and declination of each distinct parallel field, referred to the centre of ACS/WFC. We also report the number of orbits, Telescope orientation (V3 PA) for each orbit and exposure time in each filter.

#	CLUSTER	ORBITS	FIELD [PA (deg)]	RA (J2000) ($^{h}\,^{m}\,^{s}$)	DEC (J2000) ($^{\circ}\,'\,''$)	EPOCH	EXP. TIME F475W (s)	EXP. TIME F814W (s)
01	NGC1261	5	F1 [92]	03:12:49.68	-55:17:25.2	31/08/13	770	694
			F2 [138]	03:12:16.96	-55:19:29.6	11/09/13	745	669
			F3 [182]	03:11:44.35	-55:17:39.3	08/11/13	766	690
			F4 [225]	03:11:30.53	-55:13:17.9	07/12/13	745	669
			F5 [48]	03:13:01.92	-55:12:51.4	29/06/14	829	753
02	NGC1851	7	F1 [195]	05:13:37.57	-40:06:44.0	27/12/10	2x40;2x1277;1237	6x488;1x40
			F2 [164]	05:13:51.57	-40:08:55.8	11/11/10	2x40;2x1277;2x1237	8x488;2x40
03	NGC2298	4	F1 [185]	06:48:36.04	-36:05:08.7	18/12/13	2x785	2x683
			F2 [273]	06:48:35.14	-35:55:40.7	07/03/14	885	816
						15/03/15	887	815
04	NGC3201	2	F1 [25]	10:18:12.19	-46:21:47.1	13/09/13	685	612
			F2 [115]	10:17:54.00	-46:30:51.0	01/01/14	689	616
05	NGC4590	2	F1 [112]	12:39:42.64	-26:50:34.9	21/12/13	627	554
			F2 [202]	12:39:01.10	-26:47:48.5	30/03/14	627	554
06	NGC4833	4	F1 [113]	13:00:10.12	-70:58:29.4	17/01/14	2x840	2x771
			F2 [202]	12:58:20.68	-70:55:42.6	09/04/14	2x806	2x730
07	NGC5024	6	F1 [31]	13:13:21.59	+18:12:01.1	24/03/14	4x725;2x723	3x370
			F2 [120]	13:13:03.82	18:03:52.0	08/12/13	4x775;2x774	3x375
08	NGC5053	5	F1 [352]	13:16:42.03	+17:47:28.7	01/04/14	740	664
			F2 [37]	13:16:53.97	+17:43:15.0	16/03/14	740	664
			F3 [80]	13:16:50.28	+17:38:33.1	23/01/14	790	714
			F4 [125]	13:16:33.21	+17:35:39.5	05/12/13	790	714
			F5 [308]	13:16:21.88	+17:48:25.0	16/05/14	765	689
09	NGC5286	2	F1 [73]	13:47:07.09	-51:25:00.2	14/12/13	728	655
			F2 [162]	13:46:11.09	-51:28:46.7	15/03/14	603	559

Continued on Tab. 4.2

Table 4.2: Table 4.1 (continued)

#	CLUSTER	ORBITS	FIELD [PA (deg)]	RA (J2000) ($^{h\ m\ s}$)	DEC (J2000) ($^{\circ}\ '\ ''$)	EPOCH	EXP. TIME F475W (s)	EXP. TIME F814W (s)
10	NGC5466	4	F1 [112]	14:05:41.08	+28:26:12.1	05/01/14	834;835	763;765
			F2 [21]	14:05:54.29	+28:35:18.1	29/03/14	2x776	2x700
11	NGC5897	4	F1 [112]	15:17:37.48	-21:06:27.5	12/02/14	830;833	2x761
			F2 [202]	15:16:58.75	-21:03:44.3	13/05/14	779;781	710;709
12	NGC5904	2	F1 [323]	15:18:34.23	02:11:38.3	17/05/14	620	559
			F2 [52]	15:19:00.34	02:04:36.4	08/04/14	621	559
13	NGC5927	3	F1 [100]	15:28:28.73	-50:45:30.4	01/02/14	603	559
			F2 [189]	15:27:28.26	-50:44:48.7	19/05/14	603	559
						27/05/15	603	559
14	NGC5986	3	F1 [92]	15:46:28.87	-37:51:38.6	27/01/14	676	603
			F2 [180]	15:45:40.83	-37:52:21.9	17/05/14	603	559
						10/05/15	603	559
15	NGC6093	5	F1 [255]	16:16:35.04	-22:55:45.9	09/06/12	5x760;5x845	5x539
16	NGC6101	5	F1 [147]	16:25:36.08	-72:18:35.2	04/04/14	762	686
			F2 [190]	16:24:40.57	-72:16:07.7	25/05/14	762	686
			F3 [235]	16:24:23.48	-72:11:18.6	29/06/14	800	724
			F4 [282]	16:24:58.26	-72:06:50.7	14/08/13	851	775
			F5 [101]	16:26:39.71	-72:17:19.9	28/02/14	800	724
17	NGC6121	2	F1 [272]	16:23:12.57	-26:27:02.1	06/07/14	739	666
			F2 [98]	16:23:55.64	-26:36:33.4	17/02/15	666	593
18	NGC6144	2	F1 [83]	16:27:39.42	-26:05:00.9	28/02/14	679	606
			F2 [174]	16:26:57.33	-26:07:05.2	27/05/14	679	606
19	NGC6171	4	F1 [342]	16:32:41.94	-12:56:56.1	31/05/14	830;833	2x761
			F2 [72]	16:32:42.20	-12:57:07.5	25/03/14	800;802	731;730
20	NGC6218	2	F1 [276]	16:46:55.21	-01:52:03.7	16/08/13	721	648
			F2 [6]	16:47:33.42	-01:52:07.7	27/05/14	645	572
21	NGC6254	2	F1 [276]	16:56:50.04	-04:01:10.1	16/08/13	721	648
			F2 [7]	16:57:28.66	-04:01:19.2	27/05/14	644	571

Continued on Tab. 4.3

Table 4.3: Table 4.1 (continued)

#	CLUSTER	ORBITS	FIELD [PA (deg)]	RA (J2000) ($^{h}\,^{m}\,^{s}$)	DEC (J2000) ($^{\circ}\,'\,''$)	EPOCH	EXP. TIME F475W (s)	EXP. TIME F814W (s)
22	NGC6304	2	F1 [184]	17:14:10.53	-29:32:35.1	07/06/14	624	559
			F2 [274]	17:14:09.53	-29:23:04.8	26/08/13	731	658
23	NGC6341	2	F1 [230]	17:16:30.21	+43:08:03.0	22/10/13	638	565
			F2 [319]	17:17:06.19	+43:14:56.0	03/08/14	750	677
24	NGC6352	2	F1 [161]	17:25:15.00	-48:31:41.7	27/05/14	637	564
			F2 [251]	17:24:51.02	-48:22:52.5	13/08/13	731	658
25	NGC6362	2	F1 [125]	17:32:14.07	-67:09:25.3	30/03/14	651	578
			F2 [215]	17:30:47.67	-67:04:37.3	01/07/14	760	687
26	NGC6366	2	F1 [293]	17:27:31.94	-04:58:44.4	26/08/13	726	653
			F2 [351]	17:27:58.09	-04:58:57.1	07/06/15	644	571
27	NGC6388	4	F1 [238]	17:35:40.80	-44:43:02.9	05/07/14	865;906	796;834
			F2 [141]	17:36:17.23	-44:50:53.5	12/05/14	793;795	724;723
28	NGC6397	2	F1 [90]	17:41:17.47	-53:44:46.1	27/03/14	683	610
			F2 [180]	17:40:12.50	-53:45:38.3	11/06/14	640	567
29	NGC6441	4	F1 [102]	17:50:34.23	-37:08:21.5	26/03/14	833;835	764;763
			F2 [192]	17:49:46.24	-37:07:12.6	15/06/14	2x794	725;722
30	NGC6496	2	F1 [157]	17:58:53.12	-44:22:28.2	30/05/14	638	656
			F2 [247]	17:58:27.50	-44:13:57.0	12/08/13	731	658
31	NGC6535	2	F1 [319]	18:03:49.95	+00:11:04.6	19/07/14	724	651
			F2 [50]	18:04:17.63	+00:17:50.2	26/05/14	644	571
32	NGC6541	2	F1 [80]	18:08:35.16	-43:46:11.5	14/02/14	689	616
			F2 [170]	18:07:44.04	-43:48:48.8	11/06/14	639	566
33	NGC6584	2	F1 [155]	18:18:26.74	-52:19:31.3	30/05/14	640	567
			F2 [245]	18:17:54.89	-52:11:09.9	18/08/13	726	653
34	NGC6624	2	F1 [264]	18:23:14.50	-30:17:51.1	03/09/13	731	658
			F2 [174]	18:23:23.29	-30:27:20.2	27/06/14	638	565
35	NGC6637	4	F1 [84]	18:31:49.55	-32:24:40.9	18/02/14	827;840	758;768
			F2 [174]	18:31:05.49	-32:26:31.5	30/06/14	792;794	723;722

Continued on Tab. 4.4

Table 4.4: Table 4.1 (continued)

#	CLUSTER	ORBITS	FIELD [PA (deg)]	RA (J2000) ($^{h}\,^{m}\,^{s}$)	DEC (J2000) ($^{\circ}\,'\,''$)	EPOCH	EXP. TIME F475W (s)	EXP. TIME F814W (s)
36	NGC6652	3	F1 [281]	18:35:25.09	-32:54:08.8	30/08/13	707	633
			F2 [238]	18:35:14.87	-32:58:25.1	14/08/13	733	658
			F3 [192]	18:35:20.06	-33:03:36.1	01/07/14	621	548
37	NGC6656	4	F1 [266]	18:36:00.25	-23:50:16.5	23/09/10	656;644	2x389
			F2 [85]	18:36:47.76	-23:58:08.0	17/03/11	2x656	2x389
38	NGC6681	2	F1 [271]	18:42:48.78	-32:13:03.7	05/09/13	730	658
			F2 [183]	18:42:51.19	-32:22:33.1	29/06/14	637	564
39	NGC6715	6	F1 [153]	18:54:56.04	-30:35:08.9	29/06/14	2x736;2x737;2x734	3x370
			F2 [243]	18:54:33.96	-30:27:06.5	05/09/13	4x819;2x817	3x390
40	NGC6717	3	F1 [80]	18:55:31.98	-22:45:22.7	06/05/14	619	535
			F2 [125]	18:55:12.41	-22:48:27.0	03/07/14	619	544
			F3 [171]	18:54:51.25	-22:47:57.0	03/07/14	617	544
41	NGC6723	3	F1 [103]	18:59:54.19	-36:43:18.0	03/04/14	666	592
			F2 [148]	18:59:27.49	-36:44:21.9	15/06/14	626	551
			F3 [193]	18:59:06.07	-36:41:59.9	05/07/14	624	551
42	NGC6779	2	F1 [241]	19:16:04.77	+30:12:18.9	13/10/13	731	658
			F2 [333]	19:16:42.17	+30:17:38.2	19/07/14	637	564
43	NGC6791	2	F1 [322]	19:20:53.69	+37:53:04.8	17/08/13	631	559
			F2 [50]	19:21:27.31	+37:46:16.6	26/04/14	638	565
44	NGC6809	2	F1 [262]	19:39:32.79	-30:54:19.4	21/08/14	753	680
			F2 [82]	19:40:26.65	-31:01:26.4	29/03/14	677	604
45	NGC6838	2	F1 [244]	19:53:18.63	+18:48:20.3	23/10/13	723	650
			F2 [75]	19:54:12.48	+18:43:53.9	03/05/14	681	608
46	NGC6934	2	F1 [245]	20:33:44.84	+07:25:55.5	08/10/13	723	650
			F2 [334]	20:34:17.59	+07:30:52.3	18/08/14	644	571
47	NGC6981	2	F1 [289]	20:53:13.45	-12:26:24.9	13/08/13	641	568
			F2 [19]	20:53:51.29	-12:28:39.5	03/08/14	624	551
48	NGC7089	3	F1 [237]	21:32:59.85	+00:48:42.0	18/10/13	717	643
			F2 [281]	21:33:10.93	+00:44:15.0	29/08/13	668	593
			F3 [327]	21:33:29.92	+00:42:39.1	14/08/13	611	534
49	NGC7099	2	F1 [92]	21:40:44.34	-23:15:15.1	08/06/14	656	583
			F2 [182]	21:40:02.30	-23:15:49.0	19/08/14	656	583

Tables 4.1, 4.2, 4.3 and 4.4 report the log of ACS/WFC observations used to construct the catalogues. For each target, we indicate the total number of orbits assigned to each observed field separated by the different position angles (PAs) of the V3 axis of the *HST* focal plane. Typically, one F475W and one F814W image were taken each orbit, with a dither between the two dictated by primary WFC3 observing strategy. For each field, right ascension and declination of the centre of ACS/WFC are provided along with exposure time in each filter.

The physical position of ACS/WFC detectors in the focal plane of *HST* is such that its projected field of view (FoV) in the sky is located at a distance of about 6.5 arcminutes from the centre of the WFC3 FoV. Depending on the number of orbits allocated to each GC, from 2 to a maximum of 5 non-overlapping fields were observed. This is because, in order to secure a good handling of charge-transfer-efficiency (CTE) systematic errors, primary WFC3 observations were taken by applying a different telescope rotation at each orbit (Paper I, Section 4). For the majority of clusters, which were allocated 2 orbits, a rotation of about 90° was performed between the first and second orbit; for clusters observed for more than 2 orbits, a minimum difference of $\sim 45°$ between the V3 PA of each orbit was required. Five distinct pointings were obtained for 3 clusters, namely NGC 1261, NGC 5053 and NGC 6101. Three distinct fields were obtained for 4 clusters: NGC 6652, NGC 6717, NGC 6723 and NGC 7089. For the other clusters, only 2 pointings were planned. M80 is an exception and was not observed as part of the Program GO-13297. For it, we make use of archival *HST* data from GO-12311. When possible, ACS parallel observations targeted pre-existing *HST* observations.

Figures 4.1 and 4.8 – 4.15 display all *HST* observations that sample the sky area in the vicinity of those covered in this survey. Three cameras onboard *HST* were considered in order to enhance the probability of an overlap between observations: Wide Field and Planetary Camera 2 (WFPC2), ACS and WFC3 (both UVIS and IR channels). Taking 2 images per orbit, one in F475W and one in F814W filters, the typical exposure times for both filters are of the order of 700s.

All exposures have been corrected for CTE effects using the method described in Anderson & Bedin (2010). Photometric measurements of stellar objects in each field have been performed using a suite of FORTRAN programs based on `img2xym` (Anderson & King 2006) and `kitchen_sync` presented in Anderson et al. (2008a). The spatial variation of the PSF has been taken into account adopting a grid of 9×10 model PSFs distributed along each image. However focus changes/breathing of the telescope, imperfect guiding, residual noise related to CTE can produce image-to-image variations of the PSF. To

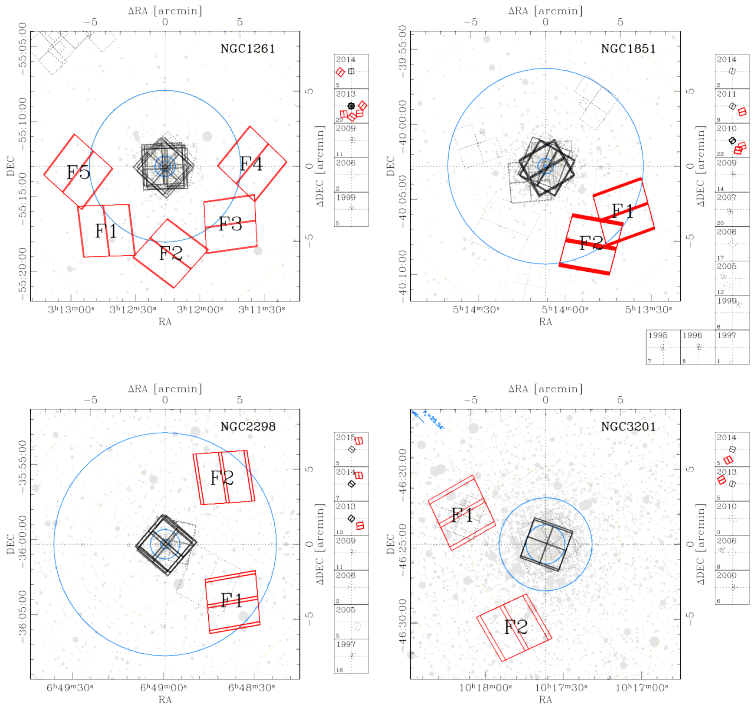

Figure 4.1: Finding charts for NGC 1261, NGC 1851, NGC 2298 and NGC 3201. Red outlines, represent ACS/WFC parallel observations of GO-13297, black outlines refer to WFC3/UVIS observations. Dark gray, dashed outlines represent archive *HST* observations in the same regions. Footprints are labeled as in Table 4.1. Observations are subdivided by epoch in the smaller panels. Blue circles mark the position of core radius, half-light radius and tidal radius for each cluster from Harris (1996, 2010 edition). Where the tidal radius could not be included in the image, its value has been indicated in the upper-let corner of the image. Yellow, dashed circles mark the distances of 1, 5 and 10 arcminutes from cluster centres. Gray dots corresponds to 2MASS sources, with brighter sources being larger.

mitigate these sources of systematic errors, we derived a set of spatially varying perturbations of the PSF models for each calibrated, non-drizzled (`flc`) image. Adopting the procedure presented in Bellini et al. (2013b), each image is divided into a grid with a number of cells changing from 2×2 to 5×5. In each cell, a subset of well measured stars is used to locally adjust the PSF models to the stellar profiles. Using an updated version of Anderson & King (2006) software, in combination with the newly created PSF models, we extracted raw catalogues of stellar positions and magnitudes in each image. We choose the grid refinement (between 2×2 to 5×5) that produces the best results, inspecting the distribution of the quality of fit parameters as a function of magnitude, and taking into account the number of reference stars used to tailor the PSF perturbations in each cell.

Each exposure related to the same field has been subsequently referred to a common reference frame. Since we are mainly interested in the faint, red part of the cluster CMDs, we used the F814W images to construct the reference frames. Catalogues are finally produced using a version of the software presented in Anderson et al. (2008a), specifically tuned for this project. In particular, the `kitchen_sync` routine has been modified in order to work properly with only one image per filter. In addition, the method presented in Gilliland (2004) was applied in order to provide reliable photometry also for saturated stars.

The raw, instrumental magnitudes have been zero-pointed into ACS/WFC Vega-mag photometric system following the prescriptions of Bedin et al. (2005). The zero-points and aperture corrections from 0.5 arcseconds to infinity of Bohlin (2016) have been used.

Especially in the present case, the photometric calibration plays a critical role, and we put strong efforts to precisely evaluate zero-point differences between various observations. Crowding is not a serious problem in the outer cluster regions and high-precision photometric measurements are relatively easy to obtain. But field-to-field zero-point variations must be accounted for to have the external fields of the same cluster on the same photometric scale. The main source of this photometric offsets between catalogues of distinct fields, is related to PSF modelling. The PSF model by construction is normalized to a surface flux of unity within a radius of 10 ACS/WFC pixels (0.5 arcsecond). Only the inner 5×5-pixel region of sources was used to fit to the PSF model in order to minimize the contaminating impact of nearby neighbors, but any mismatch between the adopted PSF model and the pixels beyond the small square fitting aperture would result in a slight zeropoint shift. The fact that we perturb the library PSFs (above) minimizes this even further. However, the best way to regularize the photometry is empirically: following Bedin et al. (2005) and Anderson et al. (2008a), we measured aperture corrections inside

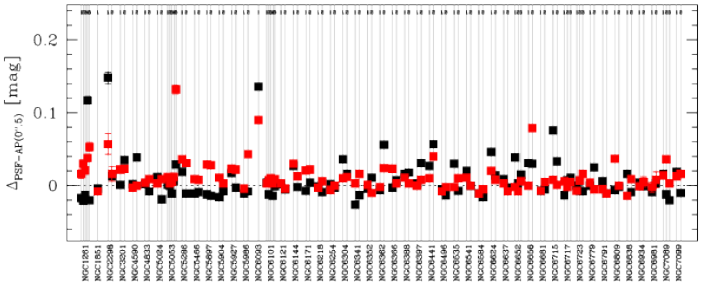

Figure 4.2: Aperture corrections measured in each field for each cluster. Red squares refer to F475W observations, while black squares refer to F814W ones.

this aperture using the calibrated and drizzled (`drc`) images as reference.

These corrections were sufficient to properly take into account the majority of the photometric biases in our catalogues. The obtained values of the aperture correction for an aperture of 0.5 arcseconds are listed in Tables 4.5 and 4.6. We maintain the same nomenclature as in Bedin et al. (2005). The aperture correction values, along with their associated uncertainties are also reported in Figure 4.2. Black dots are referred to F814W observations, red dots to F475W ones. It can be noted that for the majority of cases corrections are small: typically smaller than 0.04 magnitudes, but in the most severe cases, they can reach values as high as 0.15 mag.

Astrometrised, stacked images of each observed field have also been produced for both filters with a 1×1 pixel sampling. These have been created, for each field, combining all overlapping `flc` images using the same coordinate transformations that define the common reference frames.

Astrometric solutions have been independently derived using the *Gaia* DR1 catalogue as a reference (Gaia Collaboration et al. 2016). As a consequence, positions are given for Equinox J2000 at epoch 2015. Table 4.7 reports the precision reached by the new astrometric solution in the fifth column, which is the root mean square error of the offset between *Gaia* positions and those derived, for the same stars, in our astrometrised stacked images. The measured average value is 0.2 pixel, or $\sim$ 10 milliarcseconds. These values are also visualised in Figure 4.3.

For completeness, we also measure the astrometric precision of the origi-

Table 4.5: Tabulated $\Delta m_{\rm PSF-AP(0''.5)}$ values used in the aperture correction

#	CLUSTER	FIELD	$\Delta m^{\rm F475W}_{\rm PSF-AP(0''.5)}$ mag	$\Delta m^{\rm F814W}_{\rm PSF-AP(0''.5)}$ mag
01	NGC1261	1	$+0.016 \pm 0.006$	-0.017 ± 0.003
		2	$+0.030 \pm 0.005$	-0.021 ± 0.002
		3	$+0.021 \pm 0.005$	-0.013 ± 0.002
		4	$+0.038 \pm 0.005$	$+0.117 \pm 0.005$
		5	$+0.053 \pm 0.006$	-0.020 ± 0.003
02	NGC1851	1+2	-0.008 ± 0.002	-0.004 ± 0.001
03	NGC2298	1	$+0.057 \pm 0.014$	$+0.148 \pm 0.008$
		2	$+0.016 \pm 0.010$	$+0.013 \pm 0.005$
04	NGC3201	1	$+0.022 \pm 0.001$	$+0.001 \pm 0.001$
		2	$+0.023 \pm 0.001$	$+0.035 \pm 0.001$
05	NGC4590	1	-0.003 ± 0.003	$+0.002 \pm 0.002$
		2	0.000 ± 0.003	$+0.039 \pm 0.002$
06	NGC4833	1	$+0.004 \pm 0.002$	$+0.002 \pm 0.001$
		2	$+0.009 \pm 0.001$	-0.008 ± 0.001
07	NGC5024	1	$+0.003 \pm 0.001$	$+0.012 \pm 0.001$
		2	$+0.009 \pm 0.003$	-0.019 ± 0.001
08	NGC5053	1	$+0.012 \pm 0.004$	$+0.001 \pm 0.004$
		2	$+0.003 \pm 0.004$	0.000 ± 0.003
		3	$+0.005 \pm 0.005$	-0.011 ± 0.003
		4	$+0.012 \pm 0.005$	$+0.006 \pm 0.003$
		5	$+0.132 \pm 0.006$	$+0.029 \pm 0.003$
09	NGC5286	1	$+0.036 \pm 0.003$	$+0.019 \pm 0.002$
		2	$+0.031 \pm 0.004$	-0.011 ± 0.001
10	NGC5466	1	$+0.009 \pm 0.003$	-0.011 ± 0.003
		2	$+0.008 \pm 0.003$	-0.009 ± 0.002
11	NGC5897	1	$+0.029 \pm 0.003$	-0.012 ± 0.001
		2	$+0.028 \pm 0.003$	-0.014 ± 0.001
12	NGC5904	1	$+0.011 \pm 0.001$	-0.016 ± 0.001
		2	$+0.003 \pm 0.001$	-0.008 ± 0.001
13	NGC5927	1	$+0.023 \pm 0.002$	$+0.017 \pm 0.001$
		2	$+0.022 \pm 0.002$	-0.003 ± 0.001
14	NGC5986	1	-0.004 ± 0.002	-0.011 ± 0.001
		2	$+0.043 \pm 0.004$	-0.008 ± 0.001
15	NGC6093	1	$+0.090 \pm 0.002$	$+0.136 \pm 0.002$
16	NGC6101	1	$+0.003 \pm 0.003$	$+0.004 \pm 0.002$
		2	$+0.007 \pm 0.003$	-0.012 ± 0.001
		3	$+0.010 \pm 0.004$	$+0.004 \pm 0.002$
		4	$+0.003 \pm 0.002$	-0.014 ± 0.001
		5	$+0.009 \pm 0.002$	-0.001 ± 0.001
17	NGC6121	1	$+0.003 \pm 0.002$	$+0.002 \pm 0.001$
		2	-0.004 ± 0.003	-0.005 ± 0.001
18	NGC6144	1	$+0.030 \pm 0.004$	$+0.027 \pm 0.001$
		2	$+0.013 \pm 0.004$	-0.002 ± 0.001
19	NGC6171	1	$+0.021 \pm 0.002$	-0.007 ± 0.002
		2	$+0.022 \pm 0.002$	$+0.004 \pm 0.002$
20	NGC6218	1	-0.003 ± 0.002	-0.001 ± 0.001
		2	$+0.006 \pm 0.002$	-0.009 ± 0.001
21	NGC6254	1	-0.006 ± 0.002	$+0.002 \pm 0.001$
		2	0.000 ± 0.002	-0.003 ± 0.001
22	NGC6304	1	$+0.010 \pm 0.001$	$+0.036 \pm 0.001$
		2	$+0.012 \pm 0.002$	$+0.016 \pm 0.001$
23	NGC6341	1	$+0.003 \pm 0.002$	-0.026 ± 0.001
		2	$+0.016 \pm 0.002$	-0.013 ± 0.001
24	NGC6352	1	$+0.001 \pm 0.001$	-0.004 ± 0.001
		2	-0.010 ± 0.001	$+0.011 \pm 0.001$

Continued on Tab. 4.6

Table 4.6: Table 4.5 (continued)

#	CLUSTER	FIELD	$\Delta m^{F475W}_{PSF-AP(0''.5)}$ mag	$\Delta m^{F814W}_{PSF-AP(0''.5)}$ mag
25	NGC6362	1	-0.002 ± 0.002	-0.006 ± 0.001
		2	$+0.024 \pm 0.003$	$+0.056 \pm 0.001$
26	NGC6366	1	$+0.023 \pm 0.005$	-0.003 ± 0.001
		2	$+0.003 \pm 0.002$	$+0.007 \pm 0.001$
27	NGC6388	1	$+0.011 \pm 0.001$	$+0.016 \pm 0.001$
		2	$+0.003 \pm 0.001$	$+0.018 \pm 0.001$
28	NGC6397	1	0.000 ± 0.001	$+0.003 \pm 0.001$
		2	$+0.008 \pm 0.002$	$+0.031 \pm 0.001$
29	NGC6441	1	$+0.010 \pm 0.001$	$+0.027 \pm 0.001$
		2	$+0.040 \pm 0.001$	$+0.057 \pm 0.001$
30	NGC6496	1	-0.008 ± 0.002	-0.005 ± 0.001
		2	-0.002 ± 0.001	-0.013 ± 0.001
31	NGC6535	1	-0.002 ± 0.002	$+0.030 \pm 0.001$
		2	$+0.010 \pm 0.003$	-0.007 ± 0.001
32	NGC6541	1	$+0.011 \pm 0.001$	$+0.020 \pm 0.001$
		2	0.000 ± 0.002	0.000 ± 0.001
33	NGC6584	1	-0.011 ± 0.003	-0.011 ± 0.001
		2	-0.005 ± 0.004	-0.016 ± 0.001
34	NGC6624	1	$+0.020 \pm 0.001$	$+0.046 \pm 0.001$
		2	$+0.008 \pm 0.001$	$+0.014 \pm 0.001$
35	NGC6637	1	$+0.003 \pm 0.001$	$+0.009 \pm 0.001$
		2	-0.008 ± 0.001	-0.003 ± 0.001
36	NGC6652	1	-0.002 ± 0.002	$+0.039 \pm 0.001$
		2	-0.008 ± 0.002	$+0.003 \pm 0.001$
		3	$+0.006 \pm 0.001$	$+0.015 \pm 0.001$
37	NGC6656	1	0.000 ± 0.001	$+0.031 \pm 0.001$
		2	$+0.079 \pm 0.001$	$+0.030 \pm 0.001$
38	NGC6681	1	-0.007 ± 0.001	-0.007 ± 0.001
		2	$+0.005 \pm 0.001$	-0.005 ± 0.001
39	NGC6715	1	$+0.008 \pm 0.001$	$+0.076 \pm 0.001$
		2	$+0.001 \pm 0.001$	$+0.033 \pm 0.001$
40	NGC6717	1	$+0.006 \pm 0.002$	-0.013 ± 0.001
		2	-0.002 ± 0.002	$+0.007 \pm 0.001$
		3	$+0.005 \pm 0.001$	$+0.011 \pm 0.001$
41	NGC6723	1	-0.007 ± 0.003	0.000 ± 0.001
		2	$+0.007 \pm 0.002$	-0.007 ± 0.001
		3	$+0.016 \pm 0.003$	-0.008 ± 0.001
42	NGC6779	1	$+0.004 \pm 0.003$	0.000 ± 0.002
		2	-0.005 ± 0.002	$+0.025 \pm 0.002$
43	NGC6791	1	-0.005 ± 0.004	$+0.006 \pm 0.002$
		2	-0.011 ± 0.003	-0.011 ± 0.001
44	NGC6809	1	$+0.037 \pm 0.002$	-0.006 ± 0.001
		2	0.000 ± 0.001	-0.002 ± 0.001
45	NGC6838	1	-0.014 ± 0.002	$+0.016 \pm 0.001$
		2	$+0.009 \pm 0.002$	-0.009 ± 0.001
46	NGC6934	1	-0.001 ± 0.005	$+0.004 \pm 0.002$
		2	$+0.005 \pm 0.007$	-0.001 ± 0.003
47	NGC6981	1	-0.002 ± 0.007	-0.009 ± 0.003
		2	$+0.008 \pm 0.011$	$+0.003 \pm 0.005$
48	NGC7089	1	$+0.014 \pm 0.003$	$+0.016 \pm 0.001$
		2	$+0.036 \pm 0.002$	-0.012 ± 0.001
		3	$+0.003 \pm 0.002$	-0.020 ± 0.001
49	NGC7099	1	$+0.013 \pm 0.003$	$+0.019 \pm 0.002$
		2	$+0.016 \pm 0.004$	-0.010 ± 0.002

Table 4.7: Precision reached with the re-derived astrometric solution using *Gaia* catalogues; for completeness we report the number of reference stars used. We also provide measures of the accuracy of the original STScI astrometric solution in the form of differences between RA and DEC.

#	CLUSTER	F	stars	precision mas	ΔRA WFC px	ΔDEC WFC px
01	NGC1261	1	32	15.5	1.66 ± 0.34	-4.50 ± 0.16
		2	41	10.0	-1.89 ± 0.08	4.31 ± 0.21
		3	37	8.0	-0.51 ± 0.06	1.61 ± 0.18
		4	36	11.0	-0.50 ± 0.14	1.03 ± 0.31
		5	46	10.0	0.07 ± 0.05	-4.81 ± 0.19
02	NGC1851	1+2	232	10.0	3.54 ± 0.20	-4.25 ± 0.19
03	NGC2298	1	79	16.5	-0.17 ± 0.04	5.62 ± 0.24
		2	53	14.0	-0.11 ± 0.06	-1.37 ± 0.25
04	NGC3201	1	635	13.0	0.14 ± 0.32	-0.57 ± 0.23
		2	653	10.0	4.33 ± 0.33	8.39 ± 0.20
05	NGC4590	1	110	11.0	-0.78 ± 0.10	4.90 ± 0.15
		2	111	11.5	-0.12 ± 0.04	-3.86 ± 0.17
06	NGC4833	1	492	7.0	-3.53 ± 0.35	6.86 ± 0.22
		2	570	6.5	1.75 ± 0.15	-0.02 ± 0.20
07	NGC5024	1	173	11.5	-0.14 ± 0.23	3.09 ± 0.20
		2	142	10.0	-45.45 ± 0.77	1.35 ± 0.18
08	NGC5053	1	44	9.5	0.72 ± 0.16	-0.62 ± 0.16
		2	41	8.0	-0.07 ± 0.15	-1.86 ± 0.18
		3	38	8.5	0.22 ± 0.13	0.29 ± 0.23
		4	42	10.0	0.43 ± 0.09	0.23 ± 0.19
		5	52	12.0	0.57 ± 0.16	-0.65 ± 0.16
09	NGC5286	1	215	17.0	1.63 ± 0.20	1.85 ± 0.25
		2	217	16.5	1.61 ± 0.20	1.10 ± 0.21
10	NGC5466	1	56	7.5	-0.13 ± 0.27	1.37 ± 0.12
		2	72	8.0	-0.79 ± 0.29	-2.22 ± 0.20
11	NGC5897	1	164	9.0	0.12 ± 0.22	-0.37 ± 0.20
		2	154	7.5	2.58 ± 0.17	-2.51 ± 0.18
12	NGC5904	1	579	7.0	-1.29 ± 0.19	-2.69 ± 0.15
		2	630	7.0	-0.16 ± 0.15	-1.08 ± 0.22
13	NGC5927	1	848	8.5	3.65 ± 0.30	-0.38 ± 0.20
		2	985	8.0	-9.20 ± 0.35	11.91 ± 0.21
14	NGC5986	1	278	8.0	-0.54 ± 0.30	1.36 ± 0.22
		2	268	6.0	-6.46 ± 0.26	4.12 ± 0.18
15	NGC6093	1	236	22.0	1.81 ± 0.19	-4.47 ± 0.20
16	NGC6101	1	235	7.0	-1.85 ± 0.76	1.09 ± 0.21
		2	232	6.5	-0.80 ± 0.61	2.90 ± 0.20
		3	229	8.0	-15.82 ± 0.73	0.55 ± 0.25
		4	263	11.0	-1.83 ± 0.89	-0.52 ± 0.27
		5	204	8.5	12.13 ± 0.85	-3.52 ± 0.24
17	NGC6121	1	633	7.5	-4.81 ± 0.37	7.07 ± 0.23
		2	649	7.5	-0.69 ± 0.14	1.90 ± 0.22
18	NGC6144	1	147	7.0	-4.48 ± 0.18	-0.10 ± 0.19
		2	147	9.5	-3.09 ± 0.15	-0.76 ± 0.20
19	NGC6171	1	172	9.0	4.44 ± 0.20	-2.36 ± 0.16
		2	196	7.5	-3.26 ± 0.19	-1.51 ± 0.21
20	NGC6218	1	300	10.0	0.40 ± 0.07	-4.05 ± 0.17
		2	362	6.5	-0.72 ± 0.09	0.13 ± 0.19
21	NGC6254	1	525	7.5	-0.94 ± 0.11	2.02 ± 0.20
		2	507	5.0	-0.08 ± 0.12	-0.52 ± 0.18
22	NGC6304	1	1021	11.0	0.00 ± 0.09	7.29 ± 0.22
		2	1137	11.0	-2.63 ± 0.15	3.66 ± 0.28
23	NGC6341	1	272	7.0	3.31 ± 0.13	-1.46 ± 0.17
		2	276	6.5	1.30 ± 0.16	2.01 ± 0.14

continued on Table 4.8

Table 4.8: Table 4.7 (continued)

#	CLUSTER	F	stars	precision mas	ΔRA WFC px	ΔDEC WFC px
24	NGC6352	1	676	8.0	0.44 ± 0.09	6.24 ± 0.18
		2	658	9.5	0.20 ± 0.11	0.84 ± 0.21
25	NGC6362	1	399	6.0	-1.98 ± 0.18	-1.19 ± 0.20
		2	412	6.0	-0.15 ± 0.23	2.51 ± 0.17
26	NGC6366	1	265	7.0	1.07 ± 0.11	-4.03 ± 0.22
		2	263	6.0	2.89 ± 0.19	4.66 ± 0.18
27	NGC6388	1	812	6.5	1.68 ± 0.24	4.01 ± 0.26
		2	873	7.0	-0.86 ± 0.22	5.67 ± 0.22
28	NGC6397	1	605	8.0	16.46 ± 0.47	12.42 ± 0.26
		2	602	7.0	-4.15 ± 0.33	4.79 ± 0.30
29	NGC6441	1	1075	10.0	34.98 ± 0.54	-3.77 ± 0.26
		2	1114	9.5	4.46 ± 0.31	3.80 ± 0.27
30	NGC6496	1	482	6.0	1.85 ± 0.30	7.03 ± 0.21
		2	525	9.0	8.00 ± 0.28	1.65 ± 0.22
31	NGC6535	1	304	6.5	-4.97 ± 0.19	0.75 ± 0.18
		2	275	7.5	-1.78 ± 0.18	-9.16 ± 0.20
32	NGC6541	1	385	7.5	-11.12 ± 0.28	7.28 ± 0.23
		2	481	9.0	-7.23 ± 0.32	7.72 ± 0.22
33	NGC6584	1	119	7.5	1.82 ± 0.19	6.15 ± 0.24
		2	141	10.0	2.67 ± 0.14	2.71 ± 0.25
34	NGC6624	1	360	8.5	0.83 ± 0.12	1.93 ± 0.23
		2	774	9.5	0.61 ± 0.15	6.08 ± 0.21
35	NGC6637	1	620	10.0	-3.66 ± 0.20	1.83 ± 0.25
		2	615	11.5	-2.54 ± 0.23	-0.80 ± 0.29
36	NGC6652	1	608	12.0	0.35 ± 0.09	5.17 ± 0.26
		2	624	9.5	-0.06 ± 0.06	2.40 ± 0.25
		3	682	7.0	0.49 ± 0.15	5.78 ± 0.21
37	NGC6656	1	734	31.0	-1.20 ± 0.21	3.03 ± 0.25
		2	1052	27.5	1.21 ± 0.30	6.93 ± 0.31
38	NGC6681	1	450	14.0	-4.20 ± 0.25	1.76 ± 0.29
		2	385	15.5	-2.37 ± 0.20	1.75 ± 0.32
39	NGC6715	1	484	16.0	-0.69 ± 0.25	-4.67 ± 0.28
		2	505	15.5	3.28 ± 0.18	-1.79 ± 0.27
40	NGC6717	1	439	14.0	3.48 ± 0.21	0.07 ± 0.30
		2	406	13.0	0.49 ± 0.20	1.11 ± 0.28
		3	445	12.0	0.11 ± 0.18	4.99 ± 0.26
41	NGC6723	1	256	14.5	0.14 ± 0.20	0.95 ± 0.30
		2	144	11.5	-0.25 ± 0.19	4.59 ± 0.22
		3	111	9.0	-0.33 ± 0.16	3.99 ± 0.18
42	NGC6779	1	345	7.5	0.86 ± 0.07	1.07 ± 0.21
		2	333	6.5	3.24 ± 0.16	-8.92 ± 0.19
43	NGC6791	1	288	9.0	-1.92 ± 0.26	-7.50 ± 0.21
		2	274	5.5	-4.98 ± 0.25	-6.18 ± 0.21
44	NGC6809	1	584	7.0	-1.58 ± 0.19	0.99 ± 0.22
		2	590	7.5	-9.19 ± 0.21	-0.68 ± 0.23
45	NGC6838	1	816	7.0	-8.81 ± 0.24	-12.24 ± 0.22
		2	800	6.5	-3.96 ± 0.22	-8.28 ± 0.21
46	NGC6934	1	87	11.5	3.41 ± 0.20	2.62 ± 0.24
		2	84	5.5	1.41 ± 0.10	-12.00 ± 0.17
47	NGC6981	1	31	14.5	1.29 ± 0.26	-9.37 ± 0.19
		2	27	9.5	1.73 ± 0.23	-8.07 ± 0.23
48	NGC7089	1	92	5.5	-0.55 ± 0.12	-6.84 ± 0.15
		2	77	10.5	2.52 ± 0.15	-1.40 ± 0.18
		3	82	11.0	1.85 ± 0.12	-0.54 ± 0.20
49	NGC7099	1	79	4.5	0.93 ± 0.08	-0.89 ± 0.17
		2	89	6.5	0.66 ± 0.08	1.75 ± 0.21

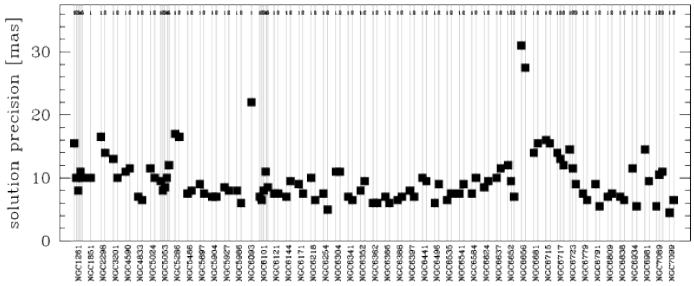

Figure 4.3: Precision of the redefined astrometric solution for each observed field, see text for details.

nal astrometric solution of `drc` images. The position offset between common sources in the *Gaia* DR1 catalogue and the `drc` images is used to define this quantity. Offset values are referred to RA and DEC distances in image pixels and are reported in columns six and seven of Table 4.7. The associated errors corresponds to the measured standard deviations of each sample. A visual representation is also given in Figure 4.4. It can be noted that, in general, offsets are lower than 5 ACS/WFC pixels (0.25 arcseconds), and, in many cases, below 1 pixel, with some notable exceptions.

4.3 The Colour-Magnitude Diagrams and trichromatic stacked images

In Figure 4.5 we report the CMDs obtained for all 5 fields of NGC 1261. Magnitudes are given both in the instrumental and Vega-mag photometric systems. Dashed lines represent the saturation limit, black dots represent unsaturated stars, saturated stars are represented with crosses. The five CMDs are all merged in the bottom-right panel, where a different colour have been assigned to each different field. In this case, the instrumental magnitude scale, along with saturation level (dashed line), refer only to Field 1.

The final CMDs for all other targets are presented in Figures 4.16 - 4.23. The presented CMDs have been obtained by selecting only high-quality stars, according to quality parameters presented in Anderson et al. (2008a). In Section 4.4 we describe the adopted selection procedure. It is important to mention

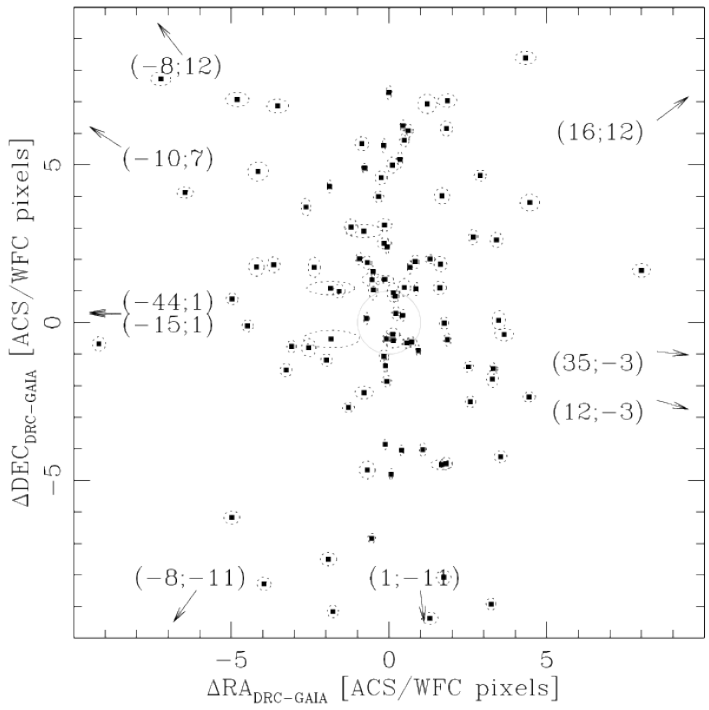

Figure 4.4: Offsets between star positions obtained using the original STScI astrometric solution (header of `drc` images) and *Gaia* ones. Points represent single fields; the semi-axes of each ellipse have length equal to the measured standard deviation. The gray circle represents an offset of 1 ACS/WFC pixel, which corresponds to ~ 0.05 arcseconds. Some points falls outside the used limits; we indicate their position along the edges of the figure, the arrows point in their direction.

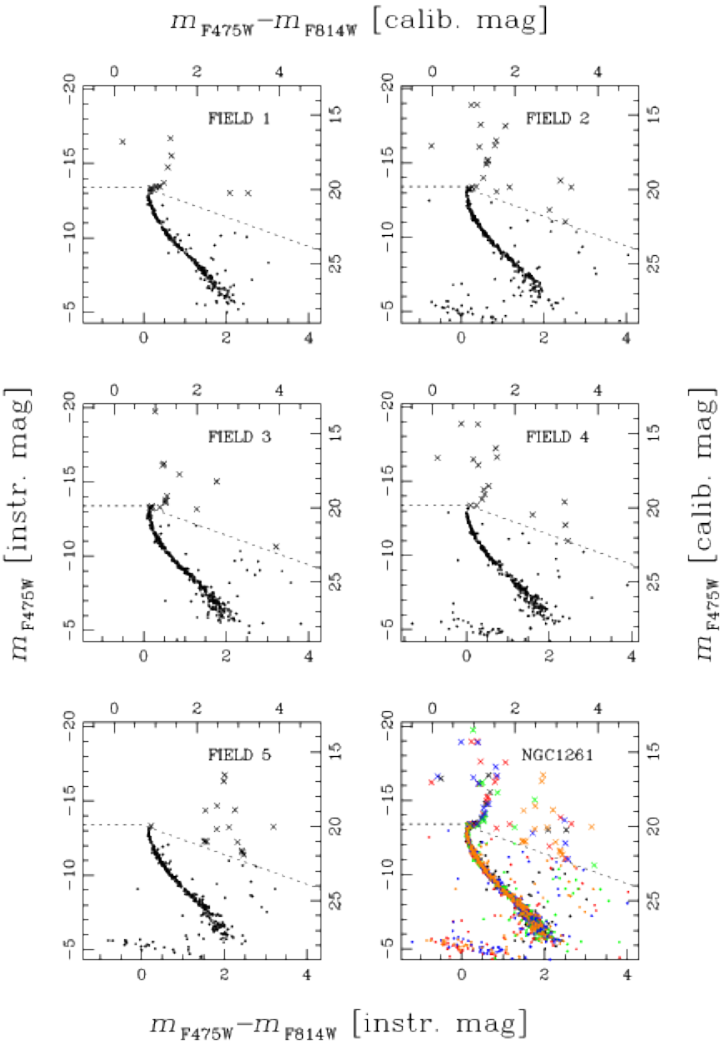

Figure 4.5: CMDs of the parallel fields of NGC 1261. Both instrumental and calibrated magnitude scales are shown. Dashed lines represent the saturation levels. Saturated stars are marked with crosses. The bottom-right panel collects all the stars present in all the five fields. Stars are here colour-coded as follows. Black dots represent stars measured in F1, red dots stars of F2, green dots stars of F3, blue dots stars of F4, and orange dots represent stars measured in F5. The instrumental magnitude scale and the saturation limit refer to F1 only.

here that, since in the majority of the cases only one image per filter has been taken, artifact rejection is not an easy task. In order to include faint sources, we have chosen not to limit in flux our raw catalogues. We nonetheless restricted the detections only to those sources observed in at least one F814W and one F475W image simultaneously, with positions in the common reference frame consistent within 0.8 pixels.

No rejection of foreground/background contamination has been performed, nor any correction for differential reddening. The homogeneity of the data guarantees very similar results in every case. Nonetheless, it is out of the scope of the present work to characterize in detail the obtained results, which require taking into consideration several issues. For example, the number density of cluster members present in the observed fields depends on the properties of each GC: in some cases, especially for bulge clusters, or those that appear projected in this dense Galactic region, it is difficult to identify the cluster sequence. We recall that another interesting application of the present data is the study of the stellar populations, external to the clusters, that contaminate the observed fields. In particular, for at least 6 GCs, namely NGC 6624, NGC 6637, NGC 6652, NGC 6681, NGC 6715 and NGC 6809, traces of the Sagittarius Stream are visible in the obtained CMDs (Siegel et al. 2011).

As an additional tool to explore and characterize observations, we have created colour images of each observed field, combining the astrometrised stacked images: an example is shown in Figure 4.6. The F814W stacked images have been associated with red channel while the F475W images are associated to the blue channel. The images associated to the green channel have been obtained as a result of a 3:1 weighted mean of F475W and F814W counts respectively.

4.4 Selection of well-measured stars

This section describes the procedure adopted to reject spurious or poorly measured sources in the catalogues and to obtain a sample of bona-fide stellar sources. In this example we refer to the catalogue associated to Field 1 of NGC 6121 (M4). The V3 PA is 272 degrees and, for this field, 2 images were collected, one in F814W, and the other in F475W (666 and 739 seconds respectively).

For the selection, we have adopted a procedure similar to that described in Milone et al. (2012c), defining limits in both q and o (quality) parameters. In addition, we also made use of the $RADXS$ parameter (Bedin et al. 2008, Bedin et al. 2009, Bedin et al. 2010).

As shown in the lower left panels of Figure 4.7, the q parameter displays a characteristic trend with magnitude. This parameter is defined as the absolute

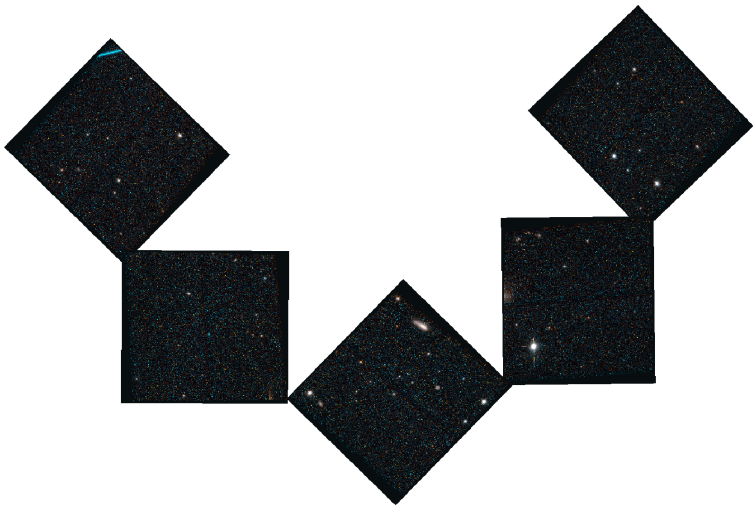

Figure 4.6: Mosaic of all trichromatic images created for NGC 1261; see text for details.

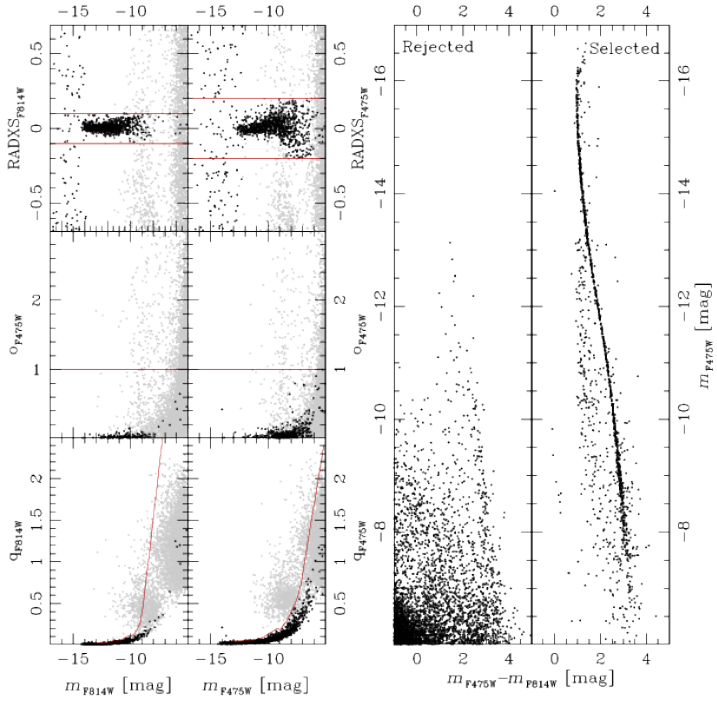

Figure 4.7: Selection procedure for Field 1 of NGC 6121. Left panels: black points mark the stars that were selected as well-measured. Red lines mark the limits chosen for the q, o and $RADXS$ parameters. Second panel from right: CMD of rejected sources. Right panel: CMD with only sources that survived the selection. All plots refer to instrumental magnitudes.

value of the subtraction between the PSF model and the spatial distribution of light of a particular detection in the image, inside the fitting radius. For a perfectly modeled source, the q parameter assumes value 0.

The o parameter quantifies the amount of light that falls on the aperture used for PSF fitting, due to neighboring sources (Anderson et al. 2008a). Unlike the q parameter, it does not shows a clear trend with magnitude (middle-left panels of Figure 4.7), for this reason we have used a fixed limit (Milone et al. 2012c).

Finally, the $RADXS$ parameter is related to the spatial extent of the sources, and it is used to distinguish between point sources and extended sources. It is defined as the flux in excess of that predicted from the PSF fitting just outside the core of each source (Bedin et al. 2008). Positive values are expected for extended objects, while negative values indicate detections that are sharper than stellar. The introduction of this parameter in the selection process for the present case is particularly necessary: since only one image per filter is available for most cases, spurious detections due to cosmic rays are present in the catalogues. Moreover, these observations cover the external regions of GCs, where the stellar density is not as high as in the central regions. The observed fields are thus relatively populated by extra-galactic, non-stellar objects.

We started by taking a more stringent limit in position-consistency for each source. We selected only sources with an rms error in position less than 0.3 pixel. We adopted fixed limits in the o and $RADXS$ parameters for both filters simultaneously. Finally, we measured, for the sources that survived this first selection, the median trend in the plane defined by magnitude and q parameter values. In this way, we removed from the sample non-stellar and poorly-measured sources, while not a priori losing faint sources. Red lines in the left panels of Figure 4.7 represent the limits used for the case of Field 1 of NGC 6121 (M4). Black points represent sources that passed the selection process. The CMD corresponding to rejected sources (grey dots in the left panels) is shown in the second panel from the right.

The resulting CMD is shown in the right panel of Figure 4.7. Note how the cleaning process allows the clear detection of the white-dwarf cooling sequence. Saturated stars have been excluded from the selection procedure, but their fluxes have been recovered using the procedure described in Gilliland (2004).

4.5 Released Electronic Material

We release, for each ACS/WFC parallel field, the astrometric and photometric catalogues and trichromatic astrometrised stacked images. All the released material will be available for download at the website of the Exoplanets & Stellar Populations Group of the Università degli Studi di Padova[1].

Table 4.9 shows the first ten rows of the catalogue produced for Field 1 of NGC 6121. The content of each column is explained in detail in Table 4.10. The parameters *wi* and *wb* are the same as in Anderson et al. (2008a). They are records that represent the level of saturation of each source in F814W and F475W images respectively. The last column includes the results of the selection of well-measured stars presented in Section 4.4.

Note that for many stars, we report a magnitude rms error of 9.900. This is because the routine empirically determines errors based on multiple observations in each filter. When there is only one observation per filter, the error is given a high default value.

[1] `http://groups.dfa.unipd.it/ESPG/treasury.php`

Table 4.9: First ten rows extracted from the catalogue referring to Field 1 of NGC 6121 (M4). A detailed description of each column is given in Table 4.10.

#id	ra(2015)	dec(2015)	x	dx	y	dy	F814W	di	F475W	db	q1	qb	oi	ob	RADXS1	RADXSb	ni	nb	wi	wb	good
00000001	245.78962440	−26.47823845	549.416	0.353	688.174	0.224	28.832	9.900	27.078	9.900	1.620	0.760	1.526	0.115	−0.9900	−0.9157	1	1	1	1	0
00000002	245.78961100	−26.47812901	557.336	0.452	687.260	0.382	26.948	9.900	29.764	9.900	1.384	1.274	0.772	9.900	6.2647	−0.9900	1	1	1	1	0
00000003	245.78968050	−26.47823281	549.844	0.632	691.807	0.152	27.164	9.900	28.433	9.900	1.285	1.234	0.179	0.998	−0.9900	−0.9900	1	1	1	1	0
00000004	245.78969050	−26.47817087	554.332	0.391	692.424	0.136	27.335	9.900	30.545	9.900	1.229	1.715	1.014	2.384	0.9430	−0.9900	1	1	1	1	0
00000005	245.78969230	−26.47815496	556.485	0.426	692.537	0.076	27.109	9.900	29.691	9.900	1.189	1.274	0.404	9.900	2.2225	−0.9900	1	1	1	1	0
00000006	245.78973530	−26.47813294	557.094	0.032	695.317	0.263	28.421	9.900	28.038	9.900	1.204	1.009	3.708	0.336	5.6081	−0.9900	1	1	1	1	0
00000007	245.78971500	−26.47807749	561.102	0.068	693.975	0.088	27.108	9.900	28.184	9.900	1.187	0.948	0.787	0.228	1.0828	−0.9900	1	1	1	1	0
00000008	245.78970010	−26.47806742	561.826	0.001	693.008	0.354	26.711	9.900	30.436	9.900	1.154	1.722	0.354	2.059	−0.9900	−0.9900	1	1	1	1	0
00000009	245.78977530	−26.47818364	553.437	0.442	697.928	0.434	27.300	9.900	28.887	9.900	1.330	1.371	0.459	1.208	−0.7265	9.9900	1	1	1	1	0
00000010	245.79005820	−26.47833427	542.628	0.483	716.320	0.322	26.991	9.900	28.863	9.900	1.025	1.193	0.699	5.580	1.8430	1.1484	1	1	1	1	0

Table 4.10: Information provided by each catalogue.

Col.	Name	Explanation
01	id	ID number for each star
02	ra	Right Ascension for each star (in deg, epoch 2015)
03	dec	Declination for each star (in deg, epoch 2015)
04	x	x position of each star on the reference frame (in pixels)
05	dx	rms errors associated to x position (in pixels)
06	y	y position of each star on the reference frame (in pixels)
07	dy	rms errors associated to y position (in pixels)
08	F814W	F814W magnitude calibrated into Vegamag system
09	di	rms errors associated to F814W magnitude
10	F475W	F475W magnitude calibrated into Vegamag system
11	db	rms errors associated to F475W magnitude
12	qi	*q* parameter for F814W magnitudes
13	qb	*q* parameter for F475W magnitudes
14	oi	*o* parameter for F814W magnitudes
15	ob	*o* parameter for F475W magnitudes
16	RADXSi	*RADXS* parameter for F814W
17	RADXSb	*RADXS* parameter for F475W
18	ni	number of F814W images the source has been detected in
19	nb	number of F475W images the source has been detected in
20	wi	source of F814W photometry 1: unsaturated in deep; 2: unsaturated in short; 3: saturated in short; 4: saturated in deep;
21	wb	source of F475W photometry (same as wi)
22	good	the source has passed the selction process

4.6 Summary and Conclusions

In the context of the *Hubble Space Telescope* UV Legacy Survey Treasury program of Galactic Globular Clusters (GO-13297; PI: Piotto, Paper I), we are releasing the photometric catalogues relative to the ACS/WFC parallel observations. They represent the first *HST* photometric survey of external regions of Galactic GCs and consist of 109 distinct stellar fields of 49 targets: 48 GCs and one open cluster, NGC 6791.

In the majority of cases, only two images per field were taken, one in F814W and one in F475W, centred at about 6.5 arcminutes from cluster centre. Exposure times were selected in order to obtain reliable photometry of the main

sequence of target GCs.

These observations complement the WFC3 observations of the central regions of the surveyed GCs, and represent valuable tools for different investigations as outlined in Paper I. These data represent a first epoch for future studies aimed at proper motions measurements in these regions. Even without proper motions, these catalogues are suitable to various interesting studies such as measurements of mass functions and binaries fractions in external regions of GCs. Furthermore, crowding is not an issue in these external cluster fields, as a result, this database could be also used as an input list for spectroscopic follow-up, for example for precise chemical tagging of cluster members.

4.7 Extra material

In this section we complement Figures 4.1 and 4.5 with those referred to the rest of the sample. In particular, Figures 4.8, 4.9, 4.10, 4.11, 4.12, 4.13, 4.14 and 4.15 complement the sample of finding charts presented in Figure 4.1. Figures 4.16, 4.17, 4.18, 4.19, 4.20, 4.21, 4.22 and 4.23 are analogs to the lower-right panel of Figure 4.5.

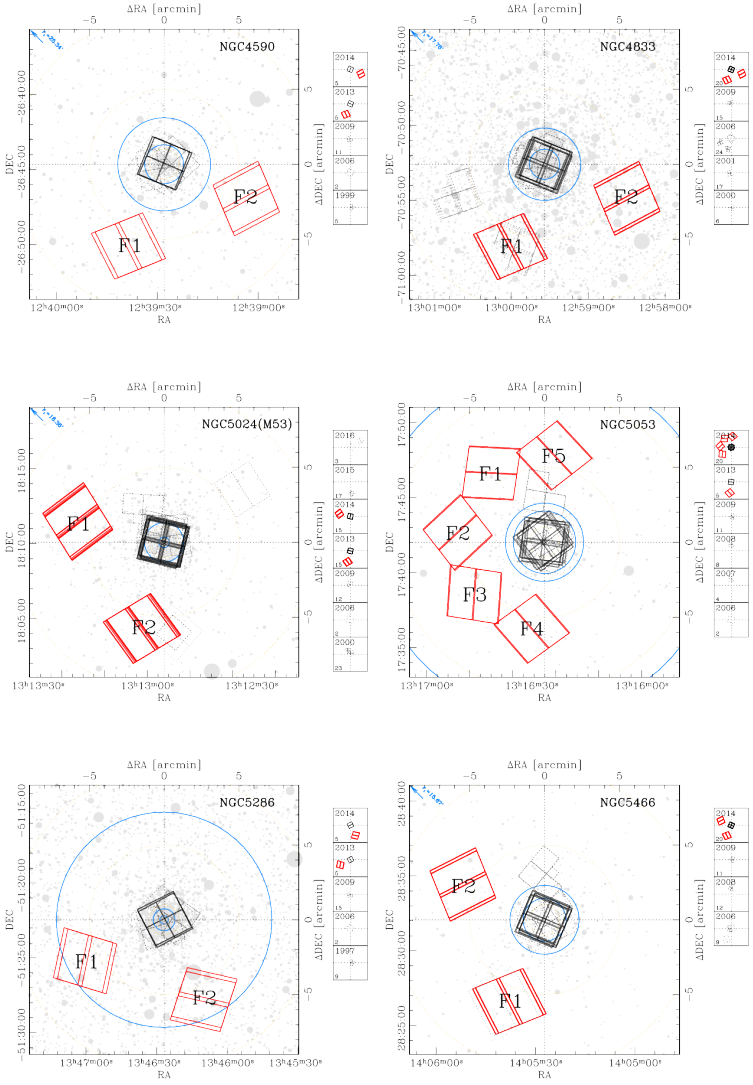

Figure 4.8: As in Figure 4.1 but for NGC 4590, NGC 4833, NGC 5024, NGC 5053, NGC 5286 and NGC 5466

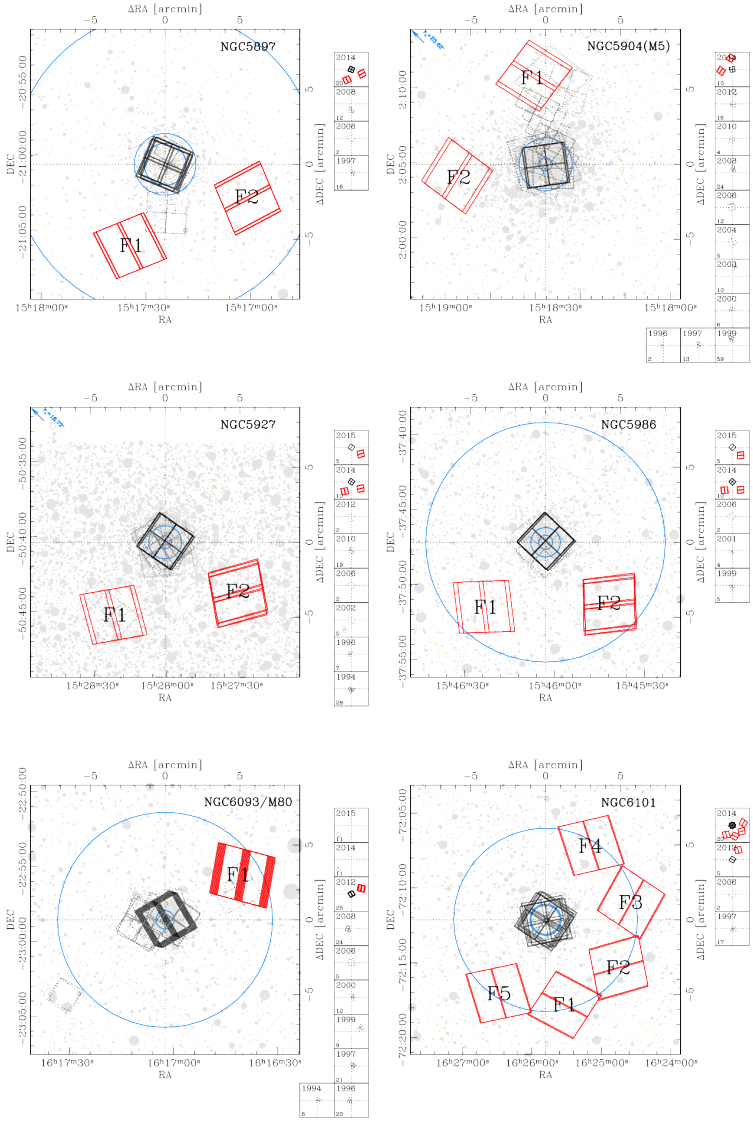

Figure 4.9: As in Figure 4.1 but for NGC 5897, NGC 5904, NGC 5927, NGC 5986, NGC 6093 and NGC 6101

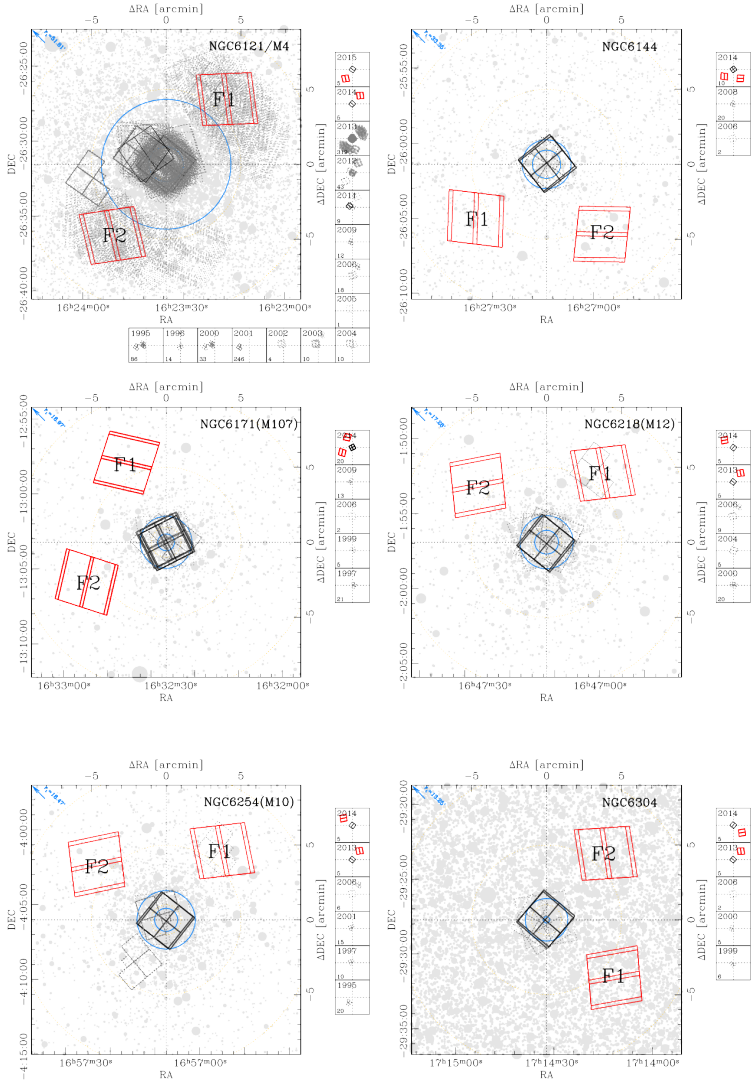

Figure 4.10: As in Figure 4.1 but for NGC 6121, NGC 6144, NGC 6171, NGC 6218, NGC 6254 and NGC 6304

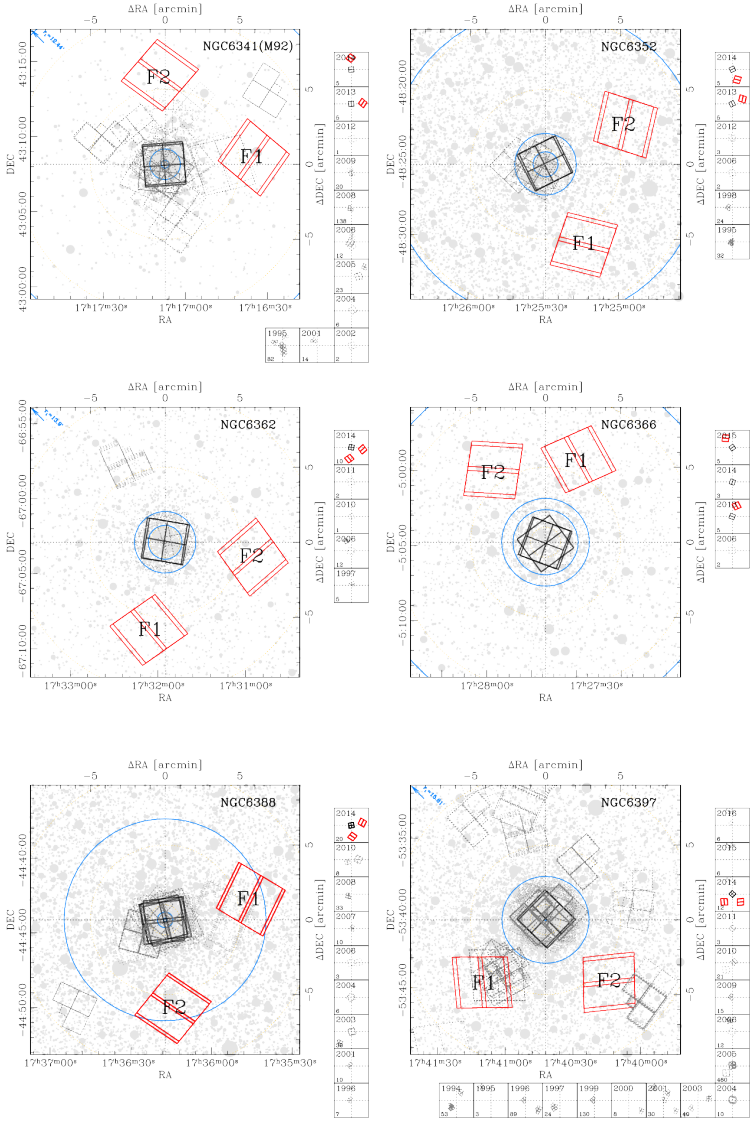

Figure 4.11: As in Figure 4.1 but for NGC 6341, NGC 6352, NGC 6362, NGC 6366, NGC 6388 and NGC 6397

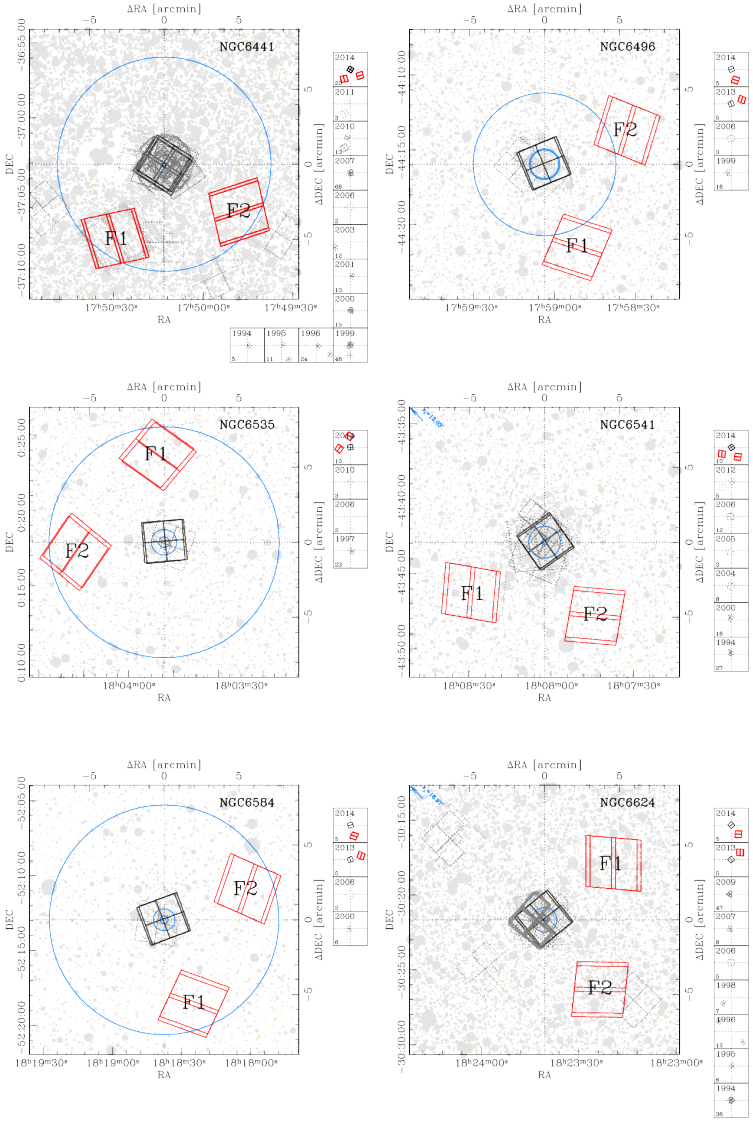

Figure 4.12: As in Figure 4.1 but for NGC 6441, NGC 6496, NGC 6535, NGC 6541, NGC 6584 and NGC 6624

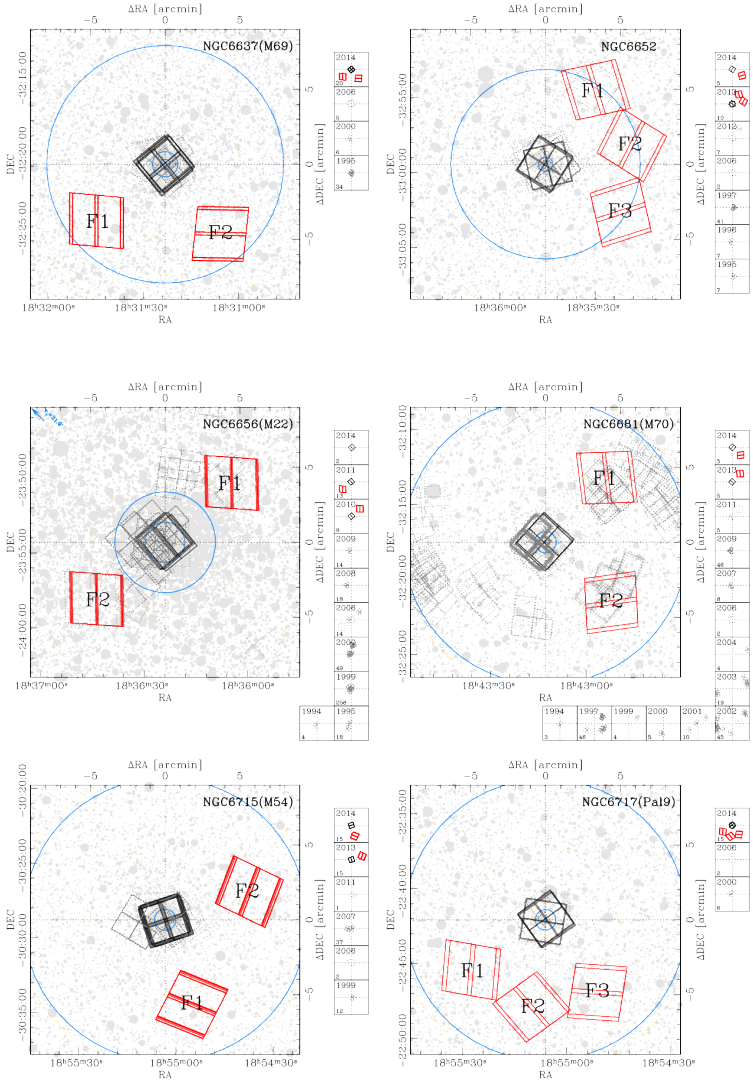

Figure 4.13: As in Figure 4.1 but for NGC 6637, NGC 6652, NGC 6656, NGC 6681, NGC 6715 and NGC 6717

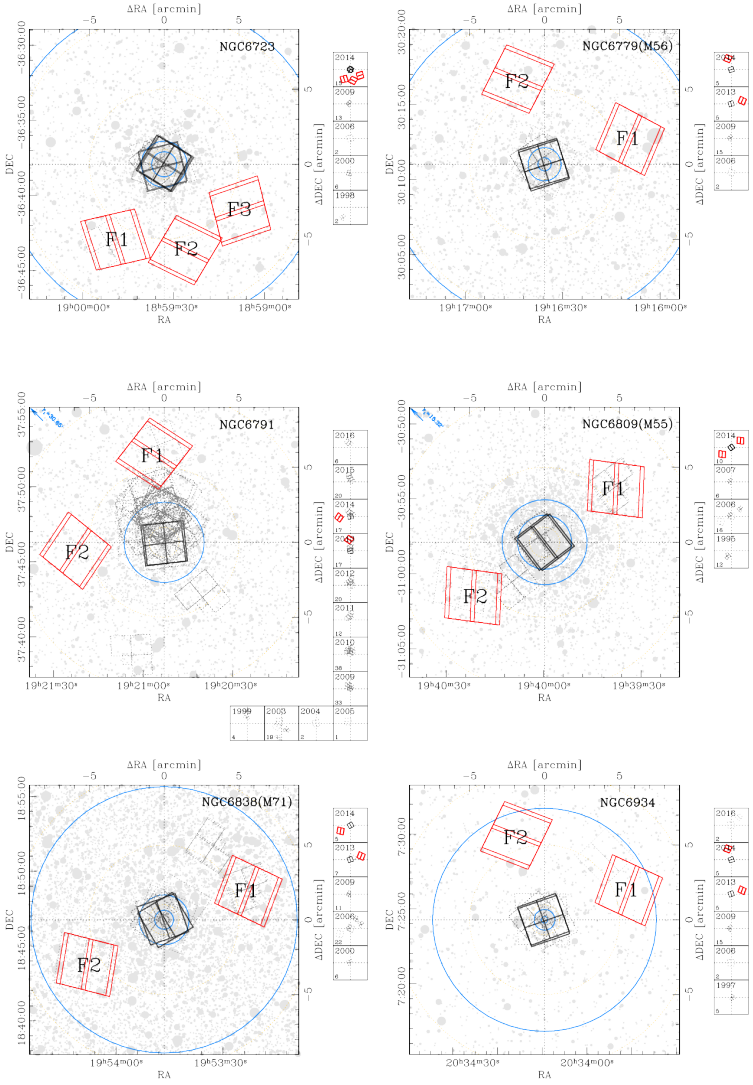

Figure 4.14: As in Figure 4.1 but for NGC 6723, NGC 6779, NGC 6791, NGC 6809, NGC 6838 and NGC 6934

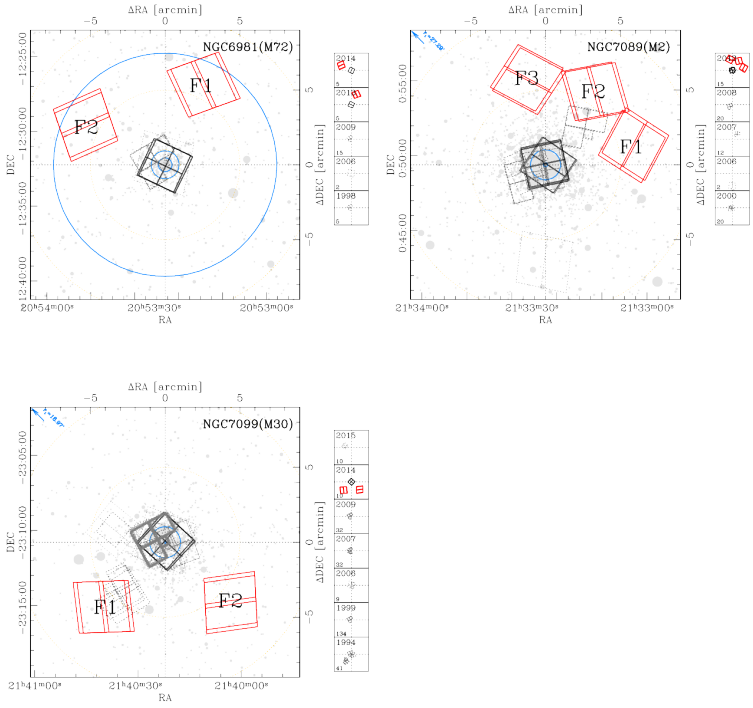

Figure 4.15: As in Figure 4.1 but for NGC 6981, NGC 7089 and NGC 7099

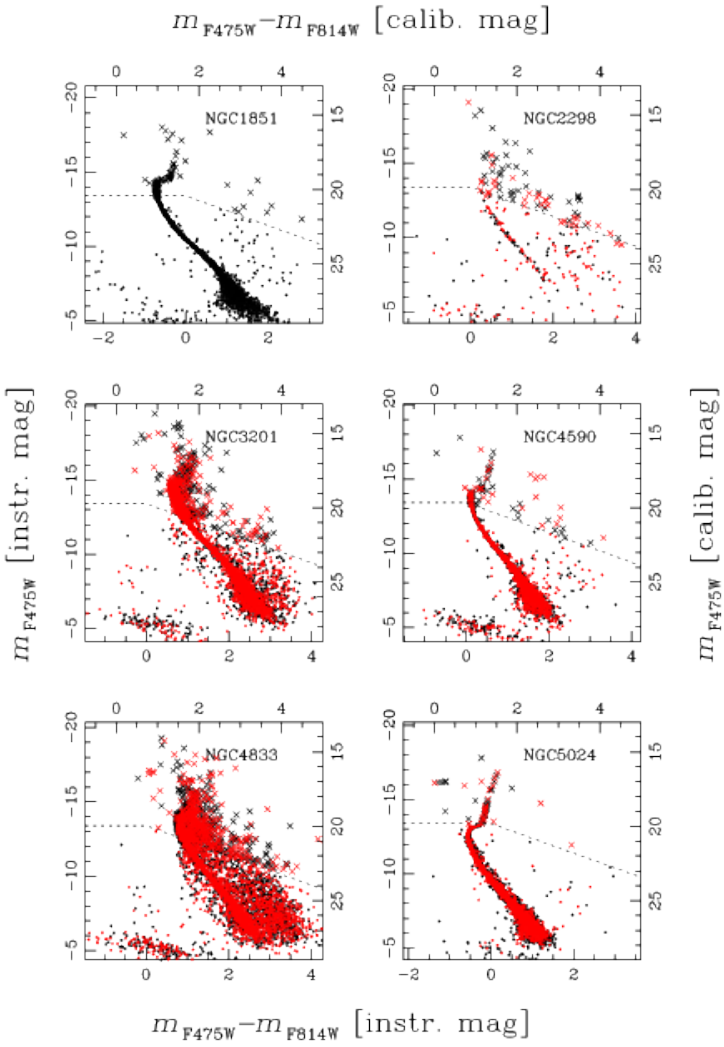

Figure 4.16: Obtained CMDs for NGC 1851, NGC 2298, NGC 3201, NGC 4590 and NGC 5024. For each cluster, CMDs for all fields have been merged together. The colour-code is such that black dots represent stars measured in F1; red dots, stars of F2; green dots stars of F3; blue dots stars of F4 and orange dots represent stars measured in F5. Dashed lines represent the saturation level for all F1, saturated stars are represented by crosses.

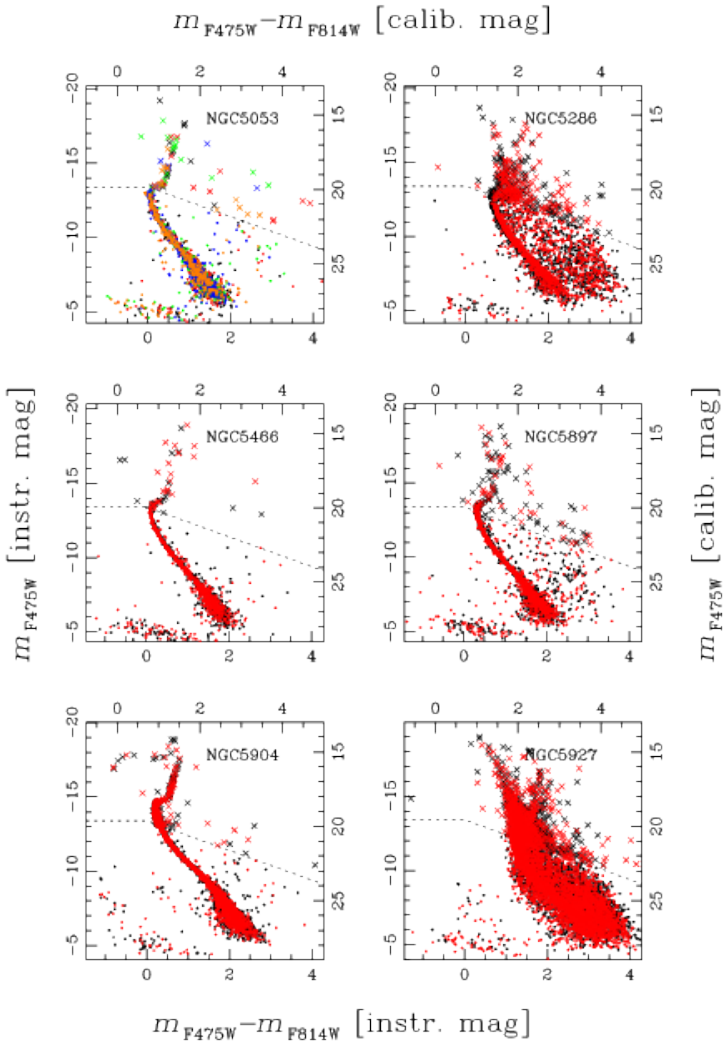

Figure 4.17: As in Figure 4.16 but for NGC 5053, NGC 5286, NGC 5466, NGC 5897, NGC 5904 and NGC 5927

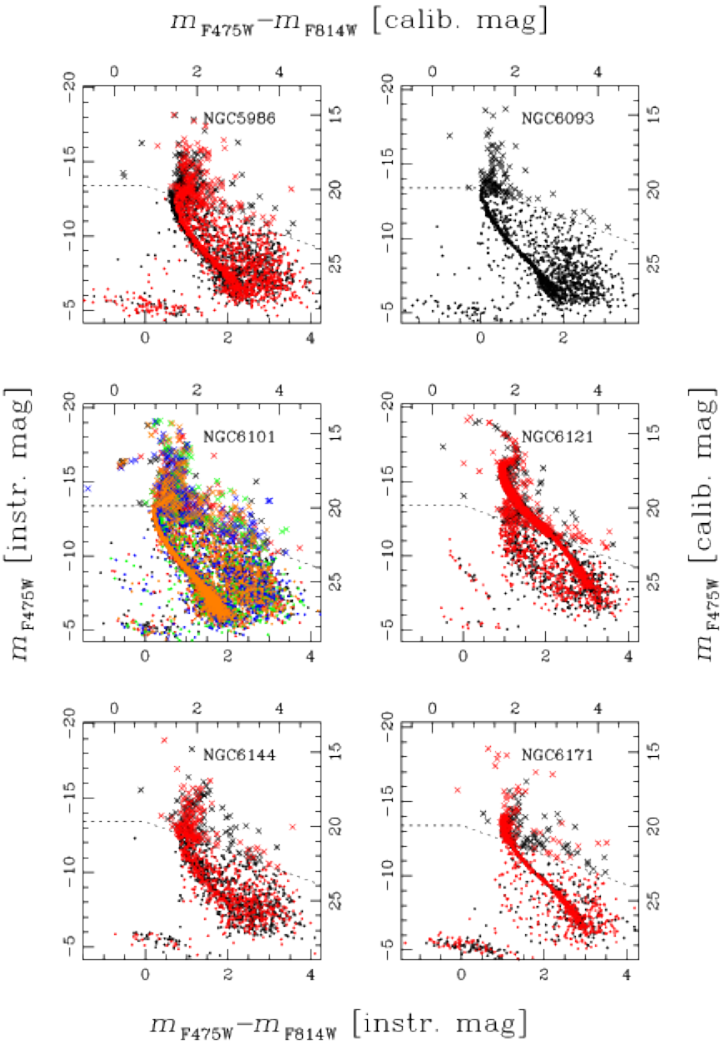

Figure 4.18: As in Figure 4.16 but for NGC 5986, NGC 6093, NGC 6101, NGC 6121, NGC 6144 and NGC 6171

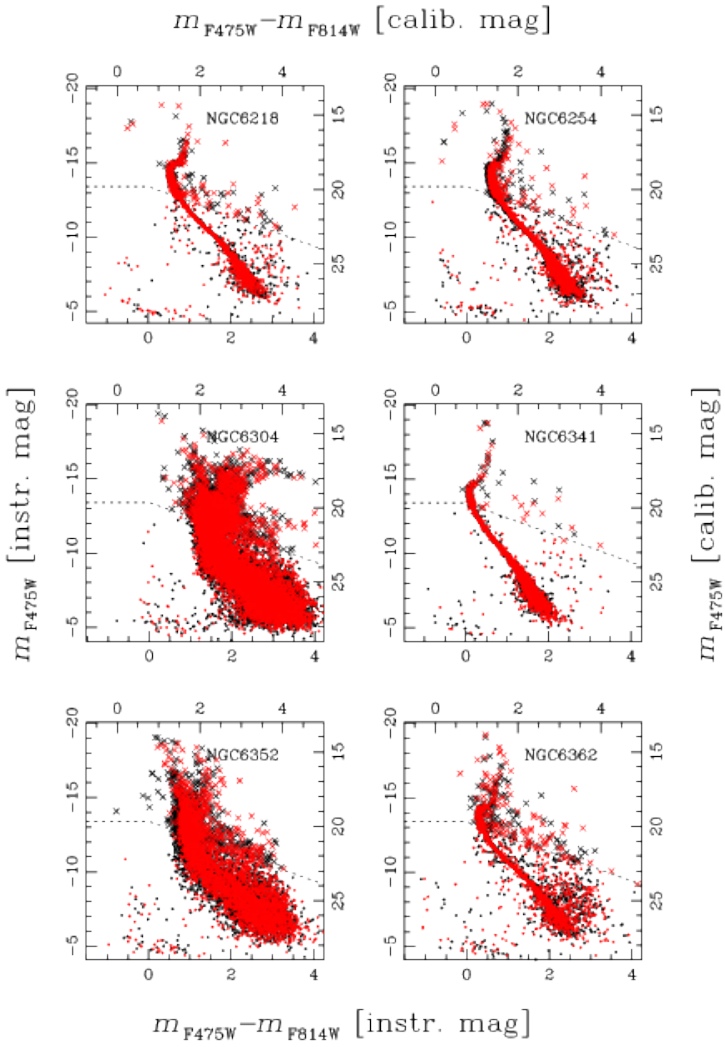

Figure 4.19: As in Figure 4.16 but for NGC 6218, NGC 6254, NGC 6304, NGC 6341, NGC 6352 and NGC 6362

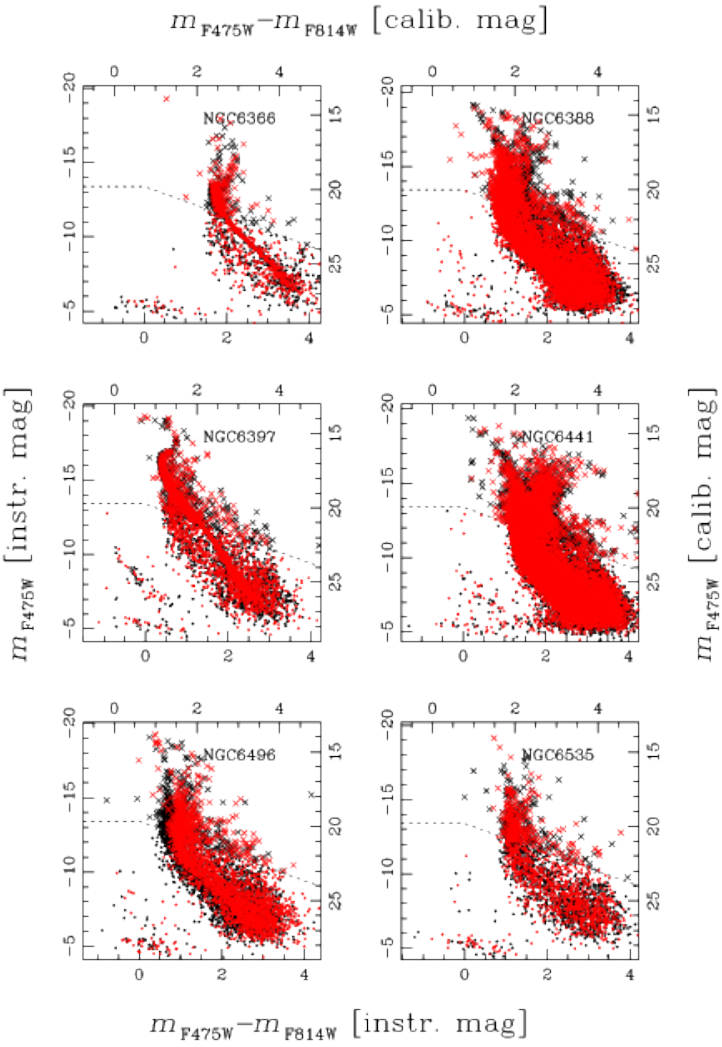

Figure 4.20: As in Figure 4.16 but for NGC 6366, NGC 6388, NGC 6397, NGC 6441, NGC 6496 and NGC 6535

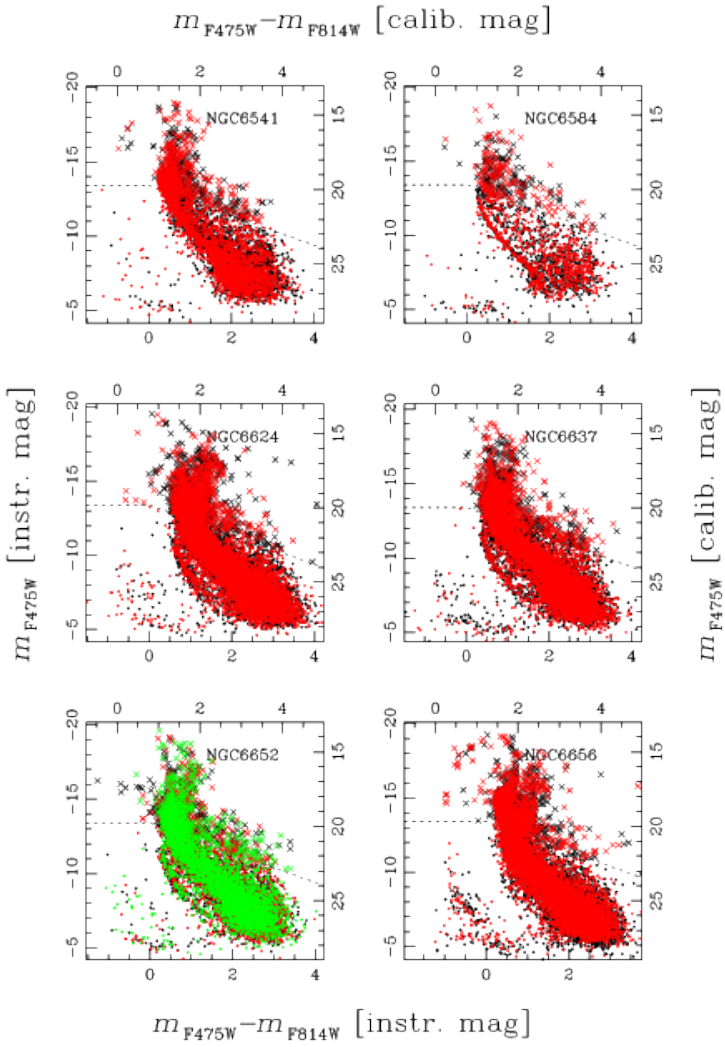

Figure 4.21: As in Figure 4.16 but for NGC 6541, NGC 6584, NGC 6624, NGC 6637, NGC 6652 and NGC 6656

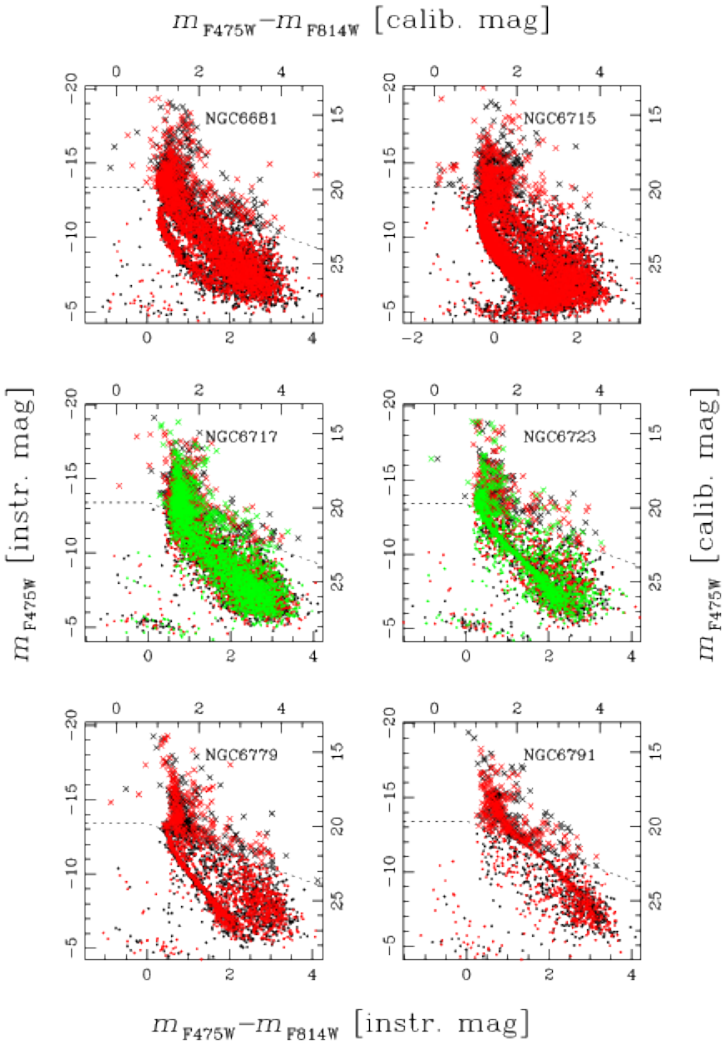

Figure 4.22: As in Figure 4.16 but for NGC 6681, NGC 6715, NGC 6717, NGC 6723, NGC 6779 and NGC 6791

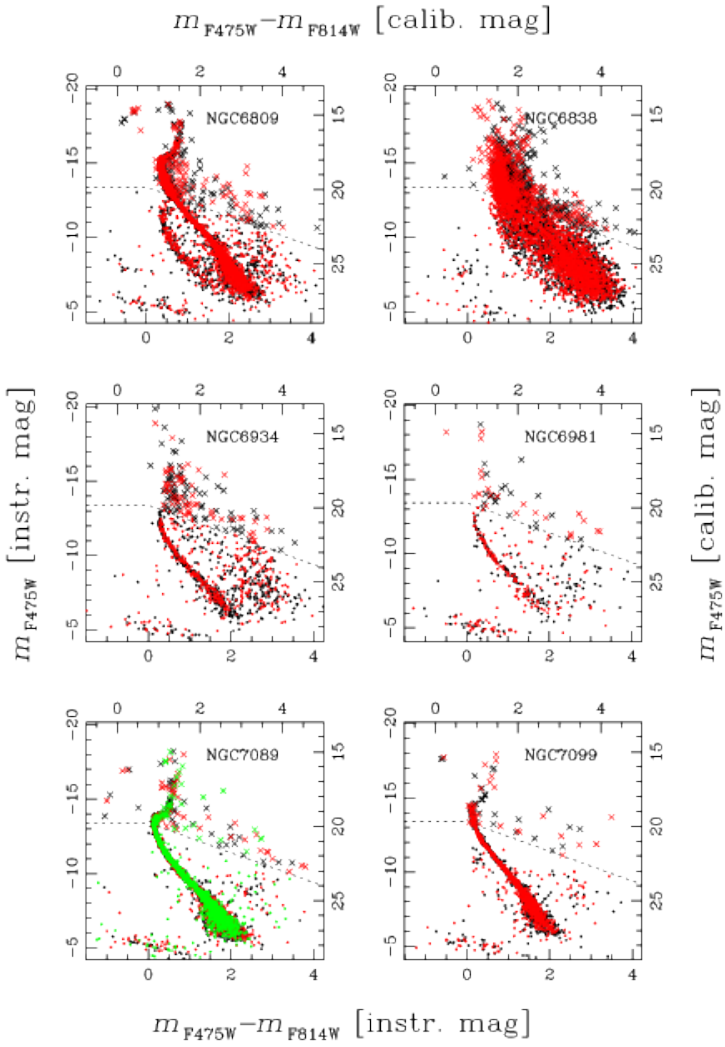

Figure 4.23: As in Figure 4.16 but for NGC 6809, NGC 6838, NGC 6934, NGC 6981, NGC 7089 and NGC 7099

5

The radial distribution of stellar populations in NGC 2808

The content of this chapter has been adapted from the work: The *Hubble Space Telescope* UV Legacy Survey of Galactic Globular Clusters. X. The radial distribution of stellar populations in NGC 2808. The article has been published in the peer-reviewed journal Monthly Notices of the Royal Astronomical Society (Simioni et al. 2016).

Abstract

Due to their extreme helium abundance, the multiple stellar populations of the globular cluster NGC 2808 have been widely investigated from a photometric, spectroscopic, and kinematic perspective. The most striking feature of the color-magnitude diagram of NGC 2808 is the triple main sequence (MS), with the red MS corresponding to a stellar population with primordial helium, and the middle and the blue MS being enhanced in helium up to Y ∼0.32 and ∼0.38, respectively. A recent study has revealed that this massive cluster hosts at least five distinct stellar populations (A, B, C, D, and E). Among them populations A, B, and C correspond to the red MS, while populations C and D are connected to the middle and the blue MS. In this paper we exploit *Hubble-Space-Telescope* photometry to investigate the radial distribution of the red, the middle and the blue MS from the cluster center out to about 8.5 arcmin. Our analysis shows that the radial distribution of each of the three MSs is different. In particular, as predicted from multiple-population formation models, both the blue MS and the middle MS appears to be more concentrated than the red MS with a significance level for this result wich is above 3σ.

5.1 Introduction

The massive globular cluster (GC) NGC 2808 is one of the most intriguing objects in the context of multiple stellar populations. The most astonishing feature of its color-magnitude diagram (CMD) is the presence of five distinct sequences of main-sequence (MS), and red-giant-branch (RGB) stars (Piotto et al. 2007; Milone et al. 2015b – hereafter Paper III –, Milone et al. 2012a –hereafter M12–) and at least four distinct horizontal-branch (HB) segments (Bedin et al. 2000).

Spectroscopy of bright RGB stars has revealed an extreme chemical composition with extended Na-O (Carretta et al. 2006; Gratton et al. 2013; Marino et al. 2014) and Mg-Al (Carretta 2014) anticorrelations.

The distinct sequences in the CMD of NGC 2808 correspond to multiple stellar populations with light element abundance variations and different helium content. In particular, the three most evident MSs discovered by Piotto et al. (2007), namely red, middle, and blue MS (rMS, mMS, and bMS) have been interpreted with three stellar populations with primordial helium abundance (Y∼0.25) and with extreme values of Y∼0.32, Y∼0.38 (D'Antona & Caloi 2004; D'Antona et al. 2005; Piotto et al. 2007; Paper III). Large helium enhancement have been also inferred from spectroscopy of HB stars (Marino et al. 2014) and by the analysis of chromospheric lines in spectra of RGB stars (Pasquini et al. 2011).

The formation and evolution of stellar populations in GCs have been widely investigated by several authors (see e.g. Renzini et al. 2015 and references therein). The fraction of stars in each population, their radial distribution, chemical composition, mass function and dynamics are amongst the diagnostics commonly used to constraint the various scenarios. In particular, the radial distribution of stellar populations can provide information on the series of events that led from massive clouds in the early Universe to the present day GCs with their multiple stellar populations. Indeed clusters with long relaxation times may still keep information of the initial conditions of their stellar populations.

Theoretical models and simulations by D'Ercole et al. (2008, 2010) predict that stars enhanced in helium and sodium are more centrally concentrated than stellar populations with primordial helium and oxygen abundance. This scenario is in agreement with observational studies on some GCs (e.g. 47Tuc and ωCen, Sollima et al. 2007, Bellini et al. 2009, Milone et al. 2012b, Cordero et al. 2014; M2, M3, M5, M13, M15, M53, M92, Lardo et al. 2011; NGC 362, Carretta et al. 2013; NGC 3201, Carretta et al. 2010c; NGC 2419, Beccari et al. 2013; NGC6388 and NGC6441, Bellini et al. 2013a) while in other cases the

multiple stellar populations share the same radial distribution (e.g. NGC 1851, NGC 6121 (M4), NGC 6362, and NGC 6752, see Milone et al. 2009b; Dalessandro et al. 2014; Nardiello et al. 2015).

In this paper we exploit proprietary data from the Wide Field Channel of the Advanced Camera for Surveys (WFC/ACS) and the Ultraviolet and Visual Channel of the Wide Field Camera III (UVIS/WFC3) to investigate for the first time the radial distribution of the multiple MSs in NGC 2808. We also show the results of a simple N-body simulations aimed at illustrating and providing some insight on the possible spatial mixing and dynamical history of this cluster. This paper is part of the *Hubble Space Telescope* (*HST*) UV Legacy Survey of Galactic Globular Clusters that is a project to investigate 57 Galactic Globular Clusters (GCs) through the filters F275W, F336W and F438W of UVIS/WFC3 (GO-13297, PI. G. Piotto, see Piotto et al. 2015 – hereafter Paper I – for details). The paper is organized as follows: In Sect. 5.2 we present the data and the data analysis; Sect. 5.3 describes in detail the methods used to derive the fraction of bMS, mMS, and rMS stars and the simulation performed for the theoretical analysis. Results are then presented in Sect. 5.4, and discussed in Sect. 5.5.

5.2 Data and data analysis

In order to study the radial distribution of the multiple MSs and RGBs of NGC 2808 we have exploited the dataset listed in Tab. 5.1 which consists of images taken with ACS/WFC and UVIS/WFC3 on board of *HST*. These data are part of GO-9899, GO-10922, GO-12605 (PI. G. Piotto) and GO-10775 (PI. A. Sarajedini) and most of them have been already used by our group to study multiple stellar populations in this clusters (e.g. Piotto et al. 2007, Paper I; Sarajedini et al. 2007; Anderson et al. 2008a; M12).

The footprints of the data are shown in Fig. 5.1 where we indicate with different color codes the images from different GOs. Stars in the most external field have radial distance of Δr$\sim$8.5 arcmin at most and lie approximately halfway from the tidal radius of NGC 2808 which is $r_t = 9.08$ arcmin (Harris 1996, 2010 edition).

We have used the photometric and astrometric catalogs presented by M12 from the GO-9899 and GO-10922 dataset, and the catalog from Anderson et al. (2008a) for GO-10775. The photometric and astrometric reduction for GO-12605 data has been carried out as described below.

We have first corrected the charge-transfer efficiency (CTE) effects in each image by using the method and the software by Anderson & Bedin (2010).

Photometry and astrometry of ACS/WFC images has been performed as in Anderson et al. (2008a). Briefly, we have used two distinct methods to

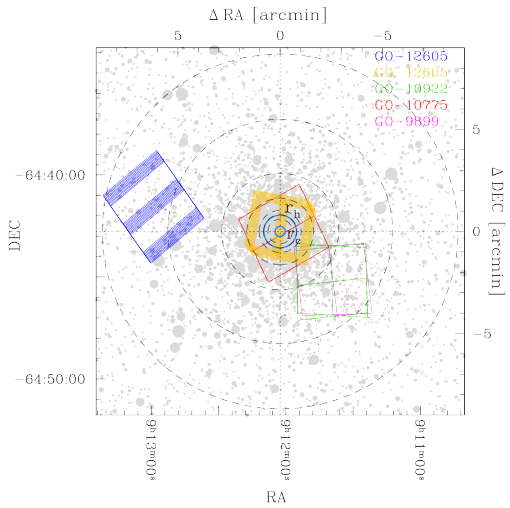

Figure 5.1: Finding chart for the used images. Core and half-light radii of NGC 2808 ($r_c = 0.25$ arcmin and $r_h = 0.80$ arcmin, Harris 1996, 2010 edition) are indicated by cyan circles. For each used set the corresponding footprints are shown: red dotted fields corresponds to WFC3 IR observations of GO-11665. Dashed circles represents the boudaries of the selected radial bins; see text for details.

measure bright and faint stars. To determine flux and position of bright stars we have analyzed each image, independently, by using the point-spread function models from Anderson & King (2006) plus a spatially constant perturbation that accounts for small focus variations due to the 'breathing' of *HST*. The derived magnitudes and positions are then combined. The flux and the position for very faint stars, which can not be robustly measured in every individual image, have been determined by fitting for each star simultaneously all the pixels in all the exposures (see Section 5 of Anderson et al. 2008b for more details). Stellar positions have been corrected for geometrical distortion by using the solution provided by Anderson & King (2006). UVIS/WFC3 images have been analysed similarly. In this case, we derived the PSFs as in Anderson et al. (2006) and Bellini et al. (2010) and used distortion solution by Bellini & Bedin (2009) and Bellini et al. (2011).

We have used the several indexes provided by the software as diagnostics of the quality of photometry (Anderson et al. 2008a). Since high-accuracy photometry is required to analyse the multiple MSs and RGBs in NGC 2808, we have adopted the method described by Milone et al. (2009a) and Bedin et al. (2009) to select a sub-sample of stars that have small astrometric errors, are relatively isolated, and well fitted by the PSF as in Milone et al. (2009a) (Sect. 2.1).

Photometry has been calibrated as in Bedin et al. (2005). For the WFC/ACS images, we used the zero points provided by Bedin and collaborators, while for UVIS/WFC3 we adopted the zero points listed in the STScI web page for WFC/ACS and WFC3/UVIS[1]. Each CMD has been corrected for differential reddening as in M12.

The CMDs used to study the radial gradient of multiple populations in NGC 2808 are shown in Fig. 5.2. For the central and middle field where stellar proper motions were available from Piotto et al. (2007) and Paper III we analyzed only stars that, according to their motion are cluster members (see Piotto et al. 2007 for details). On the contrary, there are no proper motions for stars in the outer field and we will account for field-star contamination by using the Galactic model from Girardi et al. (2005) as discussed in Sect. 5.3. In the outer and middle field we have analyzed the $m_{\rm F814W}$ vs. $m_{\rm F475W} - m_{\rm F814W}$ CMD and studied multiple populations in the magnitude interval $19.50 < m_{\rm F814W} < 22.00$ where the three MSs are clearly visible. In the inner field we analyzed MS stars with $19.50 < m_{\rm F814W} < 21.25$ and limited our study to the region with distance from the cluster center, $R > 0.75$ arcmin, indeed crowding prevents us to clearly distinguish the triple MS at smaller radii. In this case we used the

[1] http://www.stsci.edu/hst/wfc3/phot_zp_lbn, http://www.stsci.edu/hst/acs/analysis/zeropoints/zpt.py

Table 5.1: List of the used *HST* images. The average radial distance from the clusters center, R, is indicated for each field.

GO	PI	Camera	Filter	Exposures	R	Epoch
9899	G. Piotto	WFC/ACS	F475W	6×340s	3′.34	05 May 2004
10775	A. Sarajedini	WFC/ACS	F814W	23s+5×370s		01 Jan 2006
10922	G. Piotto	WFC/ACS	F475W	2×350s	3′.40	09 Aug 2006
				2×360s	3′.38	01 Nov 2006
			F814W	3×350s	3′.40	09 Aug 2006
				3×360s	3′.38	01 Nov 2006
12605	G. Piotto	WFC/ACS	F475W	6×890s+6×982 s	6′.27	08 Sept 2013
			F814W	6×508s	6′.27	08-9 Sp 2013
12605	G. Piotto	UVIS/WFC3	F275W	12×985s		08-09 Esp 2013

$m_{\rm F814W}$ vs. $m_{\rm F275W} - m_{\rm F814W}$ CMD. Furthermore, we analyze the radial distribution of multiple populations along the RGB in the entire inner field.

5.2.1 Artificial Stars

The artificial-star (AS) experiments have been performed as in Anderson et al. (2008a). We have generated a list of 300,000 stars and placed them along each MS and RGB of NGC 2808 by assuming the same spatial distribution as observed for real stars (see M12 for details).

For each star in the input list, we have generated, a star in each image, and measures it by using the same procedure as for real stars. We assumed an AS as found when the input and the output position differ by less then 0.5 pixel and the input and the output flux by less than 0.75 mag. Finally, we have selected a sub-sample of relatively isolated ASs with small astrometric errors, and well fitted by the PSF by using the same procedure as for real stars indeed the software by Anderson et al. (2008a) provides for ASs the same diagnostics of the photometric quality as for real star.

ASs have been used to estimate errors of the photometry used in this paper and the completeness level. Completeness have been derived for each star as in M12.

5.3 The fraction of stars in the three MSs

To compare the radial distribution of each stellar population and highlight the presence of gradients among them, the number of stars in each MS has been counted. These values have been thus normalized to the total number of MS stars observed in the analyzed magnitude ranges in order to obtain the so-called population ratio. To derive the number of stars in each MS ($N_{\rm bMS}$, $N_{\rm mMS}$, and $N_{\rm rMS}$) and the fraction of binaries ($f^{\rm BIN}$) in each field of NGC 2808 we adopted

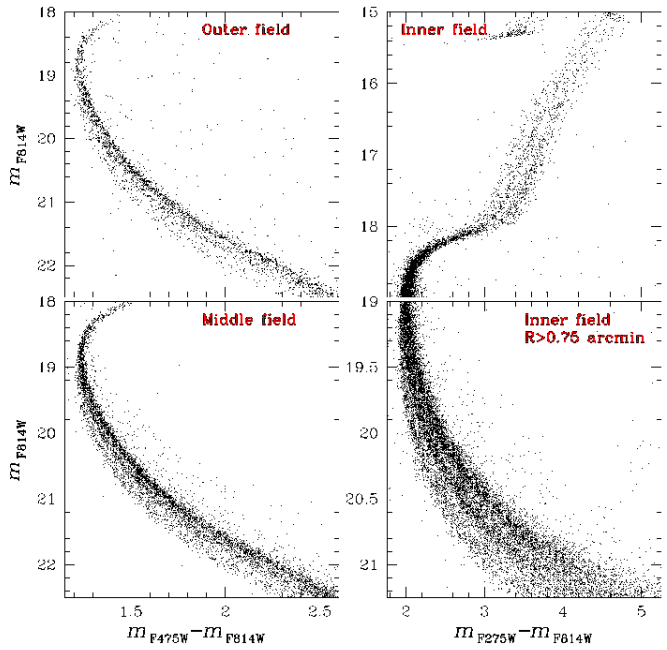

Figure 5.2: CMDs corrected for differential reddening used to determine the fraction of stars in the multiple MSs of NGC 2808 in the outer and middle field (left panels), and the fraction of multiple MSs and RGBs in the inner field (right panels).

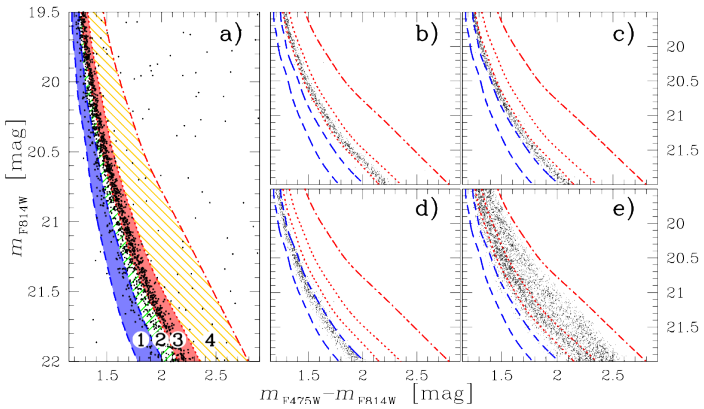

Figure 5.3: Method used to determine the fraction of bMS, mMS and rMS stars and the fraction of binaries from GO-12625 ACS/WFC data. Blue-dashed and red-dotted lines have been obtained by shifting the fiducials of the bMS and the rMS by $\pm 3\,\sigma_{\rm bMS}$ and $\pm 3\,\sigma_{\rm rMS}$, respectively. The red dashed-dotted line plotted in each panel is the fiducial line of equal-mass binaries red-shifted by $3\,\sigma_{\rm rMS}$. These lines are the boundaries of four regions, R_1–R_4 of the CMD colored blue, green, red, and yellow, respectively in panel a). The observed CMD for NGC 2808 stars is plotted in panel a), while panels b), c), and d) show the simulated CMD for single rMS, mMS, and bMS stars, respectively. The CMD of panel e) is made only of MS-MS binaries (see text for details).

the iterative procedure introduced by M12 and illustrated in Fig. 5.3 for the CMD of the outer field. The blue dashed lines and the red dotted lines plotted in each panel of Fig. 5.3 are obtained by shifting by plus or minus $3\,\sigma_{\rm bMS}$ and $3\,\sigma_{\rm rMS}$ the fiducial line of the red and the blue MS, respectively. The red dashed-dotted line is the fiducial line of equal mass rMS-rMS binaries red-shifted by $3\,\sigma_{\rm rMS}$. The fiducials and the corresponding errors have been determined as in M12.

These lines are the boundaries of four regions that we name R_1, R_2, R_3, and R_4 and colored blue, green, red, and yellow, respectively. The majority of the bMS, mMS, and rMS stars are located in the regions R_1, R_2, and R_3, while the region R_4 is mostly populated by MS-MS binaries. As discussed by M12, a fraction of bMS also migrates into regions $R_{2,3,4}$, and similar shift applies to some mMS and rMS stars. Moreover regions R_1, R_2, R_3 are also populated by MS-MS binaries.

Specifically, each region $R_{\rm i}$ is populated by a fraction $f_{\rm i}^{\rm bMS(mMS,rMS)}$ of bMS

(mMS, rMS) stars and a fraction $f_{\rm i}^{\rm BIN}$ of binaries. The relations between the observed total numbers of stars and the number of stars in each sequence can be expressed, for i=1,2,3,4 as:

$$N_{\rm i} = N_{\rm bMS} f_{\rm i}^{\rm bMS} + N_{\rm mMS} f_{\rm i}^{\rm mMS} + N_{\rm rMS} f_{\rm i}^{\rm rMS} + f^{\rm BIN} N_{\rm MS} f_{\rm i}^{\rm BIN} \quad (5.1)$$

where $N_{\rm MS}$ is the total number of MS stars. $N_{\rm i}$ is the number of cluster stars in each region corrected for completeness. In the inner and middle field, where stellar proper motions are available, we have determined $N_{\rm i}$ from counts of stars that, according to their proper motions, are cluster members. In the outer field, where we do not have proper motions, we have used the Galactic model by Girardi et al. (2005) and estimated the number of cluster stars in each region as $N_{\rm i} = N_{\rm i}^{\rm obs} - N_{\rm i}^{\rm field}$, where $N_{\rm i}^{\rm obs}$ is the number of stars observed in each region and corrected for completess, and $N_{\rm i}^{\rm field}$ is the number of field stars predicted by the Galactic model in the same direction of NGC 2808 and in a field of view with the same area as the outer field.

Since the number of binaries strongly depends on the number of stars in each sequence, and vice versa, in order to derive the unknowns of Eq. 5.1 we applied an iterative procedure. We started by assuming a null binary fraction and determine a crude estimate of $N_{\rm bMS}$, $N_{\rm mMS}$, and $N_{\rm rMS}$ by solving the system of Eq. 5.1 for i=1,2,3.

These numbers have been then used to determine $f_{\rm i}^{\rm BIN}$. To do this we have generated a CMD made of pure binaries as in M12 by using a flat mass-ratio distribution and assuming that the binary components belong to any of the MSs. The fraction of binaries, $f_{\rm i}^{\rm bMS(mMS,rMS)}$, in each region $R_{\rm i}$, has been determined by computing the ratio between the total number of inserted binaries and the number of binaries in each region. We refer the reader to M12 (see their Sect. 5.2 and 5.3) for details.

At this stage, we have obtained a raw estimate of $f_{\rm i}^{\rm BIN}$ and calculated $f_{\rm i}^{\rm bMS}$, $f_{\rm i}^{\rm mMS}$, and $f_{\rm i}^{\rm rMS}$. So we can derive $f^{\rm BIN}$ from Eq. 5.1. This ends one iteration.

The values of $N_{\rm bMS}$, $N_{\rm mMS}$, $N_{\rm rMS}$ and $f^{\rm BIN}$ are used to simulate a new CMD, improve the estimate of $f_{\rm i}^{\rm BIN}$, and again solve the system of Eq. 5.1 for $N_{\rm bMS}$, $N_{\rm mMS}$, $N_{\rm rMS}$, and $f^{\rm BIN}$. Following M12, we iteratively repeated the procedure until the value $f^{\rm BIN}$ changes by less than 0.001 from one iteration to the successive one.

Each measure is affected by the uncertainties in the determination of the fiducial line and on the corresponding boundaries of the CMD regions $R_1 - R_4$. In order to determine it, we have repeated the procedure described above 1,000 times each time by using different fiducials and the boundaries of the four

regions, thus determining 1,000 values for the population ratio. Each fiducial has been determined by adding to each point of the fiducial a shift in color, whose value is randomly extracted by a Gaussian distribution with a σ equal to the observed error. We assumed as the uncertainties in the determination of the fiducial line the $68^{\rm th}$ percentile of the 1,000 determination of the population ratio. This uncertainty has been then added in quadrature to the Poisson uncertainty to determine the error associated to each measure.

In the central field, the three MSs are not distinguishable below $m_{\rm F814W} = 21.25$ so we limited the analysis to the F814W magnitude range $[19.5 - 21.25]$. In both the outer and middle field, where deep F475W and F814W photometry is available, we have analyzed the interval with $19.5 < m_{\rm F814W} < 22.0$ in close analogy with M12. In order to compare results from different fields in the outer and middle field we also provide results for the interval $[19.5 - 21.25]$.

Table 5.2: Fraction of stars in the three main stellar populations of NGC 2808 derived from multiple MSs and RGBs in the three fields analyzed in this paper. The magnitude interval is also listed. The fraction of rMS, mMS, and bMS stars determined as described in Sect. 5.3 and the fraction of stars of RGB-(A+B+C), RGB-D, and RGB-E from Paper III are listed in the six upper lines of the table. The corresponding fraction of RGB stars inferred from method I are provided at line seven. The last four lines of the table list the population ratios derived from method II. See text for details.

field	sequence	m_{F814W} interval	population ratio rMS or RGB-(A+B+C)	population ratio mMS or RGB-D	population ratio bMS or RGB-E	binary fraction
outer	MS	19.50-21.25	0.63±0.04	0.27±0.04	0.10±0.03	0.03±0.01
		19.50-22.00	0.62±0.04	0.27±0.04	0.11±0.03	0.03±0.01
middle	MS	19.50-21.25	0.62±0.02	0.25±0.02	0.13±0.03	0.05±0.01
		19.50-22.00	0.62±0.02	0.24±0.02	0.14±0.03	0.05±0.01
inner, R>0.75 arcmin	MS	19.50-21.25	0.53±0.02	0.29±0.02	0.18±0.02	0.06±0.01
inner	RGB	12.40-17.20	0.50±0.03	0.31±0.02	0.19±0.02	–
inner	RGB	17.20-12.40	0.52±0.03	0.28±0.02	0.20±0.02	–
outer	MS	19.50-22.00	0.57±0.04	0.30±0.04	0.13±0.03	–
middle	MS	19.50-22.00	0.57±0.02	0.27±0.02	0.16±0.03	–
inner, R>0.75 arcmin	MS	19.50-21.25	0.47±0.02	0.32±0.02	0.21±0.02	–
inner	RGB	12.40-17.20	0.46±0.02	0.33±0.01	0.21±0.01	–

Table 5.3: Stellar masses for the three main populations of NGC 2808 at different luminosities in the F814W band as inferred from BaSTI isochrones.

$m_{\rm F814W}$ [mag]	$M_{\rm rMS}$ [$M_\odot$]	$M_{\rm mMS}$ [$M_\odot$]	$M_{\rm bMS}$ [$M_\odot$]
12.40	0.856	0.739	0.654
17.70	0.847	0.732	0.648
19.50	0.769	0.679	0.610
21.25	0.600	0.537	0.491
22.00	0.529	0.476	0.435

5.4 Results

The obtained fractions of bMS, mMS and rMS stars and the fraction of binaries in each field are listed in Tab. 5.2. In the first two rows we have listed results corresponding to the F814W magnitude bin [19.5 − 21.25], while in Fig. 5.4 we plotted the fraction of b(m,r)MS-stars as a function of the average radial distance from the cluster center of all the analyzed stars.

Unfortunately, as discussed in Sect. 5.2, due to stellar crowding, the triple MS is not clearly visibile in the very central regions of NGC 2808 and we have no information on the population ratio in the innermost 0.75 arcmin. In order to extend the study of the radial distribution of multiple stellar populations to the central regions, we have exploited the results from Paper III.

In that work, we have analyzed multi-wavelength photometry of NGC 2808 as part of the UV Legacy Survey of Galactic Globular Clusters from GO-13297 and GO-10775. We have separated at least five distinct populations that we name A, B, C, D and E. The five populations are clearly visible along the RGB in the entire analyzed field of view, which corresponds to the inner field analyzed in this paper. Specifically, populations D and E correspond to the mMS and the bMS identified by Piotto et al. (2007), while populations A, B, and C are associated to the rMS. The fraction of stars in the five RGBs are $f^{\rm RGB-A}$=5.8±0.5%, $f^{\rm RGB-B}$=17.4±0.9%, $f^{\rm RGB-C}$26.4±1.2%, $f^{\rm RGB-D}$=31.3±1.3%, and $f^{\rm RGB-E}$=19.1±1.0% of the total number of RGB stars with $12.25 < m_{\rm F814W} < 17.70$, respectively. Therefore the progeny of the rMS, which corresponds to the RGBs A, B, and C include $f^{\rm RGB-(A+B+C)}$=49.6±1.6% of the total number of MS stars. The interval of luminosity analyzed in Paper III for the study of multiple RGBs obviously differs from that of this paper. In order to properly compare RGB and MS stars we have adopted two different methods.

5.4.1 Crude estimate (Method I)

The first method is based on the comparison of results from multiple MS corresponding to the F814W magnitude bin [19.5 − 21.25] and from the RGB. Specifically, we have first derived the population ratios from four distinct sample of stars that include MS stars of the inner, middle, and outer field and RGB stars of the inner field.

To compare results from the RGB and the MS, we used the photometric catalog from Paper III and estimated the fraction of RGB-E, RGB-D and RGB-(A+B+C) as done in that paper but for stars with radial distance from the cluster center larger than 0.75 arcmin. This is the same region of the inner field where we have determined the fraction of bMS, mMS, and rMS stars.

We found that the fraction of RGB-(A+B+C), RGB-D and RGB-E stars are $f^{\rm RGB-(A+B+C)}_{\rm inner-field,R>0.75'} = 0.51\pm0.03$, $f^{\rm RGB-D}_{\rm inner-field,R>0.75'} = 0.32\pm0.02$, $f^{\rm RGB-E}_{\rm inner-field,R>0.75'} = 0.17\pm0.02$. For completeness, we derived the population ratio for stars with radial distance from the cluster center R<0.75 arcmin. We find $f^{\rm RGB-(A+B+C)}_{\rm inner-field,R<0.75'} = 0.49\pm0.03$, $f^{\rm RGB-D}_{\rm inner-field,R<0.75'} = 0.30\pm0.02$, $f^{\rm RGB-E}_{\rm inner-field,R>0.75'} = 0.21\pm0.03$ and conclude that there is no evidence for significant difference in the population ratio derived within the region with radial distance $0'.00$ <R< $0'.75$ and the region with $0'.75$ <R< $2'.10$.

We thus imposed the same fraction of stars along the three MSs and the corresponding RGBs in the region of the inner field with R>0.75 arcmin and calculated the number of RGB-(A+B+C) stars as:
$N^{\rm RGB-(A+B+C)}_{\rm inner-field} = N^{\rm RGB-(A+B+C)} \frac{f^{\rm rMS}_{\rm inner-field}}{f^{\rm RGB-(A+B+C)}_{\rm inner-field,R>0.75'}}$.
We derived $N^{\rm RGB-D(E)}_{\rm inner-field}$ similarly. Results are listed in Tab. 5.2 and illustrated in the upper-left panel of Fig. 5.4.

The fraction of stars in each sequence in the middle and the outer field agree within $1\,\sigma$, where approximately 63% of the entire number of the analyzed MS stars in the F814W magnitude interval [19.5 − 21.25] belong to the rMS. The fraction of rMS stars slightly decreases in the central field to about 53%, where it is similar to the fraction of RGB-(A+B+C). The difference between the fraction of rMS stars in the inner and in the outer field is significant at the $2.5\,\sigma$-level and similar results are obtained when we compare results from the RGB in the inner field with those from the MS in the outer and middle fields.

In contrast, the fraction of mMS- plus bMS-stars seems to increase when moving from the cluster outskirts to the center, and both the blue and the middle MS are more centrally concentrated than the rMS. We note, that one of the main disadvantages of the analysis illustrated in the upper-left panel

of Fig. 5.4 is that, in some cases, distinct fields cover the same radial interval and the large size of each bin has the effect of diluting and hiding in part any existing radial gradient. In order to further explore the radial distribution of the multiple stellar populations in NGC 2808 and better identify the presence and strength of radial gradients, it is necessary to use a finer and non-overlapping binning.

In order to further investigate the radial distribution of multiple stellar populations in NGC 2808 we have divided the stars studied in this paper into seven groups with different radial distance from the cluster center and calculated the population ratio in each region. Specifically, we have defined a circle with radius R= 0.60 arcmin where photometry of RGB stars only is available and three additional regions included in the inner field such that, each region contains the same number of MS stars. Moreover, we have defined three additional annuli that include stars in the middle and the outer field. The boundaries of these seven regions are plotted with dotted circles in Fig. 5.1. We have verified that the conclusion of the paper do not depend either on the location or on the number of regions that we use to study the radial distribution of multiple stellar populations.

Results are listed in Table 5.4 and illustrated in the upper-right panel of Fig. 5.4, where the continuous lines are the best-fit weighted-least-squares straight lines. The values of the slope a and the intercept b of each line are listed in Table 5.5 together with the correspoding uncertainties.

The slope corresponding to the red MS is larger than zero with a significance greater than $6\,\sigma$, while both the blue and the middle exhibit negative values of a with a significance of $\sim 6.5\,\sigma$ and $\sim 1.5\,\sigma$, respectively. By assuming a flat distribution, and the same uncertainties as in our population-ratio estimates, 10^6 Monte Carlo simulations indicate we have a probability of 2×10^{-4} to get a slope equal to or higher than that observed for red MS stars. In the case of the bMS, the probability that the observed gradient is due to measurement errors is 4×10^{-3}.

Comparing red, middle and blue MS, it can be noted that the bMS appears to be the most concentrated, having the minimum slope value among them. The difference between the slopes associated to rMS and bMS results to be significant at 12σ. The mMS is also more concentrated than the rMS with a difference between the two slopes that is significant at $\sim 7\sigma$.

Table 5.4: Population ratios measured in the redefined radial sampling (see text for details); R_{min}, R_{max}, and R_{med} are respectively the minimum,maximum and median radial distances of the bin. The first lines ar referred to Method I while the lower part is referred to Method II.

R_{min} [arcmin]	R_{max} [arcmin]	R_{med} [arcmin]	Population ratio rMS	Poputon ratio mMS	Population ratio bMS	Population ratio mMS+bMS
0.00	0.60	0.28	0.49 ± 0.03	0.30 ± 0.02	0.21 ± 0.03	0.51 ± 0.036
0.60	0.82	0.71	0.49 ± 0.02	0.32 ± 0.02	0.19 ± 0.02	0.51 ± 0.028
0.82	1.03	0.92	0.52 ± 0.02	0.29 ± 0.02	0.19 ± 0.02	0.48 ± 0.028
1.03	1.63	1.19	0.51 ± 0.02	0.31 ± 0.02	0.17 ± 0.02	0.48 ± 0.028
1.63	2.84	2.25	0.565 ± 0.038	0.294 ± 0.029	0.142 ± 0.034	0.436 ± 0.045
2.86	5.49	3.70	0.593 ± 0.034	0.285 ± 0.033	0.122 ± 0.041	0.407 ± 0.053
5.50	8.70	6.44	0.634 ± 0.053	0.272 ± 0.049	0.094 ± 0.047	0.366 ± 0.068
0.00	0.60	0.28	0.45 ± 0.03	0.32 ± 0.02	0.23 ± 0.03	0.55 ± 0.036
0.60	0.82	0.71	0.45 ± 0.02	0.34 ± 0.02	0.21 ± 0.02	0.55 ± 0.028
0.82	1.03	0.92	0.50 ± 0.02	0.28 ± 0.02	0.22 ± 0.02	0.50 ± 0.028
1.03	1.63	1.19	0.48 ± 0.02	0.32 ± 0.02	0.20 ± 0.02	0.52 ± 0.028
1.63	2.84	2.25	0.548 ± 0.038	0.284 ± 0.029	0.168 ± 0.034	0.452 ± 0.045
2.86	5.49	3.70	0.576 ± 0.034	0.270 ± 0.033	0.154 ± 0.041	0.424 ± 0.053
5.50	8.70	6.44	0.616 ± 0.053	0.271 ± 0.049	0.113 ± 0.047	0.384 ± 0.068

Table 5.5: Slope and intercept values (a and b respectively), together with their uncertainties (σ_a and σ_b), of best-fit least-squares lines for rMS, mMS, bMS and mMS+bMS respectively, referrend to Method I; see text for details.

sequence	a	σ_a	b	σ_b
rMS	0.027	0.004	0.483	0.007
mMS	−0.006	0.003	0.309	0.007
bMS	−0.020	0.003	0.202	0.006
mMS+bMS	−0.027	0.004	0.517	0.007

5.4.2 A more sophisticated estimate (Method II)

As a second method to compare results from the RGB and from the MS we follow the receipe by Milone et al. (2009b) in their study of the radial distribution of stellar populations along the SGB of NGC 1851. Sure enough, stars in different intervals of luminosity (like the sample of RGB and MS stars analyzed in this paper) have different masses; moreover, stars with different luminosity but different helium abundance have different masses. This second method takes in account this mass difference in order to properly compare the population ratio inferred from the MS and the RGBs. We have to compensate for the fact that the two stellar groups that define the distinct MSs and RGBs span different mass intervals.

This method allows us to fully exploit information from the entire magnitude interval with $19.5 < m_{\rm F814W} < 22.0$ in the middle and outer field. We have normalized the number of stars in each sequence to the analyzed mass interval as:
$N_{\rm b(m,r)MS}/\Delta\mathcal{M}$ where $\Delta\mathcal{M} = \int_{M1,\rm b(m,r)MS}^{M2,\rm b(m,r)MS} \phi(\mathcal{M})d\mathcal{M}$.
Here, $\phi(\mathcal{M})$ is the adopted mass function, and $M1, \rm b(m,r)MS$ and $M2, \rm b(m,r)MS$ are the minimum and the maximum stellar mass in the analyzed interval of luminosity. We adopted a similar relation to derive the the normalized fraction of stars in the RGB-(A+B+C), RGB-D, and RGB-E.

The masses corresponding to different luminosities are listed in Tab. 5.3 and are obtained from BaSTI isochrones (Pietrinferni et al. 2004, 2009) by adopting the same values of distance modulus, reddening, age, metallicity and helium abundance as in M12. We adopted for the mass function $\phi(\mathcal{M})=M^{\alpha}$, where we used the values of α derived by M12. Results are listed in Tab. 5.2 and shown in the lower panels of Fig. 5.4.

In the lower-left panel we have considered each field separately. We confirm results obtained by using the method I, with the population corresponding to the rMS, being less centrally concentrated than the stellar populations of NGC 2808 that are highly helium enhanced. In this case the difference between

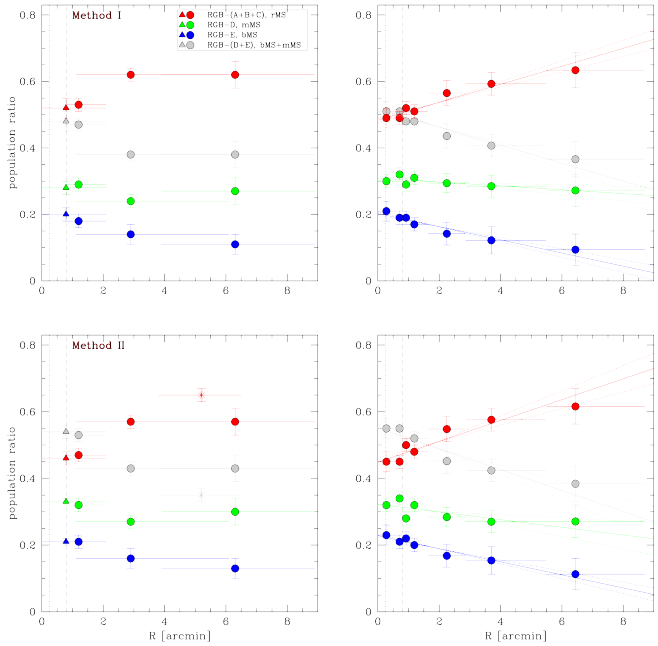

Figure 5.4: Fraction of bMS (blue symbols), mMS (green symbols), rMS (red symbols) and bMS+mMS (gray symbols) stars respect to the total number of MS stars as a function of the radial distance from the cluster center. The triangles used in the left panels indicate the values of population ratios inferred from RGB stars, while the squares refer to results from the MS. The red and gray asterisks plotted in the lower-left panel indicate the population ratio inferred by Milone et al. (2012d) in their study of low-mass MS stars. The horizontal lines plotted in each panel span the radial covarage of each bin, while the squares and the triangles indicate the average radial distance of the stars in each region. The vertical dotted and dashed lines mark the core and the half-light radius, respectively. Upper and lower panels show results obtained from method I and method II, respectively. In the upper-left and lower-left panel we have analyzed each field independently, while the upper-right and lower-right panel show the results for seven region with different distance from the cluster center. The best-fit straight lines are shown in the right panels, where dotted lines represent the maximum- and minimum-slope straight lines.

Table 5.6: Slope and intercept values (a and b respectively), together with their uncertainties (σ_a and σ_b), of best-fit least-squares lines for rMS, mMS, bMS and mMS+bMS respectively, referrend to Method II; see text for details.

sequence	a	σ_a	b	σ_b
rMS	0.031	0.006	0.449	0.012
mMS	−0.011	0.007	0.322	0.013
bMS	−0.020	0.003	0.228	0.005
mMS+bMS	−0.031	0.006	0.551	0.012

the fraction of RGB-(A+B+C) stars derived in the central field (∼57%) and the fraction of rMS in the middle and the outer fields (∼46-47%) is significant at the $\sim 4.0\,\sigma$ and $\sim 2.5\,\sigma$ level, respectively.

A recent study, based on images taken with the near-infrared (NIR) channel of WFC3 for stars in three fields have investigated multiple sequences of very low mass stars in NGC 2808. The three analyzed NIR/WFC3 fields have all radial distance of ∼5.2 arcmin from the center of NGC 2808 (Milone et al. 2012d; red dotted fields in Fig. 5.1). Two MSs are clearly visible in the magnitude interval with $< 21.25 < m_{\rm F160W} < 22.50$. The most-populous ones, contains 65±2% of the total number of analyzed stars and corresponds to the red MS, while the remaining 35±2% the sequence associated to the blue and the middle MS. The population ratios derived by Milone et al. (2012) and normalized to the corresponding mass intervals are in agreement with the results from this paper and are represented with red and grey asterisks in the lower-left panel of Fig. 5.4.

In the lower-right panel of Fig. 5.4 we show the results for the seven regions with different radial coverage, in close analogy with what we have done in the upper-right panel. The slopes corresponding to the three sequences are listed in Table 5.6 and confirm the conclusion of Sect. 5.4.1. In this case Monte Carlo simulations provide a probability smaller than 1×10^{-4} to get a slope equal to or higher than that observed for red MS stars, while the probability that the observed gradient for bMS stars is due to measurement errors is 3×10^{-3}. The difference between mMS and rMS slopes is now significant at $\sim 5\sigma$ while the significance level of the difference between bMS and rMS slopes is $\sim 7\sigma$.

5.4.3 Theoretical interpretation

The results of our observational analysis show that two helium enhanced populations (bMS and mMS) are more centrally concentrated than the rMS population. This result is in general qualitative agreement with the predictions of multiple-population cluster formation models according to which second-

generation (2G) stars should form more concentrated than the initial first-generation (1G) population.

Because of the effects of dynamical evolution on the structural properties of the various stellar populations, a direct connection between the current observed properties and those predicted by cluster formation models is not straightforward. The long-term cluster dynamical evolution will gradually weaken the initial radial gradient in the fraction of 2G stars (see e.g. Vesperini et al. 2013) until complete spatial mixing when no memory of the initial differences is preserved and all the populations share the same spatial distribution.

As discussed in the Intoduction, a few observational studies have found clusters still retaining memory of the initial differences in the spatial distribution of 1G and 2G populations while others appear to have reached the phase when different populations are completely mixed. For those clusters for which a radial gradient in the fraction of 2G stars is still present, the strength of the current observed radial gradient provides a lower limit on what must have been a stronger initial gradient.

A complete and detailed model for any specific individual cluster is a very challenging and computationally expensive task (see e.g. Giersz & Heggie 2011, Heggie 2014); the presence of multiple populations with the additional complexities related to their formation and dynamical history further complicates this task. This is well beyond the scope of the goals of this paper and is deferred to future investigations. Here, in order to illustrate the process of spatial mixing of multiple stellar populations and provide some initial insight on the possible dynamical history leading to the gradient found in our analysis we present the results of a simple N-body simulation focussing our attention on the two-body relaxation-driven long-term evolution of the spatial distributions of the 1G and 2G population. We started our simulation with 50000 particles with the 1G and the 2G populations each having half of the total mass of the system and a range of stellar masses equal to those expected at about 12 Gyr for a system with a Kroupa (2001) stellar IMF. Both populations are characterized by a King (1966) density profile with central dimensionless potential $W_0 = 7$ but the 2G population is initially concentrated in the inner regions of the cluster and has a half-mass radius about 4.5 times smaller than that of the 1G population. The simulation was run on the Big Red II supercomputer at Indiana University with the GPU-accelerated version of the NBODY6 code (Aarseth 2003, Nitadori & Aarseth 2012).

The cluster is initially tidally limited and assumed to be on a circular orbit in the external potential of a host galaxy modeled as a point mass. We focus here solely on the long-term evolution driven by two-body relaxation and its effect on the spatial distributions of the two populations (see also Vesperini

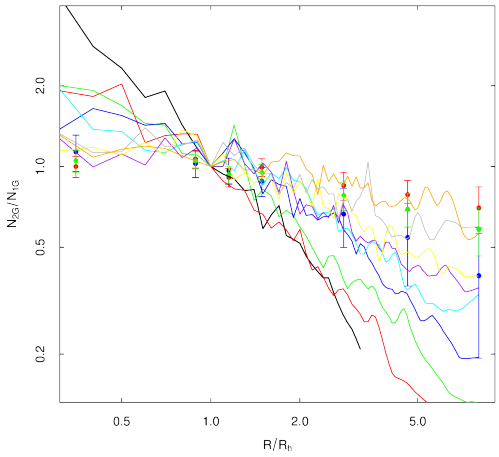

Figure 5.5: Time evolution of the radial profile of the ratio of the number of 2G to 1G stars (normalized to the value measured at the half-mass radius) versus the projetced distance from the cluster center (normalized to the half-mass radius) for the simulation discussed in the paper (see Section 5.4.3). Different curves correspond to the profiles measured at values of $t/t_{\rm rh}(t)$ equal to about 0.0 (black line), 2.0 (red line), 3.0 (green line), 5.0 (blue line), 7.0 (cyan line), 8.5 (purple line), 10.3 (yellow line),12.5 (grey line), 15.3 (orange line). Each radial profile has been calculated by using nine snapshots around the indicated time. Points with error bars show the observed ratio of the number of bMS to rMS stars (blue points), mMS stars to rMS stars (red points) and (bMS+mMS) to rMS stars (green points).

et al. 2013 for further discussion on the long-term evolution and dynamics of spatial mixing).

In Fig. 5.5 we show the time evolution of the radial profile of the ratio of the number of 2G to 1G stars for stars with masses between 0.6 and 0.8 $M_{\odot}$ along with the observed ratios for $N_{\rm bMS}/N_{\rm rMS}$, $N_{\rm mMS}/N_{\rm rMS}$ and $N_{\rm bMS+mMS}/N_{\rm rMS}$. The results of the simulations illustrate the progressive weakening of the initial radial gradient. In particular, the radial gradient in the fraction of bMS and mMS stars currently observed in NGC 2808 is approximately consistent with those found in the simulation at times $t/t_{rh}(t) \geq 7$. This figures shows a possible dynamical path and the significantly stronger initial gradient behind the current structural properties of the multiple populations of NGC 2808.

As already discussed in the Introduction, NGC 2808 is a particularly complex cluster; the early dynamics during the sequence of events that led to the formation of the different populations observed in this cluster are still unclear. A more detailed exploration of the possible differences in the early and long-term dynamical evolution of different populations and the implications for the current observed properties will require a much more extensive study than that presented here.

5.5 Summary and Conclusions

NGC 2808 is one of the most-massive GCs in the Galaxy and hosts at least five distinct stellar populations, namely A, B, C, D, and E, with different content of helium and light elements (Paper III). Populations D and E are highly enhanced in helium up to Y ∼0.32 and ∼0.38 and correspond to the mMS and the bMS discovered by Piotto et al. (2007). Populations A, B, and C are connected with the red MS by Piotto et al. (2007) and have almost primordial helium abundance. In this paper we have used both archive and proprietary data collected with the ACS/WFC and WFC3/UVIS on board of *HST* to investigate the radial distribution of the three main populations of NGC 2808 which correspond to the bMS, the mMS, and the rMS. Our dataset includes three fields spanning a radial interval that ranges from the cluster center to approximately 8.5 arcmin.

Parallel ACS@HST observations taken as part of GO-12605 are presented here for the first time (see upper-left panel of Fig. 5.2 for the obtained CMD). The three MSs have been detected in all the analyzed fields. The fraction of stars in each main sequence has been determined starting from a radial distance of 0.75 arcmin from the cluster center to 8.5 arcmin. At radial distance smaller than 0.75 arcmin, the three MS can not be clearly distinguished due to stellar crowding. We have used the photometry of RGB stars from Paper III to extend the study of multiple stellar populations to the cluster center. Using two different methods, we found that the populations which correspond to the rMS are less centrally concentrated than the helium rich stellar populations, with a significance for the result that is higher than 3σ. We have also presented the results of a simple N-body simulation illustrating the possible evolution of the multiple population spatial mixing of this cluster.

NGC 2808 has a very extended HB which is well populated on both sides of the RR Lyrae instability strip (Sosin et al. 1997). The red HB of NGC 2808 shares the same chemical composition as the stellar populations corresponding to the rMS stars (Gratton et al. 2013; Marino et al. 2014). The blue MS corre-

sponds to the bluest HB tail, while the remaining blue-HB stars are connected with the middle MS (e.g. D'Antona et al. 2005; Piotto et al. (2007); Dalessandro et al. 2011). Bedin et al. (2000) have investigated the radial distribution of the HB compontents and find no evidence for a significant gradient. Iannicola et al. (2009) further analyzed the radial distribution of HB stars in NGC 2808 and suggested that red-HB stars are less centrally concentrated than the remaining HB stars; although their conclusion is significant only at 1.5σ level, it suggests the presence of a gradient consistent with that we find in our analysis.

Recent studies have investigated the properties of the triple MS in NGC 2808, like the luminosity and mass function and the internal kinematics. M12 have studied the mass functions of the three MSs discovered by Piotto et al. (2007) and found that the slope of rMS-, mMS-, and bMS-mass function are $\alpha = -1.2 \pm 0.3$, $\alpha = -0.9 \pm 0.3$, and $\alpha = -0.9 \pm 0.4$, rispectively, i.e. are the same the same within the errors. In a paper from this series, Bellini et al. (2015), have investigated the internal kinematics of the stellar populations in NGC 2808 by using the same dataset from the central field used in this paper. They have found that in the most-external region that they have analyzed, between 1.5 and $\sim$2.0 times the half-light radius, the proper-motion distributions of the populations D and E, are significantly more anysotropic than that of the populations A, B, and C. On the basis of results from N-body simulation, Bellini and collaborators have suggested that the kinematic difference between the populations highly enhanced in helium and those with with almost primordial helium, are consistent with a scenario, where populations D and E were more-centrally concentrated at the time of their formation.

6

The multiple stellar populations of M92

Abstract

As part of the *Hubble Space Telescope* UV Legacy Survey of Galactic Globular Clusters, we have studied in detail the multiple stellar population in the low metallcity, old Galactic globular cluster NGC 6341 (M92).We focussed on the characterization of the Chromosome Map of RGB stars, leading to the identification of at least 2 distinct stellar populations. These could be further subdivided into subgroups if the photometric errors are properly modelled.

M92 is consistent with being a Type I cluster as defined in Milone et al. (2017). The radial analysis performed has not detected any strong population gradient, even though some hints suggest the presence of a small radial trend. Finally, the characterization of multiple stellar populations has been extended also to the main sequence region of the color-magnitude diagram.

6.1 Introduction

As part of the *Hubble Space Telescope* (HST) UV Legacy Survey of Galactic Globular Clusters, we have studied the multiple stellar population (MP) in the low metallcity, old Galactic globular cluster (GC) NGC 6341 (M92).

Since the advent of the early color-magnitude diagrams (CMD) in the '50s of the past century, this cluster has been the subject of a multitude of studies. Nonetheless, with the increasing attention devoted to the MP phenomenon in Galactic GCs, M92 has not been regarder as a peculiar case and few studies

have been dedicated to its study in this context. Notably, Lardo et al. (2011) detected a spread in the UV color distribution of red giant branch (RGB) stars of this cluster that has not consistent with the estimated photometric errors. The RGB has been thus assumed to be composed of two distinct stellar populations and, from the study of the radial distribution of the number of stars belonging to the two groups of stars, they found indication of the presence of a radial gradient. Mészáros et al. (2015) presented a detailed chemical aboundance analysis for RGB and asymptotic giant branch (AGB) stars in M92 (among the other clusters in their sample). The authors were able to divide their sample into two distinct stellar populations mainly looking at the Al-Mg observed anticorrelation. They also found that C+N+O content in the two stellar populations does not vary albeit some hints of variations among C, N and O between the two groups seems to be present. These studies corroborates what has been demonstrated in Piotto et al. (2015) that virtually all Galactic GCs hosts MP and that a combination of UV and visual filters is particularly suitable to detect their presence in these systems. In a subsequent paper of the same series, Milone et al. (2017) (hereafter Paper IX) further characterize the MP phenomenon introducing the so called Chromosome Maps (CM). With these diagrams, the authors have been able to explore the complexity of this phenomenon in the whole sample of GCs of the HST UV Legacy Survey.

In this work, we make use of the HST UV Legacy Survey exquisite data in order to study in detail the MP in M92. Specifically, we concentrate in the multiband characterization of stellar populations in the RGB part of the CMD and in the detection of possible radial gradients among them. In addition, we extend the study also to the main sequence (MS) region of the CMD for which ACS parallel observations are available in the context of the present survey.

The paper has the following structure: In Section 6.2 a general description of the data used is given; Section 6.3 is dedicated to the construction of the CM; the subsequent analysis of the diagram is presented in Section 6.4; the results are discussed in Section 6.5 along with the characterization of the MS; finally, in Section 6.6, we provide summary and conclusion.

6.2 Observations and Data Reduction

For this work we have used the photometric and astrometric catalogues presented in Nardiello et al. (2018b). These refers to a compilation of WFC3 UV data collected in the context of the HST UV Legacy Survey of Galactic Globular Clusters (Piotto et al. 2015) and other archival HST data that complement these observations of the central regions of a sample of 56 Galactic GCs and one open cluster. We remand to Nardiello et al. (2018b) for the details of the

data reduction and provide, in the following, a brief description. The photometric reduction has been performed on charge-transfer-efficency corrected, non-drizzled _flc images, using the software KITCHEN_SYNC2 (KS2, Anderson et al. in prep.; Sabbi et al. 2016; Bellini et al. 2017) in analogy with what has been done in Nardiello et al. (2018a) (hereafter N18). Final raw magnitudes have been calibrated in Vega-mag system by performing aperture photometry on drizzled _drc images and comparing the results with our PSF-based magnitudes. This produces an initial photometric list containing a total of 158391 stars.

Since we are interested in measuring small systematic differences in magnitude between distinct groups of stars, it is of paramount importance to exclude all the spurios measurements from our sample. We have achieved this following the prescriptions of Bellini et al. (2017) and N18. In brief, KS2 provide various indexes to asses the quality of the data (Bellini et al. 2017; N18); among them we have used the photometric error (σ), the QFIT parameter and the sharp parameter. More specifically, we started by removing from the catalogue all the sources which have not been measured in at least one filter. It resulted that 87560 stars cannot be used for this multi-band analysis. For the remaining 70831 stars, we have proceeded as follows. For each filter separately, we have considered the above indexes as a function of magnitude and have traced for each of them a ridge-line that contains $\sim 99.7\%$ of the points (i.e. 3 standard deviations) and used it to flag well-measured stars. In the case of the sharp parameter, the ridge-lines define a region of the distribution populated mainly by bona-fide stellar objects. For bright stars, the calculated standard deviations were so small that we needed to fix minimum values in order not to reject well-measured stars. We finally keep all the stars that passed the selection for all parameters and all filters simultaneously.

We show selection result in Figure 6.1. The left-side grid of panels displays for each filter and parameter the adopted ridge-lines (in red). Grey points shows the rejected sources, while black points refer to well-measured stars. For more clarity, only 10% of the total sources has been shown. In the lower-right panel we show the (F275W-F336W)-(F336W-F438W) vs F814W CMD of the rejected sources. A similar CMD, but for well-measured stars, is shown in the upper-right panel of Figure 6.1.

Considering the position of the cluster ($l = 68.34$ deg, $b = 34.86$ deg, Harris 1996, 2010 edition), the expected contamination from the Milky Way is almost negligible. Moreover, the expected reddening for this cluster is $E(B-V) = 0.02$ (Harris 1996, 2010 edition). Nevertheless, we have used proper motions (Nardiello et al. 2018b) to verify that all the stars in the selected sample are consistent with being cluster members.

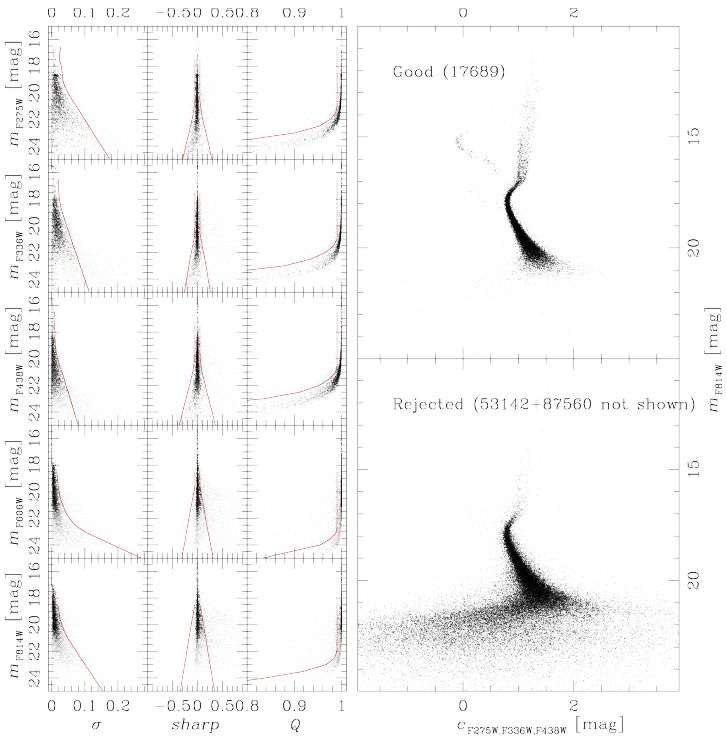

Figure 6.1: Left panels: Selection of well measured stars. Various photometric-quality indexes (columns) have been considered for each filter (rows) in analogy with other works of this series. Red lines have been hand-traced and used as ridge lines to identify in each plane well-measured stellar sources. Grey points represent sources rejected in at least one selection. Black points represents stellar sources that have survived the selection process. Upper-right panel: (F275W-F336W)-(F336W-F438W) vs F814W CMD of well-measure stars. Lower-right panel: (F275W-F336W)-(F336W-F438W) vs F814W CMD of the sources that do not have survived the selection process. For clarity, only 10% of the toal are shown. The 87560 sources not shown are those not measured in at least one filter. They were excluded from the sample before operating the selection procedure.

6.2.1 Artificial-star tests

In order to better characterize the impact of observational errors on the observed data and to examine the completeness level along our field of view, artificial stars have been generated following the prescription of N18. Specifically, about 250000 artificial RGB stars were generated in the magnitude interval $16.65 > \mathrm{F814W} > 13.55$ with a flat luminosity function and a Gaussian spatial distribution with $\sigma = 56$ arcseconds, centered in the cluster barycenter.

The color-magnitude relation used for these stars has been determined tracing fiducial lines in each of the four CMDs: F275W-F814W vs F814W; F336W-F814W vs F814W; F438W-F814W vs F814W, and F606W-F814W vs F814W. They are shown in Figure 6.2 as blue lines.

The completeness has been studied following Anderson et al. (2008a). According to them, an artificial star has been considered recovered if the difference between input and output position and F814W magnitude differ less than 0.5 pixel and 0.75 mag respectively. We finally computed the completeness taking also into account the effect of the selection criteria used for observed stars. We show the result of this analysis in Figure 6.3. It could be noted that the completeness level is above $\sim 85\%$ everywhere except in the central region.

6.3 The Chromosome Map of M92

In previous works of the present series, it has been demonstrated the usefulness of the so called Chromosome Map (CM) diagrams in order to accurately characterize the MP phenomenon in Galactic GCs (Piotto et al. 2015; Milone et al. 2015a; Milone et al. 2015b; Paper IX; N18). These diagrams, constructed using the (F275W-F814W) and the $c_{F275W,F336W,F438W}$ colors, are invaluable tools to exploit the information contained in the multi-band UV observations. For the present analysis we focused on the RGB region of the CMD, and in particular we selected only stars in the range $16.65 \geq \mathrm{F814W} \geq 13.55$. We firstly concentrated in the (F275W-F814W) vs F814W CMD, deriving a fiducial line in the selected RGB region. We have thus considered only stars that are at maximum 0.17 mag distant in color from that fiducial line (red region in the upper panel of Figure 6.2). We have then used F814W magnitude bins of $\delta m = 0.4$ mag and divided the selected magnitude range in sub-bins of $\delta m/3$ mag width. In each F814W magnitude bin we have calculated the 4^{th} and the 96^{th} percentile of the distribution of (F275W-F814W) colors and averaged the resuling ridge lines with a 3-point moving average.

The resulting fiducials are shown in the lower-left panel of Figure 6.4, for the (F275W-F814W) vs F814W case. We have indicated in blue the 4^{th} percentile

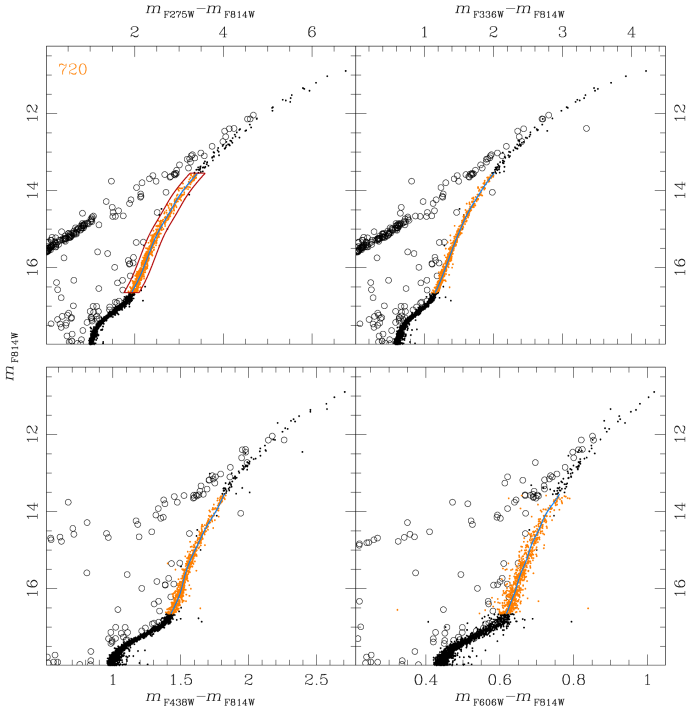

Figure 6.2: Upper-left panel: selection of RGB sample (orange points), see Section 6.3 for details. The final sample contains 720 stars. Black circles indicate stars removed from the computation of the fiducial line in blue. Upper-right panel: same as upper-left panel but for F336W-F814W color. Lower-left panel: same as upper-left panel but for F438W-F814W color. Lower-right panel:same as upper-left panel but for F606W-F814W color.

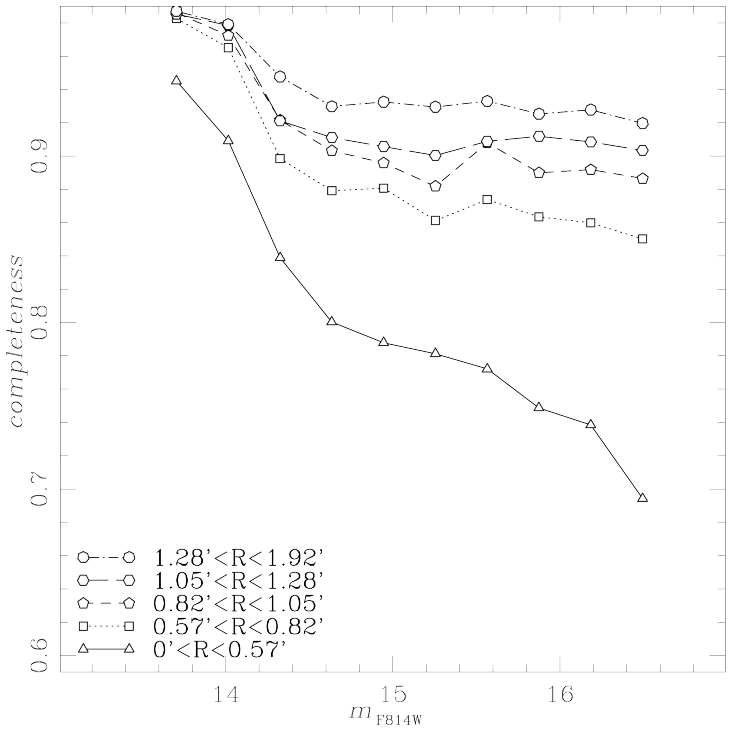

Figure 6.3: Completeness in different magnitude intervals. The radial dependence is also represented using different symbols.

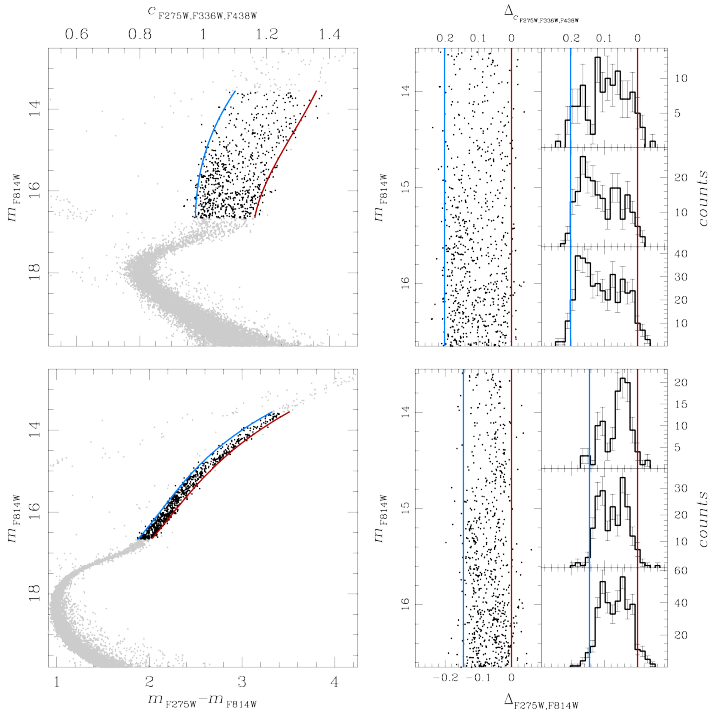

Figure 6.4: Ridge lines used for the CM construction. Lower-left panel: (F275W-F814W) vs F814W CMD. Grey points indicate non-used stars, black points show the used sample. The blue lines indicate the 4^{th} percentile fiducial, while the 96^{th} fiducial is shown as a red line. Lower-right panel, distribution of the selected star sample in the rectified CMD. The star counts distribution in 3 magnitude bins are shown in the right-most panels. Upper panels are analogs of the lower ones but for the $c_{F275W,F336W,F438W}$ vs F814W CMD.

fiducial (fiducialB) and in red the 96$^{\rm th}$ percentile one (fiducialR). We have used these fiducials to define the pseudo-color

$$\Delta_{\rm F275W,F814W} = W_X \frac{X - X_{\rm fiducialR}}{X_{\rm fiducialR} - X_{\rm fiducialB}} \tag{6.1}$$

where X is the color (F275W-F814W) and W_X is the difference in color between the two fiducials at a point placed 2 F814W magnitudes above the turn-off (TO) point ($m_{\rm TO} = 17.894 \pm 0.007$). We show the resulting $\Delta_{F275W,F814W}$ distribution in the lower-right panel of Figure 6.4 along with the distribution of stellar counts in 5 magnitude bins.

We repeated a similar operation for the $c_{\rm F275W,F336W,F438W}$ vs F814W CMD. In this case the pseudo-color has been defined as

$$\Delta_{c\rm F275W,F336W,F438W} = W_Y \frac{Y_{\rm fiducialR} - Y}{Y_{\rm fiducialR} - Y_{\rm fiducialB}} \tag{6.2}$$

where Y is the color $c_{\rm F275W,F336W,F438W}$. The fiducial lines obtained with this color combination are shown in the upper-left panel of Figure 6.4. The color distribution of $\Delta_{c\rm F275W,F336W,F438W}$ is shown in the upper-right panel.

The resulting CM is given in Figure 6.5. Black points refer to observed stars while the distribution of observational errors is shown in orange. For completeness we also show the count distribution in the two directions defined by $\Delta_{\rm F275W,F814W}$ and $\Delta_{c\rm F275W,F336W,F438W}$.

6.4 Population ratios and their radial distribution

It should be noted that the distribution of points in the CM shown in Figure 6.5, cannot be ascribed only to photometric errors. This is one of the main results presented in Paper IX, where it has been also demonstrated that groups of stars with different chemical composition occupy different loci in these diagrams. In particular, the lower part of the CM is occupied by what is assumed to be the first generation of stars (1G), with primordial chemical composition, while successive generations (2G) occupy the more vertical, upper part of the CM.

The subdivision of the sample into 1G stars and 2G stars can be performed following the procedure described in Paper IX, we illustrate it for M92 in Figure 6.6. Briefly, the CM is first rotated by an angle of 18 deg in order to define a reference frame where the lower part of the CM is horizontal. In this plane, the rotated error distribution is then fitted to the lower part of the CM and a ridge-line is marked at the 3σ level. In the case of M92, about 30% of points are found below this line and are thus associated to 1G.

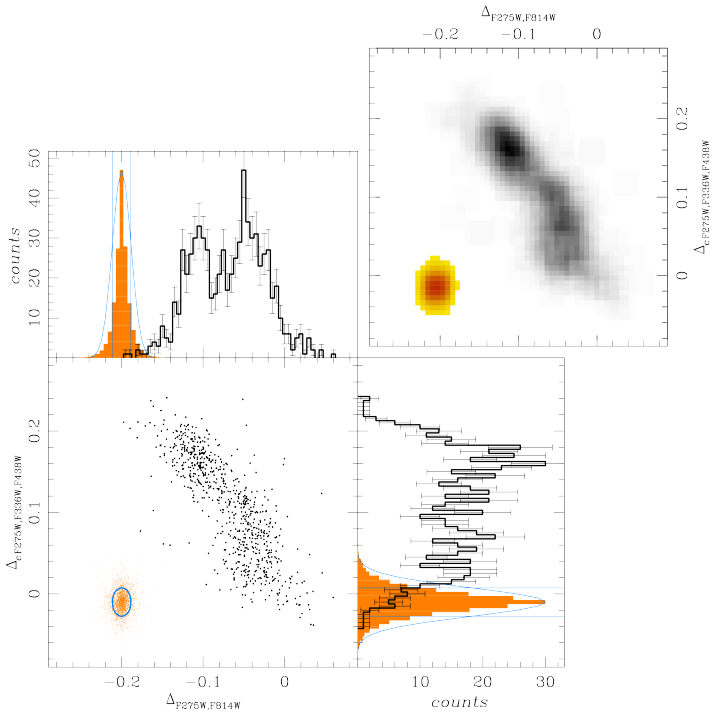

Figure 6.5: Resulting CM for M92 RGB star sample. Lower-left panel: The resulting CM; black points refer to observed stars while orange points represent the distribution of the observational error. The blue ellipse is the best fit ellipse to the distribution of observational errors, the semi-axis are equal to 1 standard deviation. The adjoint panels show the distribution of counts along the 2 directions defined by $\Delta_{F275W,F814W}$ and $\Delta_{cF275W,F336W,F438W}$. Upper-right panel: Hess diagram of the resulting CM.

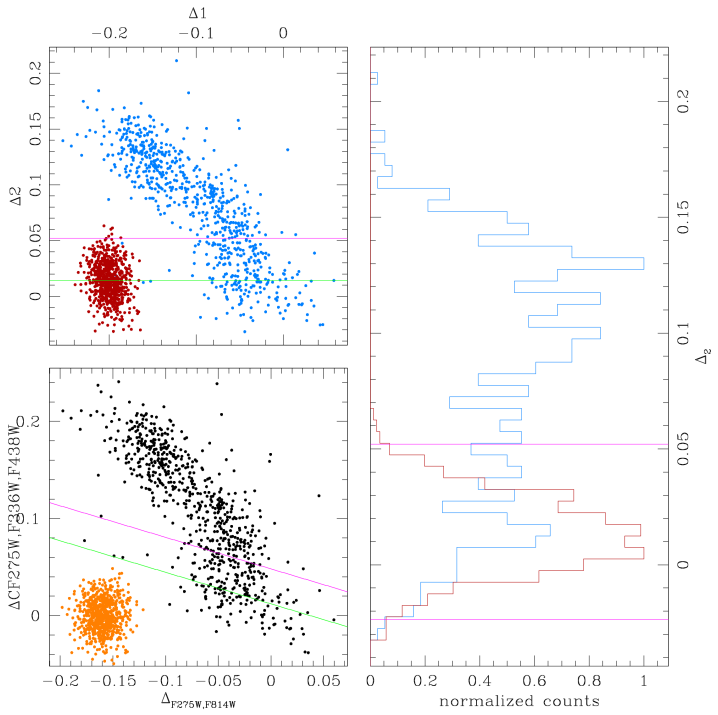

Figure 6.6: Procedure to select 1G stars from the whole sample (Paper IX). Upper-left panel: CM of M92 rotated counter-clockwise by an angle of 18 deg. The data points are plotted in blue, while red points represent the error distribution in this plane. The magenta line marks the 3σ ridgeline used to define the boundary below which 1G stars are found. The green line marks the $\Delta 2$ value at which the error distribution has been centered. Right panel: Normalized distribution of counts in the $\Delta 2$ direction (blue line), in red it is also shown the normalized distribution of error points. Lower-left panel: the CM of M92 (black points) and the associated error distribution (orange points). Magenta and green lines are the same as defined in the upper-left panel.

It can be noted, however, that the distribution of 1G points is more extended that what is expected from the distribution of errors. In particular, the standard deviation of 1G points along the $\Delta 1$ direction results to be ~ 2 times bigger than that measured for the errors in the same direction. A similar observation can be made also for 2G stars, for which the standard deviation along the least square fitting line, results to be ~ 3 times bigger than what is measured for the errors in the same direction. We interpret this as a possible evidence that 1G and 2G stars in M92 could be further subdivided into subgroups. The noisiness of the CM of this GC, however, prevent a clear separation by visual inspection as can be noted from the histograms in Figure 6.5.

Separating the single stellar populations present in the CM of M92 is not straightforward and we have operated in the following manner. In order to investigate if M92 could be comparable to other cases studied in literature, we have first assumed the presence of five distinct stellar populations (named A, B, C, D and E) and fixed by hand the center of each of them in the CM. We then took the observational error trace in the CM (the blue ellipse in Figure 6.5) as a template distribution for a single stellar population and created a synthetic CM using the previously fixed centers and this template. The same centers have been used to define the five elliptic regions where stars are counted in a similar way as N18. In this case, we have used elliptic regions with semi-major axis 3 times larger than the ones measured from observational errors. In each region (i), the number of observed stars (N_i) is linked to the total number of stars in each stellar population ($N_{A,B,C,D,E}$) by the equation:

$$N_i = f_i^A N_A + f_i^B N_B + f_i^C N_C + f_i^D N_D + f_i^E N_E \tag{6.3}$$

where $f_i^{A,B,C,D,E}$ are the fraction of stars of population A,B,C,D and E respectively expected to be found in region i. We have thus solved the system of 5 linear equations and found a first solution for N_A, N_B, N_C, N_D and N_E. We note here that N_i values have been corrected for completeness. With this first estimate, we have thus associated to each observed star a weight of being associated to each of the 5 populations using a Gaussian fit of the error trace as template. We then recalculated the position of the center of each population. In analogy with Milone et al. (2012a), observational sequences in the CM could display an intrinsic broadening that the model, based on the calculated photometric errors, fails to reproduce at the precision level necessary to our investigation. In order to take into account for the fact that observational errors could have been underestimated, we also calculate the multiplying factor to be applied to each synthetic distribution in order to better reproduce the observed distribution of stars for each population. We have used the new centers and

the mean of these multiplying factors in order to repeat the measure of N_A, N_B, N_C N_D and N_E.

The results of the last iteration of the process is shown in Figure 6.7, where the final configuration of the elliptical regions adopted to calculate the population ratios are also plotted. We found that convergence is reached in few iterations of the process and that the average multiplying factor that represents the observational distribution of stars is equal to 1.4.

We show the results of this procedure in figure 6.8. The color code is as follows: population A stars are shown in red; population B ones in magenta; population C ones in green; population D stars are shown in blue; population E ones in light-blue. We have found that population A contains $(5.3 \pm 0.8)\%$ of stars, population B $(26.1 \pm 1.5)\%$, population C $(24.7 \pm 1.5)\%$, population D $(34.0 \pm 1.6)\%$ and population E $(9.9 \pm 1.0)\%$ of stars.

To corroborate that in NGC 6341 there are 5 distinct populations, we have observed if the distribution of points in population C is consistent with each of the other. This is illustrated in bottom-right and upper-left panels of Figure 6.8 where, in the left column, we have first compared the distribution of AS (gray histogram) with population C distribution and, after having widened it, in the rightmost column we compared the obtained distribution of ASs with the distribution of all the other populations. We have chosen the distribution of population C as a template because it appears to be more isolated in the CM.

Using the centers and the multiplying factor found above, we also studied the radial distribution of the population ratios. Results are shown in Figure 6.9 where the color code is the same as in Figure 6.7. No population gradient has been detected within the errors. It is worth noting, however, that a trend may be detected, with population E slightly more centrally concentrated with respect to population B, which appears to be somewhat more diluted.

We have performed, for each radial bin, 100 measures slightly changing each time the position of the center of the population (both the model and the elliptical region). In order to do this we have exctracted randomly the values of the perturbation from a 2-D Gaussian distribution with amplitude equal to $\sigma/\sqrt{N-1}$, where N is the measured number of stars associated to each population and sigma is the standard deviation of the error distribution along the considered direction. The final values for the population ratios have been then measured as the median of the 100 values obtained for each population while the error bar lengths were determined finding the minimum and maximum values.

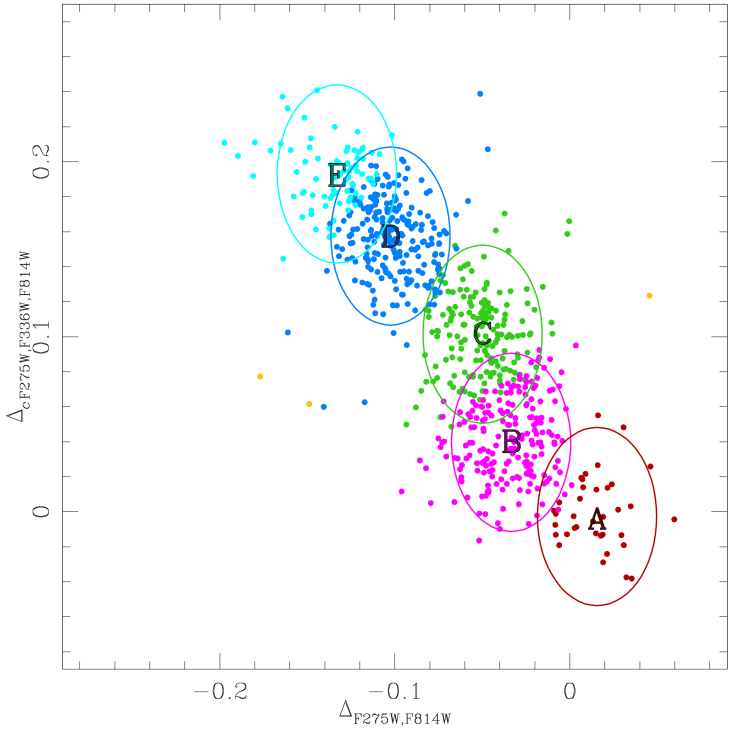

Figure 6.7: CM with stars color coded in respect to the most probable stellar population they are related to in the last iteration of the procedure to isolate them. The color code for the five population is given in the following. Population A, red; population B, magenta; population C, green; population D, blue; population E, light blue. We also show the elliptical regions associated to each population.

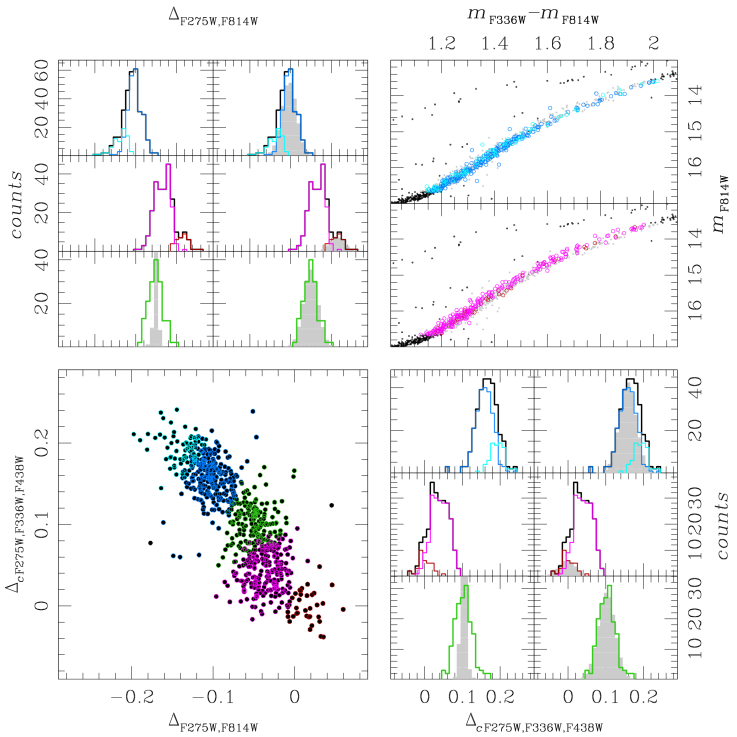

Figure 6.8: Bottom-left panel: CM with stars color coded as in Figure 6.7. Bottom-right and upper-left panels: first column, pseudo-color distribution of each single stellar component. We have compared the distribution of population counts with those obtained with ASs (gray shaded histograms). Second column, same as in the left column but this time the distribution of ASs was widened in order to better represent the observed distribution of population C stars (in green). We show the comparison with the distribution of all the other populations. Upper-right panel: F336W-F814W vs F814W CMDs. We highlighted the loci of population A (red) and B (magenta) in the lower CMD and population E (light blue) and D (blue) in he upper CMD.

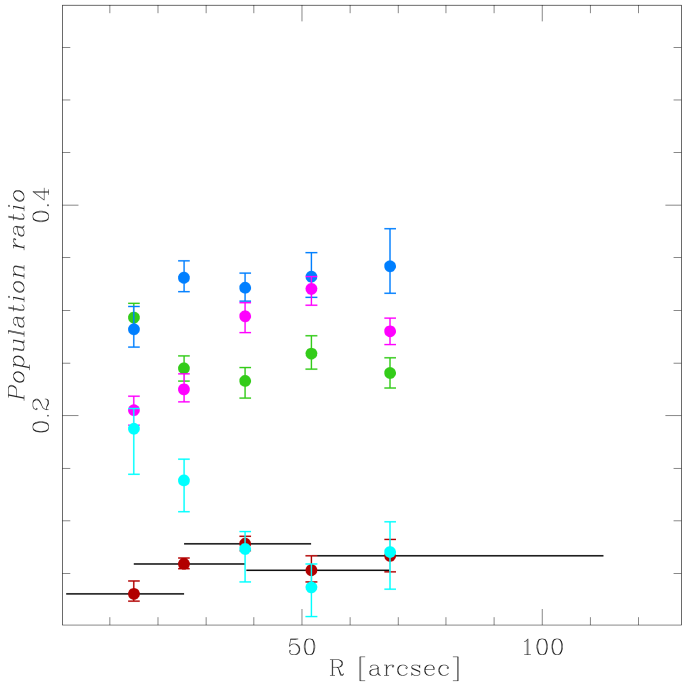

Figure 6.9: Radial distribution of the population ratios. The color code is the same as in Figure 6.7. Vertical lines represent the error associated to each population ratio measure. Black horizontal lines refer to the spatial extent of each radial bin.

6.5 Discussion

While the introduction of CMs (in previous works of this series, see eg. Milone et al. 2015b; Paper IX) has demonstrated how powerful these representations can be in separating distinct stellar population in GCs, CMs also demonstrate the complexity of the phenomenon. Milone et al. (2015b) show how quantitative information can be extracted from these diagrams and, in particular, how to decompose the CM of a GC into single stellar components. In N18 the method has been further refined and the two-dimension nature of the CM has been taken into account. But as demonstrated in Paper IX (and also in Milone et al. 2018), different chemical aboundances among GCs produce a wide spectrum of CMs, hardly resembling each other. Little is known about the origin of MP phenomenon in Galactic GCs and any observational input is of extreme importance in this phase. M92, along with M15, is one of the most metal poor GCs in the MW. It is thus very interesting to note that the CM obtained for these two clusters are different. As already visible in Paper IX and even more clearly after the detailed analysis of N18, the CM of M15 is 'S-shaped' while the CM of M92 presents a different morphology, indeed common among the GC classified as type I in Paper IX.

Figure 6.5 shows a clear separation into at least 2 stellar population. Nonetheless, given the relatively modest amplitude of the distribution of points, a detailed characterization of the photometric errors is mandatory in order to fully exploit the information from this particular CM. It is worth noting here that the photometric error is acting as the resolving power of the CM.

As explained in Section 6.3, we have adopted the photometric error trace as a template to separate the stars in the observed CM into a fixed number of distinct populations.

In particular, we have chosen to fix the number of stellar populations to be identified in this cluster to 5 in order to make a direct comparison with what has been obtained for the type I GC NGC 2808 in Milone et al. (2015b).

Based on their position in the CM, we link the populations we have found for M92 with those detected in NGC 2808 by Milone et al. (2015b). In Table 6.1 we compare the ratio obtained for each population in NGC 2808 with the results of the present work. It is very interesting to see somewhat an analogy between the two results. Nonetheless, population B in M92 seems to be more populated than its counterpart in NGC 2808 while, on the contrary, population E in M92 seems to be less numerous than in NGC 2808. In this respect it is very interesting to note that population E in NGC 2808 has been associated to the more He-enhanced population and that NGC 2808 is one order of magnitude more massive than M92. It is interesting also to note that NGC 2808 has a

Table 6.1: Resulting population ratios for M92. A comparison with the analogue populations found in NGC2808 by Milone et al. (2015b) is also made.

Pop. Milone et al. (2015b)	Corresponding Pop. this work	Pop. ratio Milone et al. (2015b)	Pop. ratio fixed cen.	Pop. ratio moving cen.
A	A	5.8 ± 0.5	5.3 ± 0.8	$5.8^{+1.1}_{-0.4}$
B	B	17.4 ± 0.9	26.1 ± 1.5	$25.9^{+1.0}_{-1.2}$
C	C	26.4 ± 1.2	24.7 ± 1.5	$25.5^{+1.0}_{-1.2}$
D	D	31.3 ± 1.3	34.0 ± 1.6	$31.6^{+1.9}_{-1.1}$
E	E	19.1 ± 1.0	9.9 ± 1.0	$11.3^{+1.5}_{-2.3}$

metallicity of [Fe/H] = −1.14 as opposed to M92 which has [Fe/H] = −2.15.

In Figure 6.10 the color difference between the fiducial lines of population B RGB stars and those of each other stellar population is shown. It is apparent that populations C, D and E follow a different trend than population A. Milone et al. (2015b) examined in detail how this kind of representation is affected by different chemical aboundance differences. In this sense Figure 6.10 suggests that populations C, D and E have different aboundances of C, N and O than to population B. While a detailed analysis by means of synthetic spectra is required to measure quantitatively these differences, the figure is consistent with the presence in M92 of stars that are enriched in nitrogen while depleted in carbon and oxygen. It is also likely the presence of slight helium enrichment. For what concern population A, it can be mentioned that a difference in effective temperature between these stars and those of population B are expected to produce similar results. We also note that Figure 6.10 is very similar to the one obtained by Milone et al. (2015b) for NGC 2808, albeit the amplitude of the color differences is smaller in the case of M92. This would indicate that such chemical aboundance differences, if present, would be smaller. Nonetheless, the nature of the processes that led to the present configuration of these systems could be the same.

To further compare our results with NGC 2808, we also show, in Figure 6.11, the radial gradients of population ratio modified for a more rapid comparison with Simioni et al. (2016). In this case, population E of M92 has been shown in blue, population D in green while in red it is shown population A+B+C.

6.5.1 The Main Sequences of M92

For the sake of completeness, we have investigated the presence of MP along the MS. This would be a further test to confirm what already found for the RGB stars. Moreover, in a recent publication, Simioni et al. (2018) presented the photometric and astrometric catalogues of the parallel ACS observations obtained in the context of the present survey. These data have been designed to optimally characterize these low mass stars in the outskirts of the clusters and have already been used to extend the spatial coverage of the data coming from the central region in NGC 2808 (Simioni et al. 2016). Specifically, for M92 two distinct fields have been observed in F475W and F814W. Albeit the stellar density is relatively low in them, the small crowding in these data results in lower photometric errors. In an effort to enhance the statistical significance of the results, in the following analysis, the catalogues of both fields have been summed.

In the upper-left panel of Figure 6.12 the MS of the central field of M92

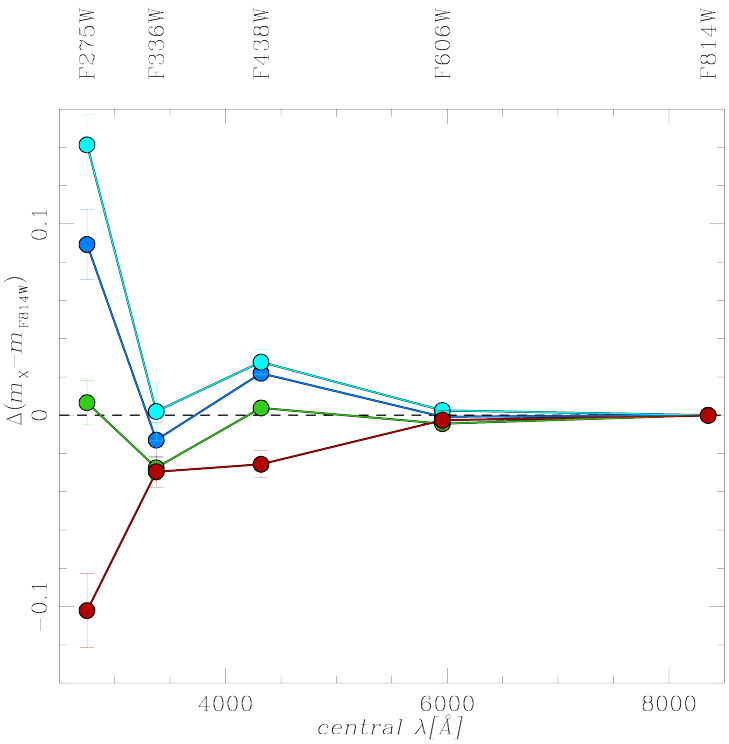

Figure 6.10: $\Delta(m_X - m_{F814W})$ color separation between the fiducials of population B and each of the other populations. The color-code adopted is the same as used previously. The magnitude used to measure the distance has been fixed to $m_{F814W} = 15.03$.

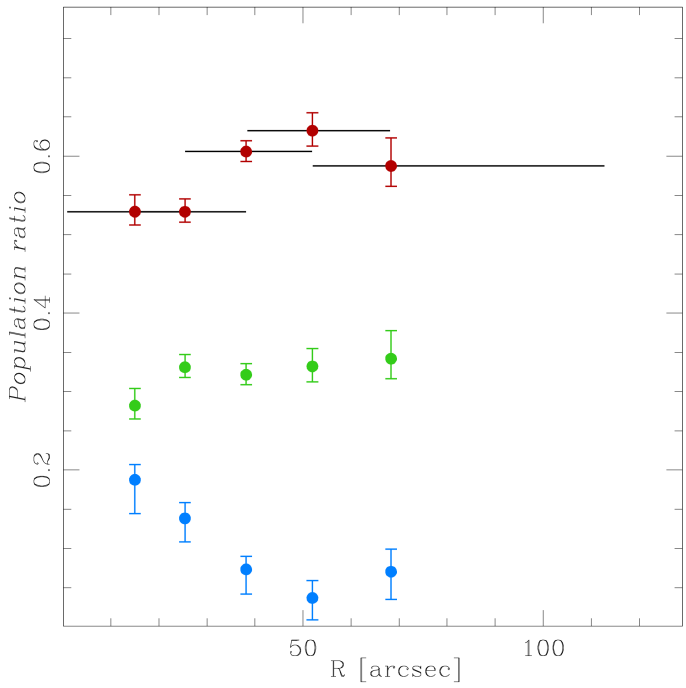

Figure 6.11: Radial distribution of the population ratios for the comparison with NGC 2808. Population E is indicated in blue, population D in green while population A+B+C are shown in red.

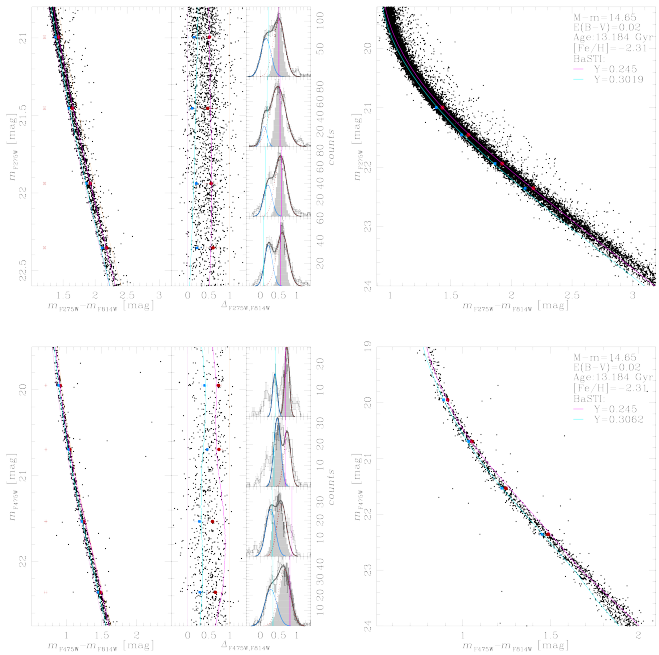

Figure 6.12: Linking the photometric catalogue of the central regions to ACS parallel observation one. Upper-right panel: on the left, the MS of M92 central region is shown along with the photometric error (red crosses). Blue and yellow lines have been used to rectify the sequence which is shown in the central inset. On the right, we show the distribution of stars in color. The gray-shaded distribution represents the photometric error associated to each magnitude interval. The distribution is consistent with the presence of at least 2 distinct stellar populations. In each magnitude bin, a function sum of two gaussian has been fitted to the data in order to locate the mean color of each stellar population along with their dispersion (blue and red dots and associated error bars). Two BaSTI isochrones have been fitted to the data imposing only He aboundance to vary between them and that primordial Y value is associated to the redder sequence. In azure the isochrone referred to the bluest population, while the primordial Y isochrone has been drawn in magenta. Upper-left panel: the resulting best-fitting BaSTI isochrones for the central field, color-coded as in the previous panel. Distance modulus, metallicity and reddening are from Harris (1996, 2010 edition) while the age of the cluster has been taken from Marín-Franch et al. (2009). Lower-panels: as in the upper panels, but for ACS parallel observation catalogues.

in the F275W-F814W filter combination is shown. After having rectified it (middle inset), we have studied the color distribution of the data into 4 magnitude bins (right inset). It is possible to observe that, in all bins, the color distribution reveals the presence of at least 2 distinct groups of stars. This seems consistent with what have been detected in the CM of RGB stars. This split can be appreciated, even not so clearly, also in the ACS parallel data (see lower-left panel of Figure 6.12). Since we are dealing with different color combinations, we have used the following procedure to verify if the observed split of the color distribution is consistent between the two datasets, the one referred to the central region and the ACS parallel one.

We first fit a function sum of two gaussian to the color distribution of points in each magnitude bin. We have then obtained the mean color of each stellar group and its dispersion. These measures have been used to fit a BaSTI isochrone to each stellar group. In performing such a fit, we have made the assumption that the redder group of stars is characterized by primordial He aboundance. Moreover, the Y value has been considered to be the only free parameter to vary. It results that, for the central field, the bluest stellar group must be enhanced by $\Delta Y \sim 0.057$ with respect to the primordial value in order to be able to fit the observed bluest MS. The same measure has been performed independently also for the ACS parallel fields obtaining $\Delta Y \sim 0.061$. In the right panels of Figure 6.12 we show the results of the fitting procedure. The accordance between the two values could indicate that the splitting of the MS of M92 in the two data sets is effective. In particular, these findings may open the path for the extension of the study of MP in M92 to larger spatial intervals. Nonetheless this would need further dedicated analysis.

6.6 Summary and Conclusions

Taking advantage of the exquisite quality of *WFC3* photometric data taken as a part of the *Hubble Space Telescope* UV Legacy Survey of Galactic Globular Clusters (Paper I), the multiple stellar populations in NGC 6341 (M92) have been characterized with unprecedent details. The results of this investigation are summarized in the following:

- The CM of RGB stars of M92 is consistent with this GC being a Type I cluster as defined in Paper IX.
- The CM of RGB stars is also consistent with the presence of at least 2 distinct stellar populations, nonetheless the distribution of photometric errors suggests the presence of additional subpopulations.

– By means of a detailed characterization of the photometric errors, it has been found a possible compatibility with the presence of 5 distinct stellar populations, that contains respectively 5% (A), 26% (B), 25% (C), 34% (D) and 10% (E) of RGB stars.

– In the present analysis, no population gradients have been detected within errors, however some hints of a trend may be present with population E more centrally concentrated and population B more diluted. An extension of the radial sampling would provide further evidences to settle this.

– We note a similarity between the stellar populations of M92 and those observed in NGC 2808 by Milone et al. (2015b).

– The MS of M92 is consistent with the presence of at least 2 distinct sequences.

– The splitting of the CMD into multiple MS is observed also in the parallel ACS observations opening the possibility of studying the MP of M92 in an extended spatial interval.

7

Conclusion

The existence of the MP phenomenon in GCs has been proposed as early as the '70s of the past century. Nonetheless, its presence has been clearly established only recently and for this reason, the present thesis is particularly timing and the obtained results add to a fast-growing wealth of knowledge about MP in GCs that is building up in these years. The MP phenomenon in Galactic GCs has been investigateg making use of the exquisite data collected in the context of the HST UV Legacy Survey of Galactic GCs. Distinct investigation paths have been pursued, we resume them in this chapter, listing the scientific evidences found.

The comparison between the CM of various Galactic GCs, led Milone et al. (2017) to subdivide them into Type I and Type II clusters. We have studied if and how cluster type correlates with other GC properties performing a principal component analysis based on 11 quantities: cluster type, Oosterhoff type, metallicity, relative age, orbits total energy, orbits total angular momentum, orbits eccentricity, orbits inclination with respect to the Glactic plane, clusters masses, core radii and tidal radii.

- The main sources of variance in the considered sample result to be contained in orbital parameters and, in sligthly less extent, in the relation between cluster type and relative ages.

- In the plane age-metallicity, type II clusters define a clear trend, with more metallic clusters being also younger. NGC 6388 is an exception, but it is also the only type II cluster that is located in the bulge.

- There are hints of a possible relation between age and Galactic distance

for type II GCs, with younger clusters being also more distant from the Galactic center.

– In the metallicity-Galactocentric distance, halo type II clusters seem to show a trend, with more metallic clusters located outwards. This trend is consistent with the radial distribution of their Oosterhoff type and apparently inconsistent with the trend found for type I GCs.

– The orbits of type II clusters seem to be more eccentric than the average of type I clusters. A large dispersion for the inclination of their orbits respect to the Galactic plane is also observed.

– Type II clusters are, on average, more massive than type I ones. There are, in any case, type I clusters with mass comparable to those of type II.

– The spatial distribution of type II GCs has highlighted that these clusters are, nowadays, preferentially located below the plane of the Galaxy. Specifically, no type II GC has been observed above Z$\sim$ 2.

In the context of the *Hubble Space Telescope* UV Legacy Survey Treasury program of Galactic Globular Clusters, we reduced the ACS/WFC parallel observations data and released the relative photometric and astrometric catalogues (Simioni et al. 2018).

– The data-set consists of 109 distinct stellar fields for 49 targets: 48 GCs and one open cluster, NGC 6791. They represent the first *HST* photometric survey of external regions of Galactic GCs.

– In the majority of cases, only two images per field were taken, one in F814W and one in F475W, centred at about 6.5 arcminutes from cluster centre. Exposure times were selected in order to obtain reliable photometry of the main sequence of target GCs.

We have investigated the radial distribution of the three main populations of NGC 2808 which correspond to the bMS, the mMS, and the rMS of Milone et al. (2012a). The analysis has been published in a refereed journal (Simioni et al. 2016).

– Parallel ACS/WFC data, presented here for the first time and relative to external regions of the cluster, has been combined with WFC3/UVIS ones relative to the central regions. The radial coverage extends from the cluster center out to about 8.5 arcmin.

– The three MSs have been detected in all the analyzed fields.

– At radial distance smaller than 0.75 arcmin, the three MSs can not be clearly distinguished due to stellar crowding. We have used the photometry of RGB stars from Milone et al. (2015b) to extend the study of multiple stellar populations to the cluster center.

– Using two different methods, we found that the populations which correspond to the rMS are less centrally concentrated than the helium rich stellar populations, with a significance for the result that is higher than 3σ.

– We presented the results of a simple N-body simulation illustrating the possible evolution of the multiple population spatial mixing of this cluster.

As a part of the *Hubble Space Telescope* UV Legacy Survey of Galactic Globular Clusters, we have characterized the multiple stellar populations in NGC 6341 (M92).

– The CM of RGB stars of M92 is consistent with this GC being a Type I cluster as defined in Paper IX.

– The CM of RGB stars is also consistent with the presence of at least 2 distinct stellar populations, nonetheless the distribution of photometric errors suggests the presence of additional subpopulations.

– By means of a detailed characterization of the photometric errors, it has been explored the possibility of the presence of 5 distinct stellar populations, that contains respectively 5% (A), 26% (B), 25% (C), 34% (D) and 10% (E) of RGB stars.

– No population gradients have been detected within errors, however some hints of a trend may be present with population E more centrally concentrated and population B more diluted. An extension of the radial sampling would provide further evidences to settle this.

– We noted a similarity between the stellar populations of M92 and those observed in NGC 2808 by Milone et al. (2015b).

– The MS of M92 is consistent with the presence of at least 2 distinct sequences.

– The splitting of the CMD into multiple MS is observed also in the parallel ACS observations, opening the possibility of studying the MP of M92 in an extended spatial interval.

Acknowledgments

Many are the people that have contributed in many different ways to the development of the presented research. First I want to thank Antonio, for all the discussion and the many teachings he gave me. I would like to thank Giampaolo, for all he has done to help me achieve this goal. I want also to thank Rolly for all the time he dedicated to me. Along with my supervisors, I would also like to thank the institutions that hosted me over these years, the IAC, the ULL, the UniPD and the INAF-OAPD. A special thanks goes to Antonino, Santi, Sebastian, Edoardo and Mimmo. I thank also Ata and Manuela who have evaluated this manuscript. Finally, I would like to thank my family for always being present.

Bibliography

Aarseth, S. J. 2003, Gravitational N-Body Simulations (Cambridge University Press), 430

Anderson, A. J. 1997, PhD thesis, University of California, Berkeley

Anderson, J., & Bedin, L. R. 2010, PASP, 122, 1035

Anderson, J., Bedin, L. R., Piotto, G., Yadav, R. S., & Bellini, A. 2006, A&A, 454, 1029

Anderson, J., & King, I. R. 2006, PSFs, Photometry, and Astronomy for the ACS/WFC, Tech. rep., Space Telescope Science Institute

Anderson, J., Sarajedini, A., Bedin, L. R., et al. 2008a, AJ, 135, 2055

Anderson, J., King, I. R., Richer, H. B., et al. 2008b, AJ, 135, 2114

Arp, H. C., Baum, W. A., & Sandage, A. R. 1952, AJ, 57, 4

Baade, W. 1944, ApJ, 100, 137

Bastian, N., Cabrera-Ziri, I., & Salaris, M. 2015, MNRAS, 449, 3333

Bastian, N., Lamers, H. J. G. L. M., de Mink, S. E., et al. 2013, MNRAS, 436, 2398

Beccari, G., Bellazzini, M., Lardo, C., et al. 2013, MNRAS, 431, 1995

Bedin, L. R., Cassisi, S., Castelli, F., et al. 2005, MNRAS, 357, 1038

Bedin, L. R., King, I. R., Anderson, J., et al. 2008, ApJ, 678, 1279

Bedin, L. R., Piotto, G., Anderson, J., et al. 2004, ApJ, 605, L125

Bedin, L. R., Piotto, G., Zoccali, M., et al. 2000, A&A, 363, 159

Bedin, L. R., Salaris, M., King, I. R., et al. 2010, ApJ, 708, L32

Bedin, L. R., Salaris, M., Piotto, G., et al. 2009, ApJ, 697, 965

Bekki, K., Campbell, S. W., Lattanzio, J. C., & Norris, J. E. 2007, MNRAS, 377, 335

Bekki, K., Jeřábková, T., & Kroupa, P. 2017, MNRAS, 471, 2242

Bellazzini, M., Ferraro, F. R., & Ibata, R. 2003, AJ, 125, 188

Bellini, A., Anderson, J., & Bedin, L. R. 2011, PASP, 123, 622

Bellini, A., Anderson, J., Bedin, L. R., et al. 2017, ApJ, 842, 6

Bellini, A., Anderson, J., Salaris, M., et al. 2013b, ApJ, 769, L32

Bellini, A., & Bedin, L. R. 2009, PASP, 121, 1419

Bellini, A., Bedin, L. R., Piotto, G., et al. 2010, AJ, 140, 631

Bellini, A., Piotto, G., Bedin, L. R., et al. 2009, A&A, 507, 1393

Bellini, A., Piotto, G., Milone, A. P., et al. 2013a, ApJ, 765, 32

Bellini, A., Vesperini, E., Piotto, G., et al. 2015, ApJ, 810, L13

Bohlin, R. C. 2016, AJ, 152, 60

Bono, G. 2010, Mem. Soc. Astron. Italiana, 81, 863

Brown, T. M., Cassisi, S., D'Antona, F., et al. 2016, ApJ, 822, 44

Carretta, E. 2014, ApJ, 795, L28

Carretta, E., Bragaglia, A., D'Orazi, V., Lucatello, S., & Gratton, R. G. 2010c, A&A, 519, A71

Carretta, E., Bragaglia, A., Gratton, R., D'Orazi, V., & Lucatello, S. 2009c, A&A, 508, 695

Carretta, E., Bragaglia, A., Gratton, R., & Lucatello, S. 2009b, A&A, 505, 139

Carretta, E., Bragaglia, A., Gratton, R. G., et al. 2006, A&A, 450, 523

—. 2010b, A&A, 516, A55

—. 2009a, A&A, 505, 117

—. 2013, A&A, 557, A138

Casetti-Dinescu, D. I., Girard, T. M., Jílková, L., et al. 2013, AJ, 146, 33

Cassisi, S., Salaris, M., Pietrinferni, A., & Hyder, D. 2017, MNRAS, 464, 2341

Catelan, M. 2009, Ap&SS, 320, 261

Charbonnel, C. 2016, in EAS Publications Series, Vol. 80, EAS Publications Series, ed. E. Moraux, Y. Lebreton, & C. Charbonnel, 177–226

Cordero, M. J., Pilachowski, C. A., Johnson, C. I., et al. 2014, ApJ, 780, 94

Crane, J. D., Majewski, S. R., Rocha-Pinto, H. J., et al. 2003, ApJ, 594, L119

Dalessandro, E., Salaris, M., Ferraro, F. R., et al. 2011, MNRAS, 410, 694

Dalessandro, E., Massari, D., Bellazzini, M., et al. 2014, ApJ, 791, L4

D'Antona, F., Bellazzini, M., Caloi, V., et al. 2005, ApJ, 631, 868

D'Antona, F., & Caloi, V. 2004, ApJ, 611, 871

D'Antona, F., Vesperini, E., D'Ercole, A., et al. 2016, MNRAS, 458, 2122

de Mink, S. E., Pols, O. R., Langer, N., & Izzard, R. G. 2009, A&A, 507, L1

Denissenkov, P. A., & Hartwick, F. D. A. 2014, MNRAS, 437, L21

Denissenkov, P. A., VandenBerg, D. A., Hartwick, F. D. A., et al. 2015, MNRAS, 448, 3314

D'Ercole, A., D'Antona, F., Ventura, P., Vesperini, E., & McMillan, S. L. W. 2010, MNRAS, 407, 854

D'Ercole, A., Vesperini, E., D'Antona, F., McMillan, S. L. W., & Recchi, S. 2008, MNRAS, 391, 825

Dinescu, D. I., Girard, T. M., & van Altena, W. F. 1999, AJ, 117, 1792

Dinescu, D. I., Majewski, S. R., Girard, T. M., & Cudworth, K. M. 2000, AJ, 120, 1892

Frinchaboy, P. M., Majewski, S. R., Crane, J. D., et al. 2004, ApJ, 602, L21

Gaia Collaboration, Brown, A. G. A., Vallenari, A., et al. 2016, A&A, 595, A2

Giersz, M., & Heggie, D. C. 2011, MNRAS, 410, 2698

Gilliland, R. L. 2004, ACS CCD Gains, Full Well Depths, and Linearity up to and Beyond Saturation, Tech. rep., Space Telescope Science Institute

Girardi, L., Groenewegen, M. A. T., Hatziminaoglou, E., & da Costa, L. 2005, A&A, 436, 895

Gnedin, O. Y., & Ostriker, J. P. 1997, ApJ, 474, 223

Gratton, R., Sneden, C., & Carretta, E. 2004, ARA&A, 42, 385

Gratton, R. G., Carretta, E., & Bragaglia, A. 2012, A&A Rev., 20, 50

Gratton, R. G., Lucatello, S., Sollima, A., et al. 2013, A&A, 549, A41

Harris, W. E. 1996, 2010 edition, AJ, 112, 1487

—. 2001, Globular Cluster Systems (Springer-Verlag Berlin Heidelberg), 223

Harris, W. E., Ciccone, S. M., Eadie, G. M., et al. 2017, ApJ, 835, 101

Heggie, D. C. 2014, MNRAS, 445, 3435

Iannicola, G., Monelli, M., Bono, G., et al. 2009, ApJ, 696, L120

Ibata, R. A., Gilmore, G., & Irwin, M. J. 1995, MNRAS, 277, 781

Iben, Jr., I. 1967, ARA&A, 5, 571

King, I. R. 1966, AJ, 71, 64

Kraft, R. P. 1979, ARA&A, 17, 309

—. 1994, PASP, 106, 553

Krause, M., Charbonnel, C., Decressin, T., Meynet, G., & Prantzos, N. 2013, A&A, 552, A121

Kroupa, P. 2001, MNRAS, 322, 231

Kunder, A., Stetson, P. B., Cassisi, S., et al. 2013, AJ, 146, 119

Lagioia, E. P., Milone, A. P., Marino, A. F., et al. 2018, MNRAS, 475, 4088

Lardo, C., Bellazzini, M., Pancino, E., et al. 2011, A&A, 525, A114

Lee, Y.-W., Joo, J.-M., Sohn, Y.-J., et al. 1999, Nature, 402, 55

Mackey, A. D., & van den Bergh, S. 2005, MNRAS, 360, 631

Marín-Franch, A., Aparicio, A., Piotto, G., et al. 2009, ApJ, 694, 1498

Marino, A. F., Villanova, S., Piotto, G., et al. 2008, A&A, 490, 625

Marino, A. F., Milone, A. P., Przybilla, N., et al. 2014, MNRAS, 437, 1609

Marino, A. F., Yong, D., Milone, A. P., et al. 2018, ApJ, 859, 81

Martell, S. L., & Grebel, E. K. 2010, A&A, 519, A14

Martin, N. F., Ibata, R. A., Conn, B. C., et al. 2004, MNRAS, 355, L33

Mészáros, S., Martell, S. L., Shetrone, M., et al. 2015, AJ, 149, 153

Meylan, G., & Heggie, D. C. 1997, A&A Rev., 8, 1

Milone, A. P., Bedin, L. R., Piotto, G., & Anderson, J. 2009a, A&A, 497, 755

Milone, A. P., Piotto, G., Bedin, L. R., et al. 2012c, A&A, 540, A16

—. 2012a, A&A, 537, A77

Milone, A. P., Stetson, P. B., Piotto, G., et al. 2009b, A&A, 503, 755

Milone, A. P., Bedin, L. R., Piotto, G., et al. 2008, ApJ, 673, 241

Milone, A. P., Piotto, G., King, I. R., et al. 2010, ApJ, 709, 1183

Milone, A. P., Piotto, G., Bedin, L. R., et al. 2012b, ApJ, 744, 58

Milone, A. P., Marino, A. F., Cassisi, S., et al. 2012d, ApJ, 754, L34

Milone, A. P., Marino, A. F., Piotto, G., et al. 2013, ApJ, 767, 120

—. 2015a, MNRAS, 447, 927

—. 2015b, ApJ, 808, 51

Milone, A. P., Piotto, G., Renzini, A., et al. 2017, MNRAS, 464, 3636

Milone, A. P., Marino, A. F., Renzini, A., et al. 2018, MNRAS, 481, 5098

Moehler, S. 2001, PASP, 113, 1162

Nardiello, D., Milone, A. P., Piotto, G., et al. 2015, A&A, 573, A70

—. 2018a, MNRAS, 477, 2004

Nardiello, D., Libralato, M., Piotto, G., et al. 2018b, MNRAS, 481, 3382

Nitadori, K., & Aarseth, S. J. 2012, MNRAS, 424, 545

Oke, J. B., & Schwarzschild, M. 1952, ApJ, 116, 317

Oort, J. H. 1926, PhD thesis, Publications of the Kapteyn Astronomical Laboratory Groningen, vol. 40, pp.1-75

Pancino, E., Ferraro, F. R., Bellazzini, M., Piotto, G., & Zoccali, M. 2000, ApJ, 534, L83

Pasquini, L., Mauas, P., Käufl, H. U., & Cacciari, C. 2011, A&A, 531, A35

Paust, N. E. Q., Reid, I. N., Piotto, G., et al. 2010, AJ, 139, 476

Pietrinferni, A., Cassisi, S., Salaris, M., & Castelli, F. 2004, ApJ, 612, 168

Pietrinferni, A., Cassisi, S., Salaris, M., Percival, S., & Ferguson, J. W. 2009, ApJ, 697, 275

Piotto, G. 2009, in IAU Symposium, Vol. 258, The Ages of Stars, ed. E. E. Mamajek, D. R. Soderblom, & R. F. G. Wyse, 233–244

Piotto, G., Milone, A. P., Marino, A. F., et al. 2013, ApJ, 775, 15

Piotto, G., King, I. R., Djorgovski, S. G., et al. 2002, A&A, 391, 945

Piotto, G., Bedin, L. R., Anderson, J., et al. 2007, ApJ, 661, L53

Piotto, G., Milone, A. P., Anderson, J., et al. 2012, ApJ, 760, 39

Piotto, G., Milone, A. P., Bedin, L. R., et al. 2015, AJ, 149, 91

Renzini, A. 1981, Annales de Physique, 6, 87

Renzini, A. 1987, in European Southern Observatory Conference and Workshop Proceedings, Vol. 27, European Southern Observatory Conference and Workshop Proceedings, ed. M. Azzopardi & F. Matteucci, 289–298

—. 2013, Mem. Soc. Astron. Italiana, 84, 162

Renzini, A., & Fusi Pecci, F. 1988, ARA&A, 26, 199

Renzini, A., D'Antona, F., Cassisi, S., et al. 2015, MNRAS, 454, 4197

Rosenberg, A., Aparicio, A., Saviane, I., & Piotto, G. 2000b, A&AS, 145, 451

Rosenberg, A., Piotto, G., Saviane, I., & Aparicio, A. 2000a, A&AS, 144, 5

Sabbi, E., Lennon, D. J., Anderson, J., et al. 2016, ApJS, 222, 11

Sandage, A. 1953, PhD thesis, California Institute of Technology

Sandage, A. R., & Schwarzschild, M. 1952, ApJ, 116, 463

Sarajedini, A., Bedin, L. R., Chaboyer, B., et al. 2007, AJ, 133, 1658

Sbordone, L., Salaris, M., Weiss, A., & Cassisi, S. 2011, A&A, 534, A9

Shapley, H. 1918, PASP, 30, 42

Siegel, M. H., Majewski, S. R., Law, D. R., et al. 2011, ApJ, 743, 20

Simioni, M., Milone, A. P., Bedin, L. R., et al. 2016, MNRAS, 463, 449

Simioni, M., Bedin, L. R., Aparicio, A., et al. 2018, MNRAS, 476, 271

Slemer, A., Marigo, P., Piatti, D., et al. 2017, MNRAS, 465, 4817

Smith, G. H. 1987, PASP, 99, 67

Sollima, A., & Baumgardt, H. 2017, MNRAS, 471, 3668

Sollima, A., Cacciari, C., Bellazzini, M., & Colucci, S. 2010, MNRAS, 406, 329

Sollima, A., Cassisi, S., Fiorentino, G., & Gratton, R. G. 2014, MNRAS, 444, 1862

Sollima, A., Ferraro, F. R., Bellazzini, M., et al. 2007, ApJ, 654, 915

Sosin, C., Dorman, B., Djorgovski, S. G., et al. 1997, ApJ, 480, L35

van den Bergh, S. 2011, PASP, 123, 1044

Vesperini, E., & Heggie, D. C. 1997, MNRAS, 289, 898

Vesperini, E., McMillan, S. L. W., D'Antona, F., & D'Ercole, A. 2010, ApJ, 718, L112

—. 2013, MNRAS, 429, 1913

Yong, D., & Grundahl, F. 2008, ApJ, 672, L29

Zinn, R. 1985, ApJ, 293, 424

Zinn, R. 1988, in IAU Symposium, Vol. 126, The Harlow-Shapley Symposium on Globular Cluster Systems in Galaxies, ed. J. E. Grindlay & A. G. D. Philip, 37–46

Zorotovic, M., Catelan, M., Smith, H. A., et al. 2010, AJ, 139, 357